CHARACTERISATION AND MODELLING OF SEGREGATION IN CONTINUOUSLY CAST STEEL SLAB

By

DAYUE ZHANG

A thesis submitted to the University of Birmingham for the degree of

DOCTOR OF PHILOSOPHY

School of Metallurgy and Materials

College of Engineering and Physical Sciences

The University of Birmingham

September 2015

Abstract

The microstructures of as-continuously cast steel slabs were characterised by optical microscopy (OM) and scanning electron microscopy (SEM). The second dendrite arm spacing (SDAS) at the quarter thickness position in each steel slab was obtained by measuring the distance between two adjacent parallel pearlite colonies. The microsegregation profiles of Mn, Si and Ni in steels at the same quarter thickness position were characterised by scanning electron microscopy-energy dispersive X-ray spectroscopy (SEM-EDS) using cumulative profile method. The segregation profiles were obtained by sorting the EDS data using weighted interval rank sorting (WIRS) and single element sorting (SES) methods. The Mn profiles have sharp slopes at the beginning and end of the profile with a shallow slope through the middle. The slope changing areas between the middle and end (right-hand) parts of the segregation profiles were assumed to separate the solute-rich and solute-depleted region and solute-rich region fractions were obtained by analysing the segregation profiles.

Thermo-Calc (part of Thermo-Calc software) was used to predict the equilibrium phase transformations for each steel. Pipeline and structural steel slabs were predicted to solidify without peritectic reaction; ship building and slab 1 steel slabs were predicted to solidify through the peritectic reaction. A hypothesis of solute-rich region formation was proposed that the austenite layer formed during the peritectic reaction stops the diffusion of substitutional alloying element atoms from liquid into the already-formed solid so that the atoms were trapped in the liquid and solute-rich region formed on eventual solidification of that liquid region.

Analytical approaches (Clyne-Kurz and Scheil) and Thermo-Calc were used to predict the segregation (segregation profiles and solute-rich fraction) behaviour of each steel slab. The segregation profiles predicted by Clyne-Kurz model agree with experimental results better than those predicted by other models. The solute-rich fractions predicted by Clyne-Kurz model and Thermo-Calc have a reasonable agreement with the experimental solute-rich fractions.

DICTRA (another part of Thermo-Calc software) considering the cross-effect of different elements in steels were used to simulate interdendritic microsegregation. Root mean square deviation (RMSD) values were determined to characterise the difference between the experimental and predicted segregation profiles. RMSD values were less than the experimental standard deviations except for slab 1 steel. The reasons may be the inaccurate predicted cooling rate or the coalescence coarsening effect which has not been considered in DICTRA.

Two directional solidification (DS) trials at 50 and 200 - 100 mm/h withdrawal rates were carried out to verify DICTRA simulations under known (measured) cooling histories. Microstructures of DS samples were characterised by OM and SDAS values were measured. DICTRA prediction using the measured cooling rate and SDAS values fell into the scatter band of WIRS profiles. However, discrepancy between the simulation and best fit to the WIRS profiles was found in the centre of both the dendritic and interdendritic regions. The discrepancy may indicate that the diffusion of Mn, Ni and Si in δ-ferrite used in DICTRA are faster than real situation.

The comparison between DICTRA predictions, Howe's model predictions and experimental results in Fe-C-Mn steels from the literature report was carried out. The DICTRA predictions

were greater than Howe's model prediction in terms of maximum Mn concentrations. The use of Mn partition coefficients and diffusion coefficients that were dependent on the temperature and composition in DICTRA may account for the difference.

Acknowledgements

I would like to express my enormous gratitude to my main supervisor Dr. Martin Strangwood for his guidance, support and encouragement during the whole PhD project and for his time and patience when he corrected my thesis which gave me confidence and sustained me to finish my thesis.

I also would like to thank Prof. Claire Davis, my second supervisor, for her encouragement and valuable advices for my research work.

Financial support from the School of Metallurgy and Materials, the University of Birmingham, and China Scholarship Council is gratefully acknowledged. Also I thank Shougang Steel Company, China and Corus, UK for providing the materials for this research.

I would like to thank Mr. Paul Stanley (SEM) and Mrs. Teresa Morris (SEM), Ms. Avril Rogers (heat treatment and hardness), Mr. Jaswinder Singh (sample preparation) and Mr. Peter Cranmer (directional solidification), Mr. Grant Holt (lost wax investment casting) and Mr. Paul Osbourne.

Massive thanks to the inhabitants of 1B20, and all the members of Phase Transformation and Microstructural Modelling Group, especially Carl Slater (for help with Thermo-Calc), Christoph Karl (for help with optical microscopy), Lei Zhou (for help with sample preparation), Guowei Zhang and Xi Liu (for help with Matlab) and my friends in the department.

My sincere gratitude to my friends especially Miss Kathryn Newton, Dr. Jing Yang, Dr. Yu Lu, Miss Ching Man Chan, Dr. Carl Meggs and Mr. Mick Wickins for their constant support and encouragement which helped me overcome the hard times.

I sincerely thank Dr. Xinxin Zhao. Without her help and encouragement, it would not be possible for me to reach this country and complete my research here.

Finally, I wish to thank my parents who always encourage and support me in a countless way and I would like to dedicate my thesis to them.

Contents

List of Figures

List of Tables

Chapter 1 Introduction

Continuous casting technology proposed in the 1950s has influenced the steelmaking industry worldwide and evolved to obtain improved quality of metal with lower cost and higher productivity. HSLA (high strength low alloy) steel slabs containing microalloying elements such as Nb, V and Ti produced by the continuous casting technique have been widely used in the automotive industry, manufacturing of pipelines for gas and oil transportation or plates for constructing ships in recent years due to the combined mechanical property of high strength and high toughness. The basic process of continuous casting is shown in Figure 1-1. The molten metal is poured into a water-cooled mould with an open bottom where the thin shell (10 mm to 20 mm wall thickness) is formed and primary solidification occurs. The strand subsequently passes through the secondary cooling region (water sprays) and radiative cooling region until the centre of the metal solidifies fully. After solidification, the metal has turned through 90 degrees and is oriented to go through the rolling process.

Thermomechanical controlled rolling (TMCR) has been used to decrease the processing cost and to improve both strength and toughness by refining the grains in continuously cast HSLA steel. The small amount of microalloying elements added in the steel form precipitates with carbon and nitrogen during casting and the subsequent hot rolling process which retard austenite recrystallisation during TMCR, so that refined grains are obtained in the final product. In addition, the fine precipitates also contribute to increase the overall strength of the steel. Nb has been found to be the most effective element to retard static recovery and recrystallisation and also affect the solute strengthening after high temperature deformation [1].

However Nb and Ti segregate strongly to the interdendritic region during solidification to cause inhomogeneous precipitate distributions in as-cast slabs [2] and even the formation of undesirable large precipitates [3]. Bimodal ferrite grain distributions (mixed coarse and fine grains) have been observed in Nb-bearing HSLA steels after TMCR processing and related to interdendritic segregation [4]. During reheating, the inhomogeneous precipitate distribution in as-cast steel slabs can produce a variation in precipitate dissolution temperature between solute-rich and solute-depleted regions, so that partially dissolved precipitates in the micro-scale at a certain reheating temperature range result in the formation of grain size bimodality [5, 6]. Bimodal grain structure can also form during deformation within a certain temperature range due to partial recrystallisation related to solute-rich and solute-poor regions [7]. This wide ferrite grain size distribution can produce a high degree of scatter in properties, eg. fracture toughness [8].It is desirable to avoid bimodal grain size distribution by controlling reheating and rolling process parameters according to microalloying element distribution in the solute-rich and solute-depleted regions. Therefore the prediction of segregation in as-cast material has particular practical importance. In this study, analytical and numerical segregation modelling based on HSLA as-continuously cast steel have been carried out in order to provide information on segregation for the subsequent reheating and rolling process. In addition, the directional solidification technique has been used to investigate segregation under controlled solidification conditions in alloys [9-11] to verify the segregation models.

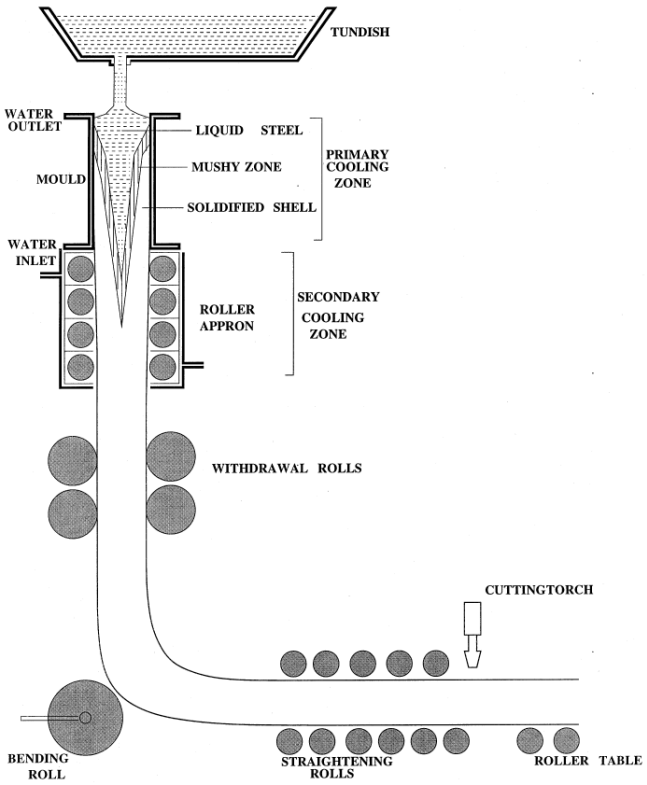

Figure 1-1 The schematic picture of continuous casting process [12].

Chapter 2 Cooling process, grain structure development and phase transformation during casting

2.1 Introduction

The cooling process during continuous casting process has a significant influence on the formation of microstructure and segregation in steel, and must be incorporated into segregation modelling. Grain structure development and phase transformation process (peritectic reaction and transformation and γ-austenite→α-ferrite transformation) during casting in steel which influence the formation and development of microsegregation and macrosegregation has been studied in this chapter.

2.2 Continuous casting process

The continuous casting technique for steels has been developed over several decades to provide shapes for subsequent processes, e.g. rolling processes. The different shapes for steel conclude billets with square cross section less than ~150 to 175 mm, thick slab with thickness between ~50 and 300 mm and thin slab with thickness between ~50 and 75 mm. The productivity depends on the casting speed which is determined practically according to alloy composition and cross section geometry. For steel slabs, the operating speed increases from 0.01mm/s [13] to over 0.08 mm/s as thickness decreases from 300 mm to 50 mm.

Heat transfer during continuous casting processes is complex, containing several mechanisms: convection in liquid, axial advection, heat conduction through the solid to the surface, convection to the mould called the primary cooling process, to the water-cooling system below the mould called the secondary cooling system and radiation in the bottom part called the radiative cooling process, as shown in Figure 2-1. For steel continuous casting, heat

transfer through the thickness of solid may dominate the overall heat transfer in the cross section [14].

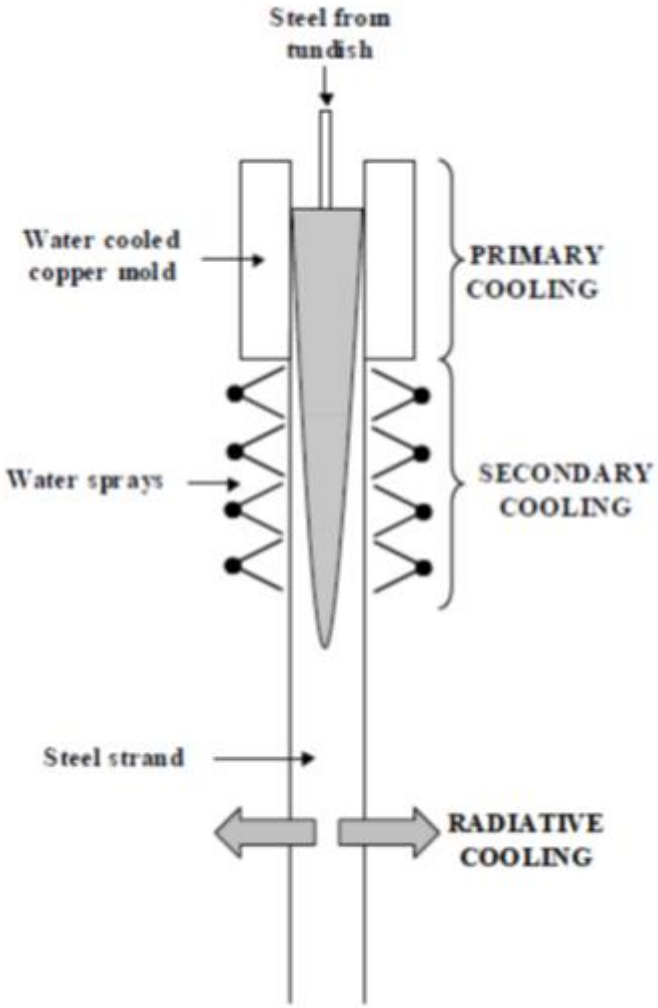

Figure 2-1 Schematic diagram of continuous casting of steel cooling process.

2.2.1 Primary cooling process (mould cooling)

Liquid metal flows from the tundish into the bottomless water-cooled copper mould (generally ~ 700 to 1200 mm in length) shown in Figure 2-1. A thin solid shell with thickness of about 10 to 20 mm forms against the mould wall and is strong enough to support the inner liquid core after leaving the mould. With increasing casting speed, the shell thickness at the

exit of the mould is reduced. Primary cooling in continuous casting refers to the heat transfer at the metal/mould interface. In steel continuous casting, the newly solidified shell keeps good contact with most of the mould wall because of the internal liquid pressure and the tapering process which is intended to offset the contraction of the shell.

2.2.2 Secondary cooling process (water cooling)

After leaving the mould, the strand is cooled by water spray or a combination of water and air (air-mist), referred to as secondary cooling. This section consists of a number of zones (5 to 9) [15, 16] with decreasing water flow rates as the distance below the meniscus increases. The series of water flow zones control temperature on the steel surface in order to minimise reheating and avoid cracking. The length of the liquid metal core is usually 5 to 30 m according to the operating speed and thickness of the strand. At the exit of the secondary cooling process, the centre of the steel slabs may be fully solid or still partially liquid depending on the processing parameters such as casting speed. The average temperatures across the section and surface temperatures of steel slabs after secondary cooling process reported by Wang et al.[15] are in a range of 1200 - 1300 ℃ and 1000 - 1100 ℃ respectively.

2.2.3 Radiative cooling during continuous casting of steel

After the water-cooling zone, the strand goes through the radiative cooling process and solidification is completed before any subsequent process, eg. rolling. The heat transfer in this stage is by air cooling which involves radiation, natural convection with air and conduction or diffusion in solidified steels. The governing equations for the different heat transfer mechanisms involved in radiative cooling are summarised below.

For heat conduction or diffusion in solidified steels, Fourier's law in the one-dimensional form can be used and shown in Equation 2-1:

$$\frac{q}{A} = -\frac{kdT}{dx} = \frac{dT}{R}, R = \frac{dx}{k} \quad 2\text{-}1$$

Where, q/A is the local heat flux density (W/m^2); q is heat transferred per unit time (W); A is cross-sectional surface area (m^2); k is thermal conductivity (W/(m·k)); dT/dx is temperature gradient in x direction (℃/m); R is thermal resistance (m^{2}k/W).

Thermal conductivity changes with temperature and composition. Peer et al predicted thermal conductivities in different steels and the prediction agrees well with the experimental results. Figure 2-2 shows the comparison of predicted and experimental thermal conductivities for 0.5C wt % steel (0.5C-0.5Mn-0.25Si, wt %).

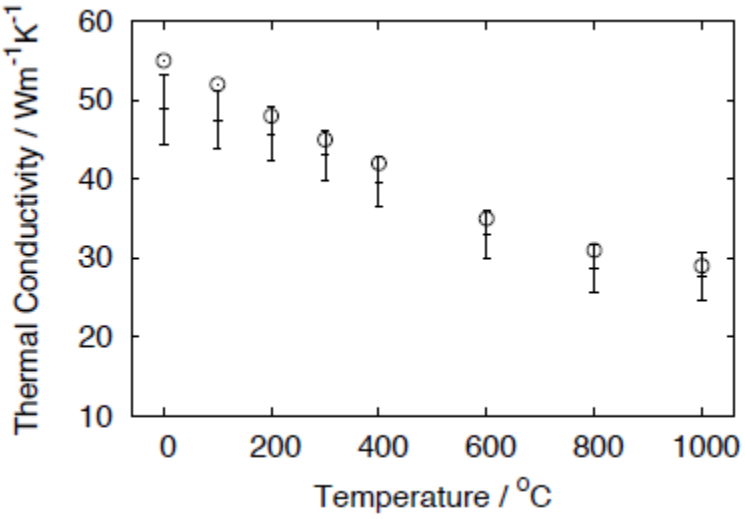

Figure 2-2 Predicted (with error bar) and experimental (circle) thermal conductivity as a function of temperature for 0.5C-0.5Mn-0.25Si wt% steel [17].

The equation used for convection can be expressed as follows:

$$q = H_c A dT \quad (2\text{-}2)$$

Where q is heat transferred per unit time (W); A is heat transfer area of the surface (m^2); H_c is the convective heat transfer coefficient (W/ (m^2·K)); dT is temperature difference between the surface and the bulk fluid (K or ℃).

Heat transfer coefficients depend on both the material and the fluid to which the heat is being transferred. For free convection to air, the range of heat transfer coefficient is 5 - 25 W/ (m^2·K), such as 7.9 W/ (m^2·K) for heat transferred from mild steel to air [18], it also depends on whether the fluid is moving and, if so, the velocity should be taken into account. The heat transfer coefficient is a property of a system, rather than of a material.

Heat transfer through radiation occurs in the form of electromagnetic waves mainly in the infrared region. If a hot object is radiating energy to its cooler surroundings the loss rate of net radiation heat can be expressed as

$$q = \varepsilon\sigma(T_h^4 - T_c^4)A \quad (2\text{-}3)$$

Where T_h is hot body absolute temperature (K); Tc is cold surroundings absolute temperature (K); A is area of the object (m^2); ε = Emissivity Coefficient of the object; σ = 5.6703 10^{-8} (W/m^2·K^4) - The Stefan-Boltzmann Constant.

Surface emissivity for steel changes with temperature and surface finish. For steel with an oxidised surface, emissivity coefficient at 300 K is approximately 0.79 [19].

2.3 Grain structure development during solidification

The grain structure in most castings has three distinct zones: the chill zone, columnar zone, and equiaxed zone, shown in Figure 2-3. Solidification starts with fast nucleation of equiaxed

crystals with random orientation in extremely supercooled liquid near the mould wall. The narrow band of small equiaxed crystals near the cold mould wall is called the chill zone. Due to the latent heat released by the first forming equiaxed grains, the nucleation rate dramatically decreases. Grains with preferred crystallographic orientation <100> which are most parallel to the direction of maximum temperature gradient grow fastest in the direction of heat flow usually normal to the mould wall. Those grains with a strong preference in orientation normal to the mould walls form the columnar zone. At the same time, spherical, randomly oriented crystals with isotropic properties are formed by nucleation in the most constitutionally supercooled inner liquid and on broken dendrite arms from columnar zone crystals transported by liquid flow into the centre [20, 21]. The equiaxed zone in the centre of the mould consists of equiaxed grains with much larger size than those in the chill zone.

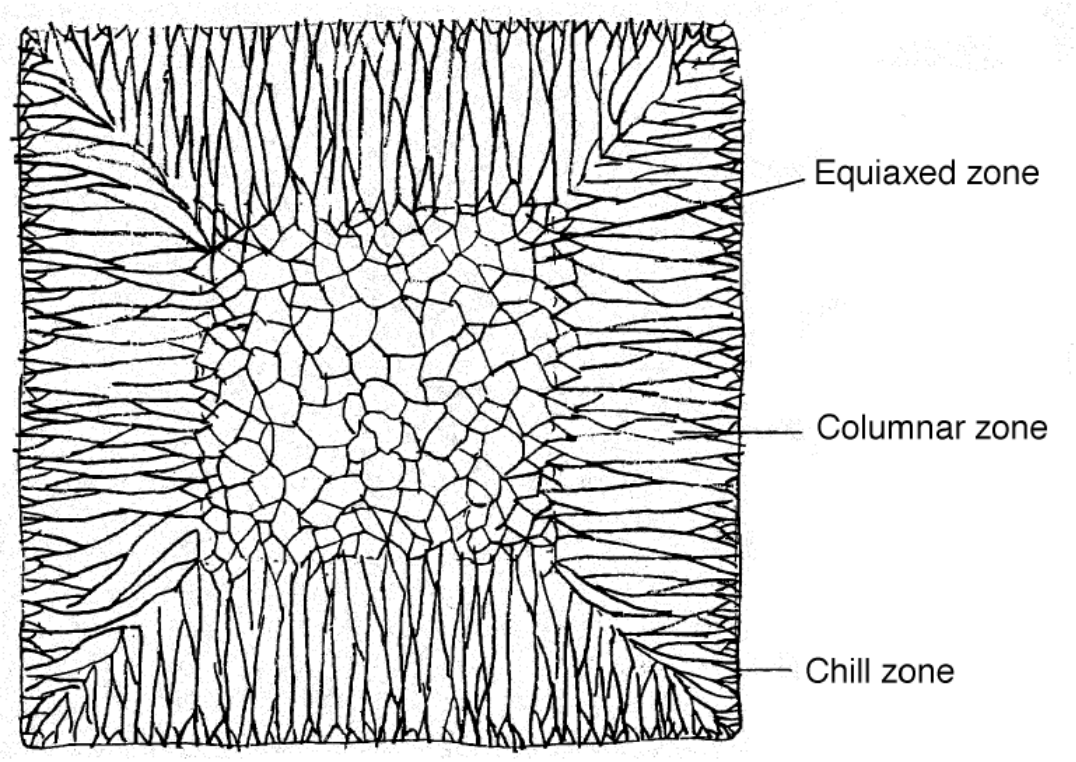

Figure 2-3 Characteristic grain structure in a cross section of as cast steel [22].

The transition from columnar grains into equiaxed grains called CET plays a very important role in the formation of centreline segregation and inner cracks, in the continuous casting process. Increasing the area of the columnar region can worsen the centreline segregation [23].

2.3.1 Cellular and dendritic solidification

Constitutional supercooling has important effects on the solidification morphology. Due to solute partitioning between the solid and liquid during solidification, the solute rejected to the liquid produces a solute-enriched layer in front of the solidifying interface (Figure 2-4 b). According to the phase diagram (Figure 2-4 a), the liquidus temperature increases as the distance from the interface increases shown as line T_L in Figure 2-4 (c).

Regardless of convection, the criterion of constitutional supercooling can be expressed by Equation 2-4 [20].

$$\left(\frac{G_L}{R}\right) \geq \left[\frac{m_L C_O (1-k)}{k D_L}\right] \qquad 2\text{-}4$$

Where, G_L is the actual temperature gradient near the interface in the liquid; R is the growth velocity; m_L is the slope of the liquidus line; C_0 is the bulk composition; k is the partition coefficient and D_L is the diffusion coefficient in the liquid.

If the ratio (G_L/R) in front of the interface is above the critical value indicated by the line T_1 in Figure 2-4 (c), a perturbation formed by an instability on a flat solid-liquid interface will melt back and the interface will continue to solidify in a planar manner. As the ratio (G_L/R) goes down below the critical value, such as line T in Figure 2-4 (c), a supercooled zone appears in front of the interface as shown in Figure 2-4 (c). Under these conditions, any perturbation will be projected into the supercooled liquid and so will be stabilised to a

distance at which the T and T_L line cross. Growth will be cellular along the direction of heat flow and dendritic as the stabilised distance increases further.

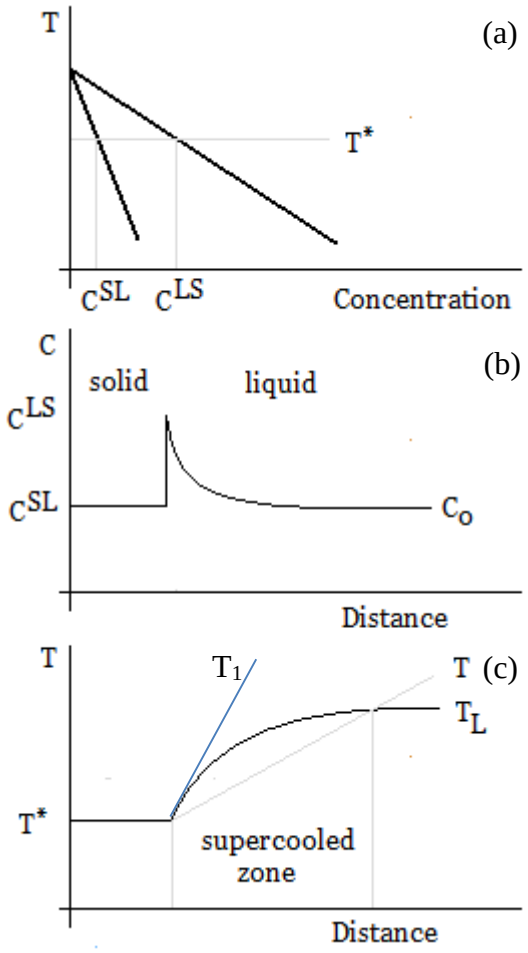

Figure 2-4 Constitutional supercoiling during solidification (a) phase diagram; (b) solute concentration in front of the S/L interface; (c) constitutional supercooled region.

The cellular structures are stable only in a certain temperature gradient range. Normally cells grow normal to the interface at relatively low growth rates and reject solute element atoms which pile up in the intercellular regions. With increasing growth rate, crystallographic effects start to make a difference and the cells grow towards the preferred crystallographic growth

direction (<100> for cubic structure). Therefore, secondary dendrites or even tertiary dendrites start to form on the stem of columnar structures to form dendritic geometry.

In continuous casting, dendritic solidification in steels occurs in both columnar and equiaxed zones. G and R are important in optimising the operational parameters in terms of decreasing the risk of internal defects. Both the growth rate R and thermal gradient G depend on the cooling rate and decrease with increased distance from the surface [24]. If the dendrite growth rate is too slow, the shell thickness is thin enough that break-out may happen. If the dendrite growth is too fast, defects may form in the final product. The growth rate and thermal gradient in continuous casting of steel reported by previous research are 0.05 mm/s - 6.0 mm/s and 129 K/mm - 0.3 K/mm respectively [24-26].

2.3.2 Coarsening

Coarsening may happen during dendritic solidification by two main mechanisms: (1) growth of larger dendrite arms at the same time as smaller dendrite arms disappear (ripening); (2) filling in the space between two adjacent dendrite arms to merge them into one larger dendrite arm (coalescence). Duing the early stages of solidification, ripening happens by dissolving the small dendrite arms as shown in Figure 2-5 (b), while at the final stage of solidification, coalescence occurs by filling in the space between two dendrite arms, Figure 2-5 (b) [27].

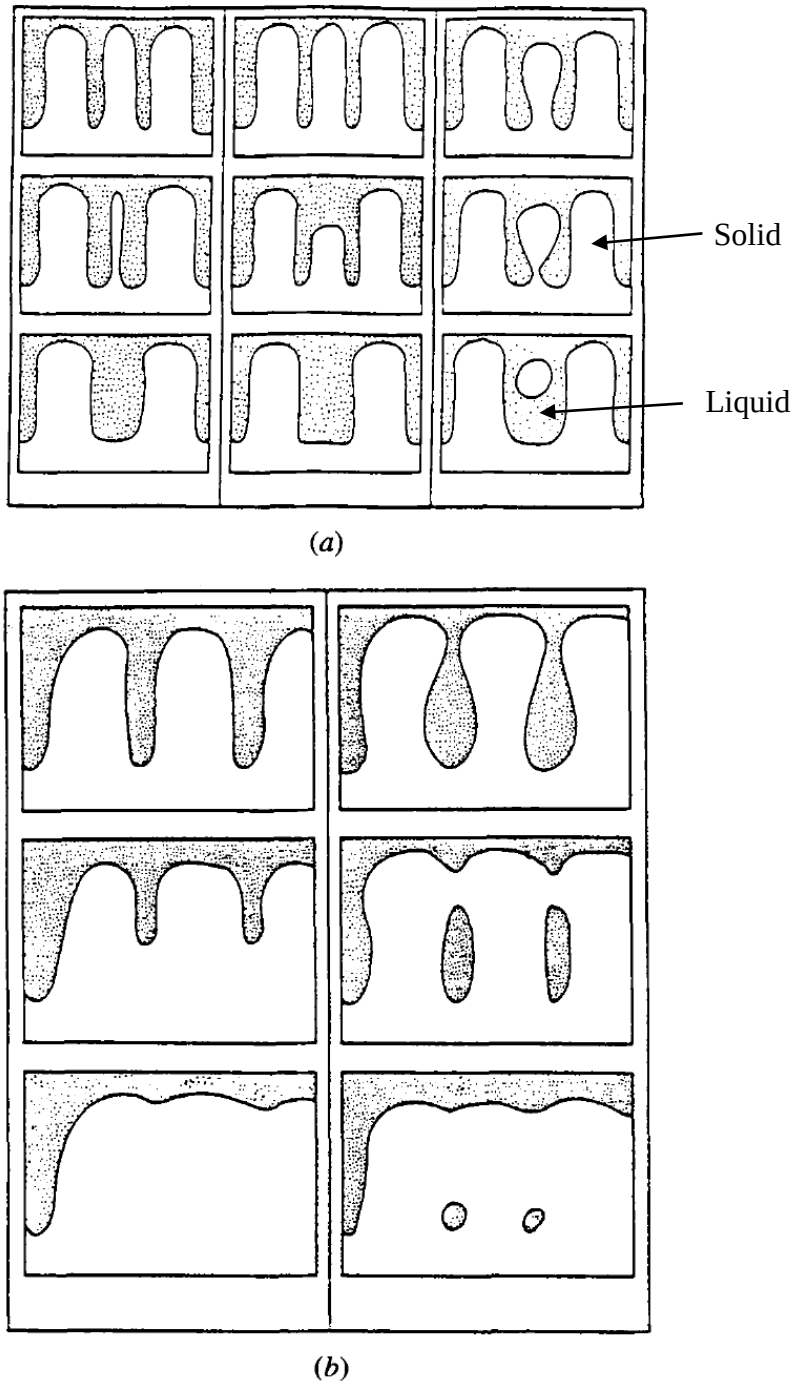

Figure 2-5 Schematic diagrams of coarsening mechanisms: (a) ripening and (b) coalescence.

The ripening happening at the earlier stage of solidification should reduce the level of microsegregation in the solid [28, 29]; the latter stage of coalescence was expected to have

little effect on the level of segregation. The effect of coarsening on microsegregation is small compared with the back-diffusion in solid [30].

2.4 Phase transformation during casting in steels

2.4.1 Peritectic reaction and transformation in steel

Steel solidification processes can start with the precipitation of δ ferrite or austenite (γ) according to alloying element contents and cooling rates. Segregation behaviour during the primary precipitation of ferrite is different from that of austenite due to the different partition coefficients between ferrite and liquid or austenite and liquid and the diffusion coefficients between ferrite and austenite.

In the case of primary precipitation of δ ferrite, many steels solidify partially through peritectic reaction and transformation, such as in the iron-carbon system with a carbon content of 0.09 - 0.53 wt %. The definition of the peritectic reaction and transformation was introduced by Kerr et al. [31]. In the peritectic reaction, all the phases (primary phase, secondary phase and liquid) are in contact with each other and the secondary phase grows along the interface of the primary phase and liquid. During the peritectic transformation, the secondary phase isolates and grows into the primary phase and the liquid. The peritectic reaction is rapid and is generally accepted to be controlled by the diffusion of solute in the liquid phase [32, 33] and the peritectic transformation is controlled by diffusion through the secondary phase [34]. However, the peritectic reaction rates (1.5 - 5.5 mm/s) in an Fe-C alloy at a cooling rate of 20 K/min measured by high-temperature laser-scanning confocal microscopy (HTLSCM) were found to be too rapid to be explained by a carbon diffusion mechanism, indicating that either massive transformation, Singh et al. [35] or precipitate type transformation, Takahashi [36], controls the reaction rate [37, 38]. Similarly, the

transformation from δ-ferrite to austenite in Fe-0.14C steel at a cooling rate of 10 - 20 K/min was finished within 1/30-2/30 seconds and can not be explained by carbon diffusion mechanism.

The peritectic reaction and transformation affects the segregation sequence through the difference in diffusion coefficients of the alloying elements in austenite and ferrite. The stress related to the solidification shrinkage and $\delta \rightarrow \gamma$ transformation can deform the very thin solidified shell and detach the shell from the mould wall during continuous casting processes. Longitudinal cracking caused by the contraction on peritectic solidification in hypo-peritectic steel during continuous casting has been found [39].

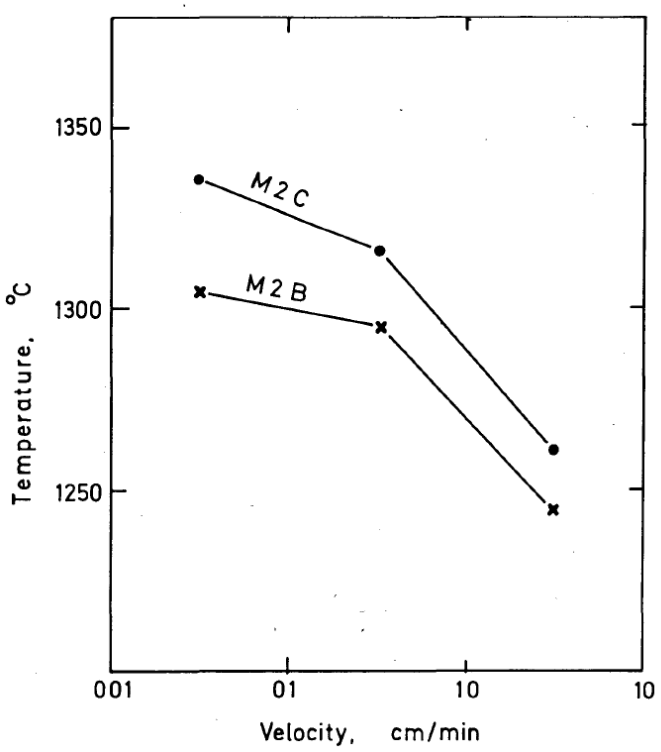

Figure 2-6 Peritectic temperature as a function of solidification rate.

The austenite-stabilising elements enhance a peritectic reaction, while the ferrite-stabilising elements promote a eutectic reaction during the solidification process [40]. The ferrite-

stabilizing elements have been found to segregate to ferrite during the δ →γ transformation [41]. The influence of the addition of one element into Fe-C to form a ternary system on peritectic temperature has been investigated by Kagawa [42]. Alloying elements S, P, Ti, Si, Mo, and W reduce the peritectic temperature significantly. By introducing Mn, Co, Ni, and Cu, the peritectic temperature was increased. The peritectic temperature was observed to decrease with increasing cooling rate in high alloy steels, Figure 2-6 [41].

2.4.2 Growth of α-ferrite in steels

The growth of α-ferrite is controlled by interstitial and/or substitutional diffusion and interface movement [43]. This problem was addressed by taking an example of ternary steel, Fe-C-Mn. A schematic diagram of concentration profiles at the α-ferrite/austenite interface is shown in Figure 2-7 and $C^{\gamma\alpha}$ and $C^{\alpha\gamma}$ are elemental content in γ phase and α-ferrite respectively at the α/γ interface. The far field concentration in austenite $\bar{c}$ was assumed to be constant.

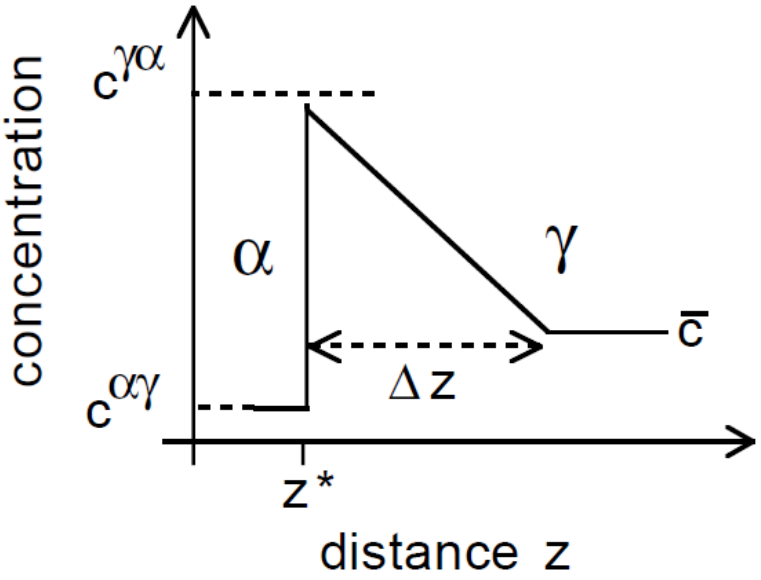

Figure 2-7 Schematic concentration profile at the interface of ferrite and austenite during diffusion controlled growth.

For each of the species, two equations must be satisfied simultaneously in terms of mass conservation as follows:

$$\begin{aligned}(c_c^{\gamma\alpha} - c_c^{\alpha\gamma})v &= -D_c \nabla C_c \\ (c_{Mn}^{\gamma\alpha} - c_{Mn}^{\alpha\gamma})v &= -D_{Mn} \nabla C_{Mn}\end{aligned} \qquad 2\text{-}5$$

Where v is interface velocity, ∇C is concentration gradient at the position of interface. D is the diffusion coefficient in austenite. The right hand side is the diffusion flux from the interface. In these equations, the cross effect of elements on the diffusivity was neglected. The concentration at the interface are determined by a tie-line from a phase diagram, Figure 2-8.

As $D_c \gg D_{Mn}$, the tie-line needs to be chosen to satisfy both equations. If the tie-line allows $c_c^{\gamma\alpha} \to \bar{c}_c$, Figure 2-8 (a), ∇C will be very small and hence the flux of carbon is decreased to be consistent with Mn diffusion. This mechanism for the ferrite growth is called Partitioning, Local equilibrium (P-LE) with the feature that $c_{Mn}^{\alpha\gamma}$ can be dramatically different from $\bar{c}_{Mn}$ resulting in long range diffusion of Mn into austenite.

Another choice of tie-line is such that $c_{Mn}^{\alpha\gamma} \to \bar{c}_{Mn}$ so that ∇C_{Mn} is significantly increased. The flux of Mn atoms at the interface is increased and can keep pace with the carbon. This growth mode is called Negligible Partitioning, Local Equilibrium (NP-LE), with the feature that the Mn content in the ferrite at the interface is almost equal to $\bar{c}_{Mn}$.

Ferrite growth from austenite can occur at a constrained equilibrium called Paraequilibrium (ParaE) at temperatures where the diffusion of substitutional solutes stops but interstitials may still be active. In Fe-C-Mn steel, Mn stops partitioning at the interface and only carbon redistributes.

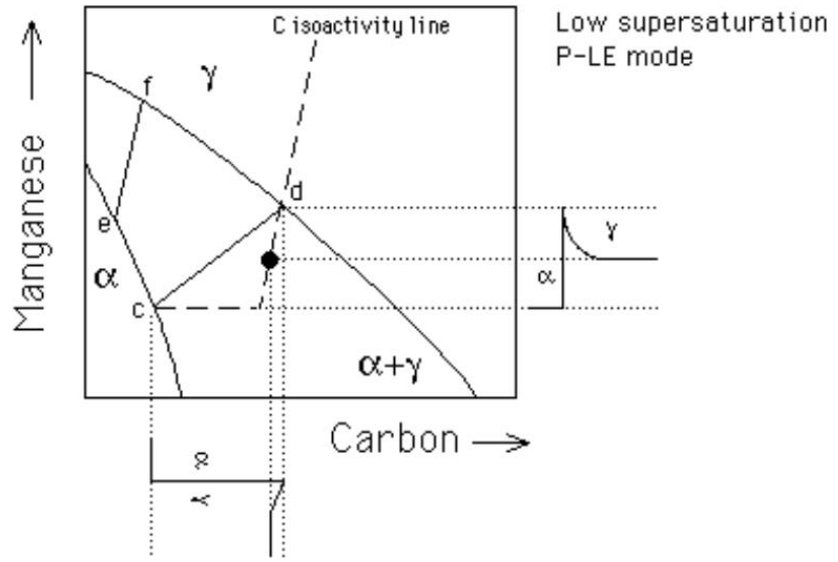

(a)

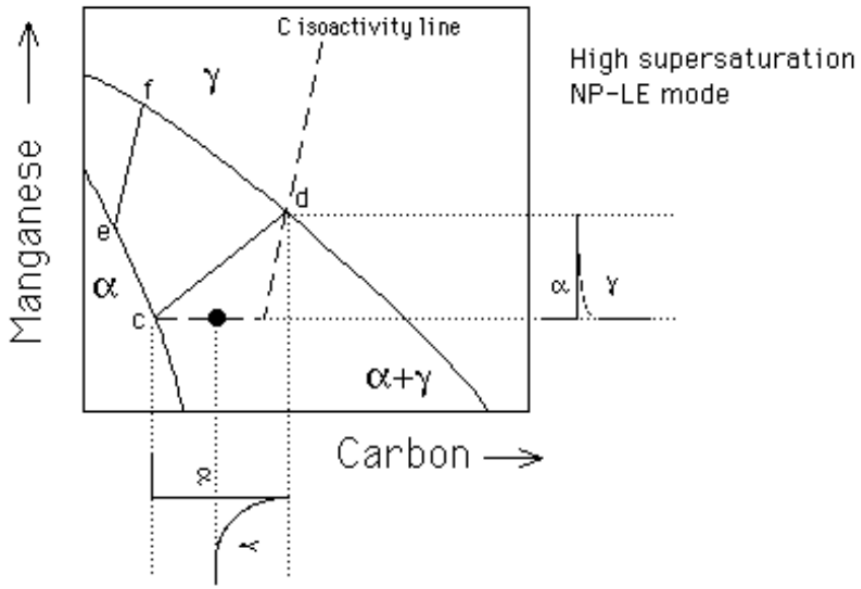

(b)

Figure 2-8 Schematic isothermal section of a phase diagram in the Fe-C-Mn ternary system illustrating different ferrite growth mechanisms at the interface: (a) P-LE mode and (b) NP-LE mode, the black dot in each case represents the bulk composition.

Chapter 3 Segregation characterisation

3.1 Microsegregation

Microsegregation is generally caused by freezing of solute-enriched liquid in the interdendritic spaces. During solidification, most solute atoms are rejected from the growing solid into the interdendritic liquid, because there is less solubility for these elements in the solid compared with that in the liquid phase. Rejection of solutes results in lower solute concentrations in the primary solid than that in the liquid. This microsegregation is on the scale of the solidification structure, i.e. dependent on solidification rate.

3.1.1 Distribution of alloying elements in steels

Alloying elements in steel can exist (i) in the free state; (ii) as intermetallics with iron or with each other; (iii) as nonmetallic inclusions such as oxides, sulfides; (iv) as carbides; or (v) as a solution in iron [44]. There are two different types of alloying element in terms of their distribution characteristics in steel.

The first group of elements (e.g. Ni, Si, Co, Al, Cu and N) do not react with iron and carbon, so that they can only be present in the form of solid solutions in steel. But Cu and N are exceptions. If the copper content is more than 7 wt %, pure copper will exsolve in the form of free metal inclusions. If N content exceeds 0.015%, nitrogen with iron or other alloying elements (V, Al, Ti, and Cr) will form nitrides.

Alloying elements in the second group (e.g. Cr, Mn, Mo, W, V, Ti, Zr, and Nb) can form stable carbides in steel. The enthalpies of formation of carbides, nitrides and borides are shown in Figure 3-1. The distribution of these elements is dependent on the content of carbon and other carbide-forming elements in the steel. If carbon content is relatively low and the

content of an alloying element is high in steel, then, carbon will be used for carbides before the alloying element atoms are fully used. Consequently excess carbide-forming elements will exist in the form of solid solution. If a steel contains a high quantity of carbon and small amount of the alloying elements, the carbide forming element will be found in the steel mostly as carbides.

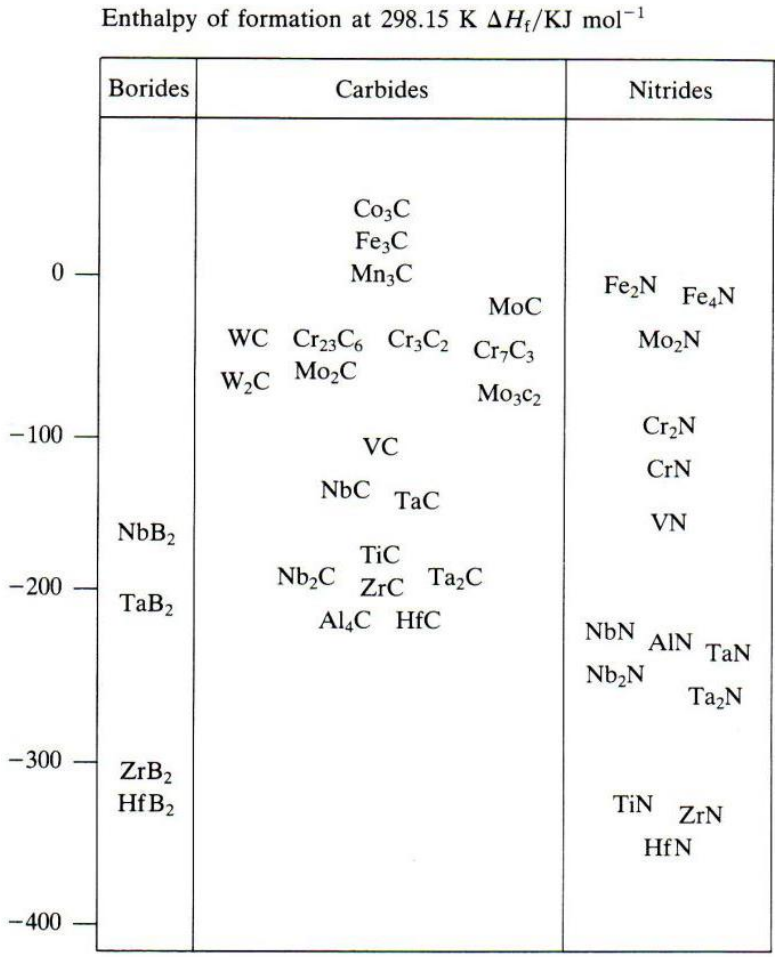

Figure 3-1 Formation enthalpies of selected carbides, nitrides and borides.

Elements such as Ni, Si and Mn do not form carbides in competition with cementite, and consequently do not change the microstructures formed. However, strong carbide-forming elements such as Nb, Ti and V are able to form alloy carbides even when the alloying concentration is less than 0.1 wt% and consequently significant changes in the steel

microstructures would be expected with these elements. The segregation can be characterised by the distribution of precipitates.

3.1.1 Element partition behaviour during solidification

During phase transformation, solute element atoms can partition between two adjacent phases. The partition coefficient k is the ratio between the elemental concentration in solid to that in liquid or in two different solid phases and is used to describe the partition tendency of each element. During solidification, if k is less than 1, the solute will be enriched in the liquid phase. The degree of segregation of elements to the liquid phase with low partition coefficients (k<1) in steel is high. If the liquid solidified directly as δ or γ solid phase, then the microsegregation can be characterised by the partition coefficient k_δ or k_γ, respectively.

Partition coefficient values can be obtained from phase diagrams according to concentrations at the interface of two different phases. Table 3-1 shows equilibrium partition coefficients of elements between the δ-phase and γ-phase with liquid: these values are assumed to be independent of temperature and are determined from binary phase diagrams. Nb and Ti have a higher tendency than other substitutional elements to segregate into liquid.

Elements, such as Si and Nb, which are ferrite stabilisers have lower k values in austenite than in δ-ferrite indicating a lower solubility in austenite than in δ-ferrite. Therefore interdendritic segregation of these elements at the austenite/liquid interface is greater than that at the δ-ferrite/liquid interface. In contrast, the austenite stabilisers, such as Mn, Ni show the opposite partition behaviour to ferrite stabilisers.

Phase diagrams in multicomponent systems have been successfully obtained by Thermo-Calc developed based on the Gibbs energy calculation by STT Foundation (Foundation of

Computational Thermodynamics, Stockholm, Sweden) [45-48]. Equilibrium partition coefficients determined from Thermo-Calc-derived phase diagrams has also been used as parameters in some non-equilibrium models in steels [49, 50].

Table 3-1 Equilibrium partition coefficients and diffusion coefficients of solute elements in δ-ferrite and in austenite

Element	$k^{\delta/L}$[4]	$k^{\gamma/L}$	D^{δ} (cm^2/s) [16]	D^{γ} (cm^2/s)
C	0.19	0.34	0.0127 Exp(-81379/RT)	0.0761 exp(-134429/RT)
Si	0.77	0.52	8.0Exp(-248948/RT)	0.3Exp(-251458/RT)
Mn	0.76	0.78	0.76Exp(-224430/RT)	0.055Exp(-249366/RT)
P	0.23	0.13	2,9Exp(-230120/RT)	0.01Exp(-182841/RT)
S	0.05	0.035	4.56Exp(-214639/RT)	2.4Exp(-223426/RT)
V	0.93	0.63	4.8Exp(-239994/RT)	0.284Exp(-258990/RT)
Nb	0.4	0.22	50Exp(-251960/RT)	0.83Exp(-266479/RT)
Cr	0.95	0.86	2.4Exp(-239785/RT)	0.0012Exp(-218991/RT)
Ti	0.38	0.33	3.16Exp(-247693/RT)	0.15Exp(-250956/RT)
Ni	0.83	0.95	1.6Exp(-239994/RT)	0.34Exp(-282378/RT)

Notes: R is gas constant of 8.314 Joule/mol K, and T is the temperature in Kelvin.

3.1.2 Microsegregation during cellular and dendritic solidification

When cells grow into liquid, solute elements ($k \leq 1$) build up in intercellular liquid. It is convenient to analyse the microsegregation by taking a volume element. In cellular solidification, the volume element (Figure 3-2(a)) has a small thickness in the growth direction and extends a distance L from the centre of a cell to the midpoint between two cell tips. The solute was rejected as the cells thicken diffusing towards both the centre of the cell and the liquid, so the solid and liquid are not of uniform composition. The cross-section

segregation of Mn in cellular structure of directionally solidified steel is shown in Figure 3-3. Higher Mn concentration was located in the intercellular region.

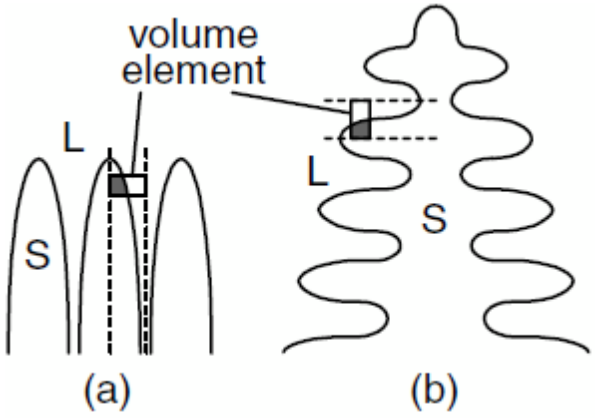

Figure 3-2 Volume elements for solute redistribution analysis in (a) cellular solidification; (b) dentritic solidification.

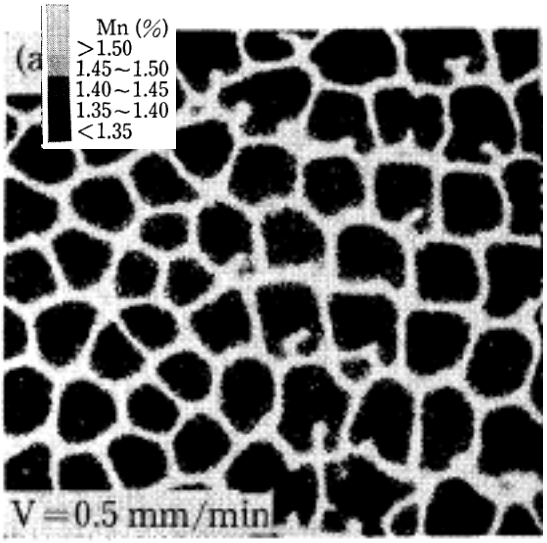

Figure 3-3 Mn segregation on cross-section of directional solidification in cells at withdrawal rate of 0.5 mm/min [51].

Dendritic solidification occurs in both columnar and equiaxed zones of continuously cast steel [52]. The solidifying metal consists of three regions, solid, liquid and mushy zone in which both dendritic solid and interdendritic liquid exist at the same time. The secondary dendrite

arms form on the stems of primary dendrites. A volume element with length of L taken from the centre of dendrite to the middle point of two adjacent secondary dendrite arms can be used to show the formation of dendritic microsegregation in Figure 3-2 (b). During solidification, the solid grows from one end of the volume element (the centre of the dendrite arm) to the other end (interdendritic region) and solute is rejected by the solid and enriched in liquid ($k \leq 1$) as the dark area in volume element increases. When the secondary arms on one primary dendrite impinge on the secondary arms on the adjacent primary dendrite (which has been found to occur when the solid fraction $f_s \approx 0.9$), the solute rich liquid was trapped in the interdendritic region and the surrounding liquid could not be accessible.

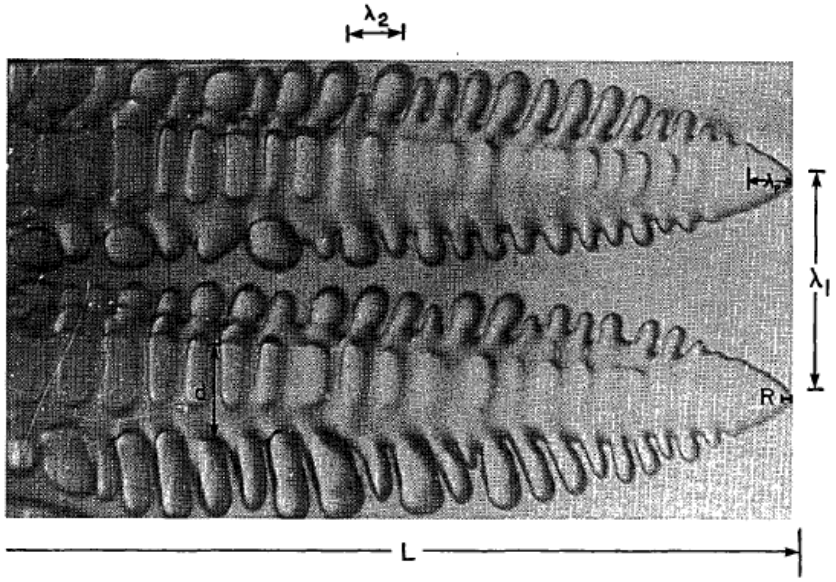

Figure 3-4 Dendritic structure with important length scales [53].

The segregation pattern is largely influenced by the microstructural length scales of dendrites, especially secondary dendrite arm spacing (SDAS). A dendritic structure is characterised by several important length scales, as shown in Figure 3-4. These are: the dendrite tip radius R, the primary dendrite arm spacing (for directional growth only) λ_1 and the secondary dendrite arm spacing λ_2.

3.1.3 Measurement of secondary dendrite arm spacing (SDAS)

One of the measurements of the scale of microsegregation is the secondary dendrite arm spacing (SDAS) which separates the solute-rich and solute-deleted regions determined by conditions of solidification. Solidification rate is one of the important factors to influence the SDAS. Figure 3-5 shows that, with increasing cooling rate, the SDAS decreases [22]. Generally, with increasing distance from the cold mould wall, cooling rate reduces which leads to an increase in SDAS, shown in Figure 3-6 [22]. From Figure 3-7, in 50 mm thick 1020 steel slab, the SDAS at subsurface is about 60 μm and at quarter thickness it is 120 μm corresponding to the decreasing cooling rate.

Won et al. obtained an equation (Equation 3-1) which expresses the relationship between SDAS, cooling rate and carbon content by fitting experimental data in Figure 3-8 [54]:

$$\begin{aligned} \lambda_{SDAS} &= \left(169.1 - 720.9 \cdot (\%C)\right) \cdot C_R^{-0.4935} \quad \text{for } 0 < (\%C) \leq 0.15 \\ &= 143.9 \cdot C_R^{-0.3616} \cdot (\%C)^{(0.5501 - 1.996(\%C))} \quad \text{for } 0.15 < (\%C) \end{aligned} \qquad \text{3-1}$$

Where C_R is the cooling rate (℃/s) and (%C) is the carbon content (wt % C).

From Figure 3-8, when the carbon content is close to 0.15 wt %, the experimental points from each cooling rate overlap. So, this equation can only roughly predict the SDAS with carbon content and solidification rate.

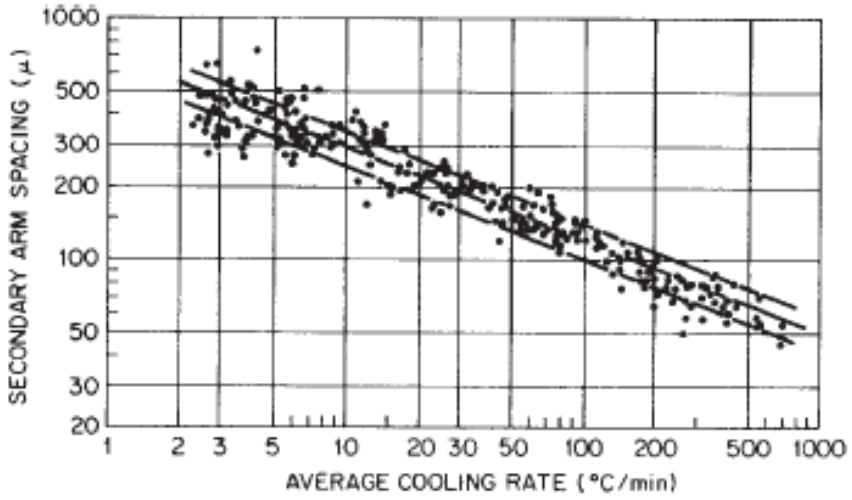

Figure 3-5 SDAS against cooling rate from commercial steels with 0.1 to 0.9% C [22].

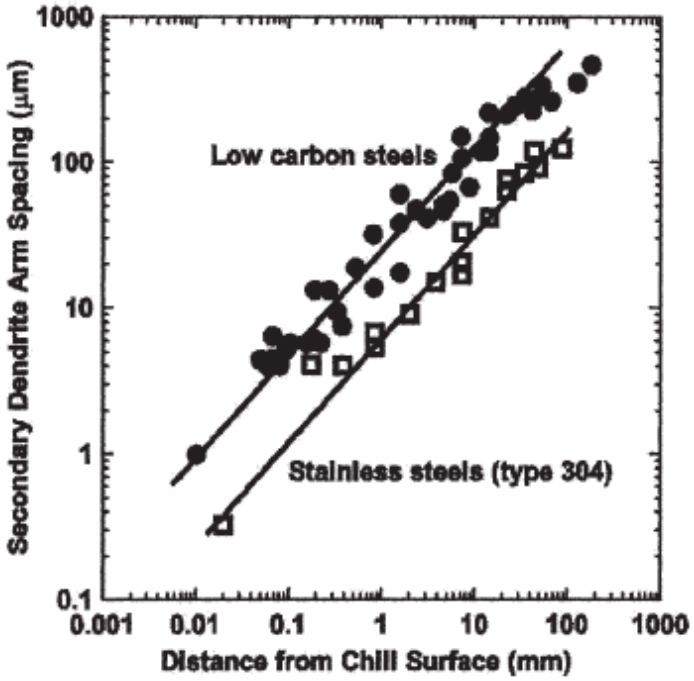

Figure 3-6 SDAS against distance from chill surface of different low-carbon and stainless casting steels [22].

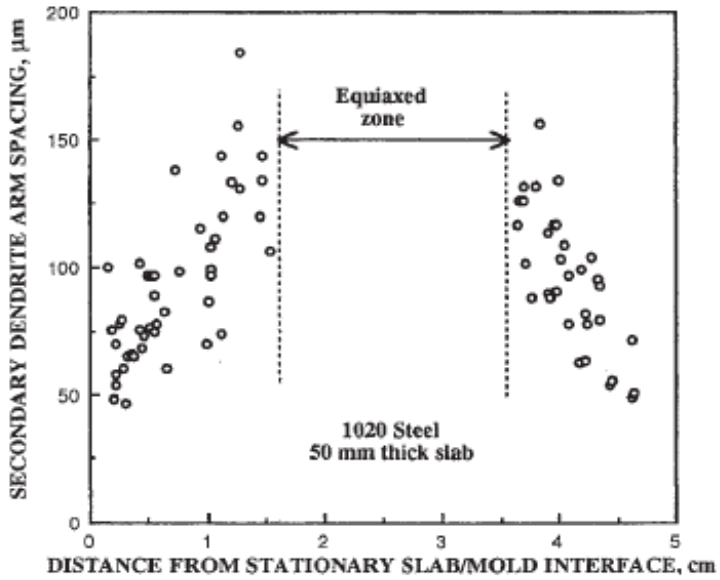

Figure 3-7 SDAS against distance from stationary slab/mould interface for a 50 mm thick as-cast slab of 1020 steel.

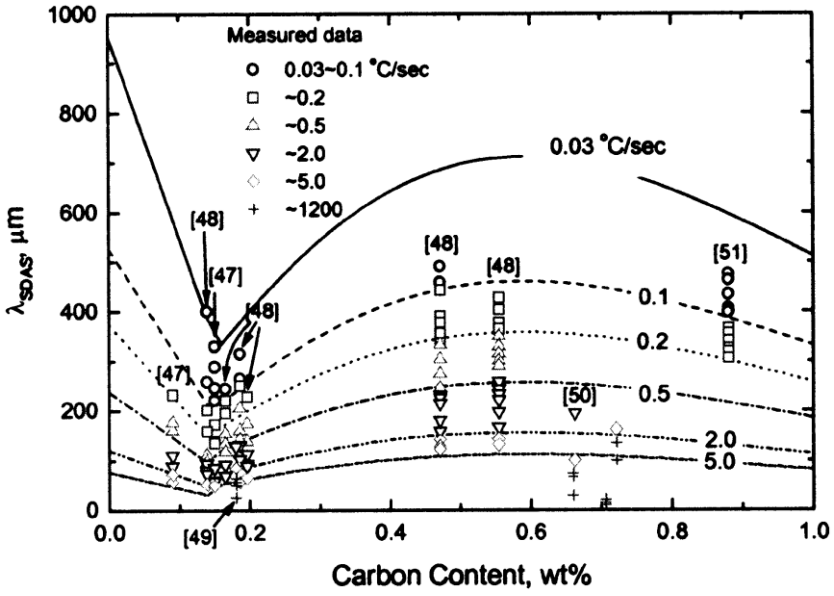

Figure 3-8 Compared calculated SDAS with experimental SDAS as a function of carbon content at different cooling rates [54].

3.2 Measurement of microsegregation

The interpretation of microsegregation during solidification is very important to optimise processing and control composition and the mechanical properties of the final product. To some extent, characteristics of interest are segregation range (minima, maxima) and the composition profiles on the scale of dendrites. Data from some dendritic regions are required and the process used for this can have a strong effect on the results and the assessment of microsegregation. Commonly, microsegregation is measured in 2D plane, but the spatial chemical variation between dendritic and interdendritic areas is 3D. However, all the characteristics in the 3D material can be investigated on a 2D section as long as the investigated regions are big enough. Microsegregation is characterised by analysing elemental distribution, generally by use of scanning electron microscope–energy dispersive spectroscopy (SEM-EDS) or electron microprobe analysis with wavelength dispersive spectrometry (EMPA-WDS). The limitation of detection for EDS is 0.1 - 0.3 % and the precision of EDS detection is approaching ± 0.1%. The WDS have lower limitation, 0.003 - 0.03 %. Typical methods of determination of microsegregation are segregation ratio, line-scans and cumulative profiles.

3.2.1 Segregation ratio

The segregation ratio, *s*, can be defined as follows,

$$s = \frac{C_{max}}{C_{min}} \tag{3-2}$$

Where C_{max} is maximum element concentration; C_{min} is the minimum element concentration.

This method is used commonly to characterise the level of microsegregation for each element. Turkeli used segregation ratio to investigate the effect of composition and cooling rate on Mn

segregation in Fe-C-Mn steels during unidirectional solidification [55]. The segregation levels of microalloying elements in three as-cast continuous steels are listed in Table 3-2. In these steels, the Nb segregation ratio is about 2.5-2.7, higher than those of Ti, V and Al, which are about 1 - 1.3 [6].

Table 3-2 Segregation levels of microalloying elements in 3 continuously cast steel slabs.

Slab Location	Nb (Wt Pct)	Ti (Wt Pct)	V (Wt Pct)	Al (Wt Pct)
Slab 1, interdendritic	0.075	0.0024	0.056	0.048
Slab 1, dendrite center	0.027	0.0018	0.047	0.041
Slab 2, interdendritic	0.050	0.001	0.055	0.031
Slab 2, dendrite center	0.020	0.001	0.047	0.026
Slab 3, interdendritic	0.040	0.010	—	0.039
Slab 3, dendrite center	0.016	0.008	—	0.032

3.2.2 Line-scans

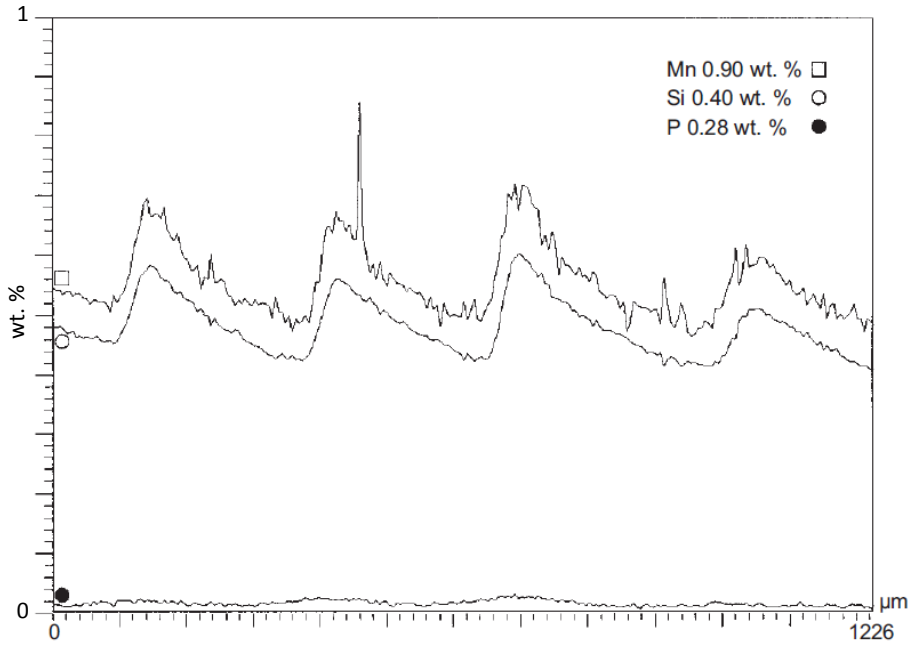

Figure 3-9 Saw-tooth profiles of Mn, Si and P by line-scans from a high carbon steel [56].

Line-scans present the composition changes with positions along a selected line. Information is kept in terms of variable length scale. The segregation in columnar grains can be measured

along a chosen line crossing a few secondary dendrite arms. Any abnormal segregation features such as saw-tooth profiles (Figure 3-9) can be shown by line-scans. However, the line-scans method is based on 1-D data so that it may lose some segregation features of 3D dendrite structures such as the maximum element concentration in the most segregated region.

3.2.3 Cumulative profiles

Cumulative profiles are obtained by sorting the composition data for each element from a grid of points into compositional profiles as a function of volume fraction. A cumulative compositional profile shows the composition proceeding with solid fraction increasing. This technique was performed to verify solidification models [57, 58] and has achieved primacy as it avoids the subjective selection of a line crossing solute-rich and solute-depleted regions and creates a continuous concentration profile rather than several discrete points[59]. Also, it does not demand special solidification conditions to show clear dendrite structures. This technique with 100 or more grid points can statistically give a similar trend to the real segregation with reasonable accuracy [60, 61].

3.2.3.1 Flemings-Gungor sort

The random sampling approach, first proposed by Flemings et al. [62], is the most widely used method to quantitatively characterise microsegregation, and is generally called area scan technique [57, 63]. The composition of 100 or more points acquired on a square/rectangular grid for a polished sample with the interval between two adjacent grid points more than SDAS is systematically measured [64, 65]. According to their segregation behaviour, the data for each element are then respectively ranked into gradually ascending or decending series based on concentration, without considering their sampling locations, to create successive composition profiles. Presuming that the solid concentration at the liquid/solid interface is a

function of continuously increasing fraction solid, regardless of back-diffusion in the solid during solidification and interdiffusion during cooling, then these curves can be considered as microsegregation profiles from the initial to completed solidified areas.

However, this method used in multicomponent alloys can cause misleading errors [56, 57], as local compositional maxima or minima due to the formation of new phases are lost when sorting composition data for each solute independently. Further, the cumulative profiles contain errors caused by random errors of analysis[56]. Moreover, each sampling point should be consistent with a unique solid fraction, but the independent sorting does not preserve this feature which causes the elemental total at each assigned fraction solid to deviate from 100 % (Figure 3-10).

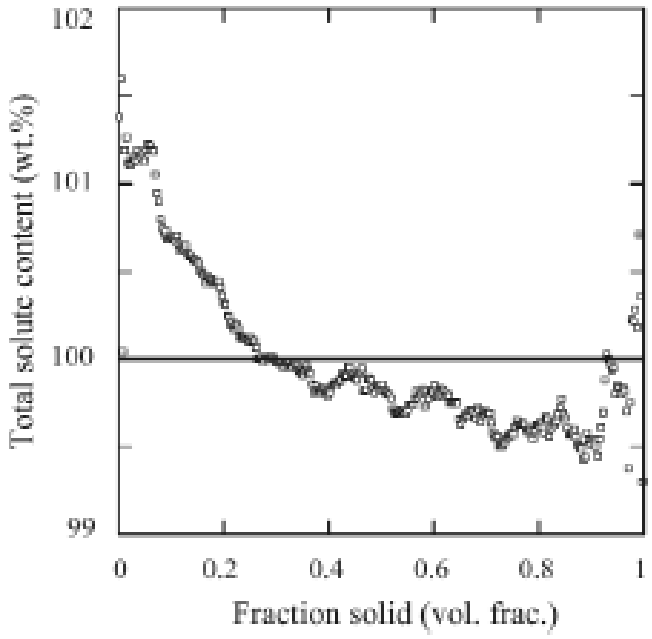

Figure 3-10 Total solute content as a function of solid fraction using F-G method. 100wt % is marked as a solid line.

A unique fraction solid is needed if the dendrite composition is built up from the compositional data, which would be used to compare with solidification models [66]. Finally, the compositional range for each element can be overestimated due to counting in the signal of the noise element.

3.2.3.2 Single element sort

Other approaches have been proposed to overcome some of the problems stated above. One of them is single element sorting (SES): the compositions of all the elements are sorted according to the concentration of one single element for which the segregation direction is known. The common relation is one component concentration was sorted against another obtained at the same analysis point. When the measurements of one chosen element were sorted into ascending ($k < 1$)or descending order ($k > 1$) the other element concentrations can be contemporaneously ordered against that chosen element. The local maximum and minimum for Mn profile in aluminum 7050 were observed by Xie et al. when Cu contents were sorted and other element contents were plotted directly [57]. SES has been applied in Ti-Al-Cr-Nb Alloy by Charpentier et al to characterise the segregation of Al, Cr and Nb [67].

3.2.3.3 Different sort

In different sorting methods, the difference of concentration between two selected elements are calculated and sorted into descending or ascending order according to the segregation direction of both elements. Other elements are ranked based on the sorting of the pre-selected pair of elements. This technique was applied in CMSX 4 by Karunaratne et al.[68] to analyse the segregation behaviour by using Ta-Re pair according to their opposite segregation directions.

However, both single element soring and different sorting methods need to appropriately select the elements on which the sorting is based. The universal sorting technique [66] proposed by Genesan et al. is able to implement all the data avoiding the subjectivity of choosing elements and distribute the uncertainty in the concentration profiles.

3.2.3.4 Weighted interval rank sort

From the measured composition data series of each element, *j*, the minimum and maximum of measured concentrations are identified. The measured concentration, C_i^j, at each grid position is weighted according to

$$\bar{C}_i^j = \frac{C_i^j - C_{MIN}^j}{\sigma^j} \quad 3\text{-}3$$

for an element segregated into the interdendritic region ($k < 1$), and

$$\bar{C}_i^j = \frac{C_{MAX}^j - C_i^j}{\sigma^j} \quad 3\text{-}4$$

for an element segregated into the dendritic core ($k > 1$).

Where σ^j is the uncertainty in concentration for the measured element, j. For each concentration, $\bar{C}_i^j$ varies between 0 and $(C_{MAX}^j - C_{MIN}^j)/\sigma^j$. The values at each measured position are next averaged, ranked in ascending order and given a rank number, Ri from 1 to the total number of points N.

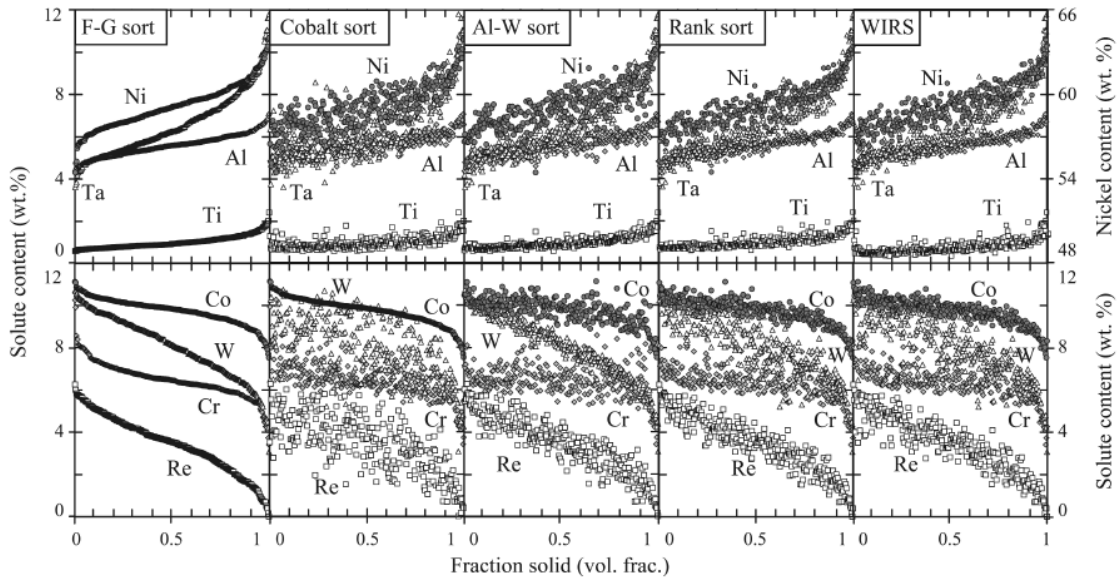

Figure 3-11 Segregation profiles of alloying elements in CMSX-4 alloy (5.6Al-1.0Ti-6.5Cr-9.0Co-0.6Mo-6.5Ta-6.0W-3.0Re, wt %) according to different sorting methods.

Certain elements can be omitted if considered necessary and so universal schemes can be used based on any two or more elements. Ganesan et al [66, 69] compared different sorting methods. From Figure 3-11, segregation profiles sorted by cobalt single element sort are more scattered than those sorted by Al-W different sort and weighted interval rank sort in CMSX 4 alloy. However, the segregation profiles using Cr-Re different sort in CMSX 4 become more scattered than those using Al-W different sort (Figure 3-12 (b)), but Cr-Re different sort used in CMSX 10 alloy produces less scattered profiles as shown in Figure 3-12 (a). Ganesan et al concluded that weighted interval rank sort (WIRS) produced consistently less scattered segregation profiles for all the investigated elements than the other methods although some different sorts can perform well when choosing a suitable pair of elements to sort data.

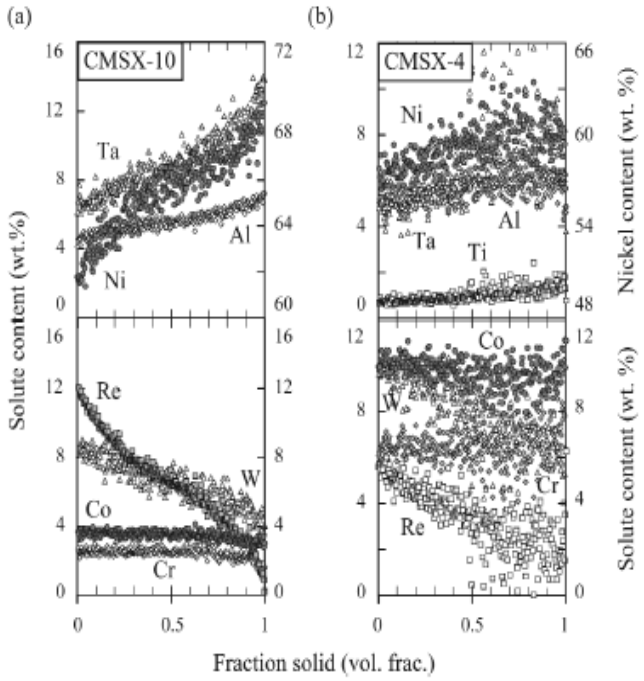

Figure 3-12 Segregation profiles of alloying elements sorted by different sorting method using Cr-Re pair in (a) CMSX-4 alloy (5.6Al-1.0Ti-6.5Cr-9.0Co-0.6Mo-6.5Ta-6.0W-3.0Re, wt %) and (b) CMSX-10 alloy (5.7Al-0.2Ti-2.0Cr-3.0Co-0.4Mo-8.0Ta-5.0W-6.0Re, wt %).

3.2.3.5 Solid fraction assignment

Once the ordered data have been given a rank number i this must be transferred to a solid fraction. In this study, Ganesan et al.'s method to assign solid fraction to each position described below will be followed [66]. Due to the random sampling the true maximum and minimum values may not always be determined and so the fraction solid based on the rank number was given by $f_s(i) = (i - 0.5)/N$, therefore $0 < f_s(i) < 1$. After this, each sampled point was given an estimated solid fraction between 0 and 1.

3.3 Macrosegregation in steels

The cause of macrosegregation is flow of liquid enriched with solute elements driven by shrinkage, gravity, solid deformation or movement of solid dendrites with low solute

concentration in the early stage of solidification over macroscopic distances [70]. They can all change the average composition of relevant volumes away from the bulk composition. Positive and negative macrosegregation respectively refers to the compositions above and below the bulk composition.

3.3.1 Macrosegregation in continuously cast steel slab

Figure 3-13 shows the several types of segregation, included in continuously cast (CC) steel slabs: interdendritic segregation, V segregation, centreline segregation, and white bands [71]. Interdendritic microsegregation is associated with the grain size variation noted above for microalloyed steels. V segregation regions are rich in alloying elements and harmful in terms of hydrogen induced cracking (HIC) [72]. Centreline segregation represents a high degree of positive segregation in the centre region of CC steel slab and is most harmful to the quality of the steel [73]. Figure 3-14 presents a representative carbon concentration profile in a CC steel slab. Centreline segregation can cause an increase in local hardenability in the central area and form lower temperature products, like martensite and bainite in ferritic and pearlitic steels, during cooling. The non-uniform microstructure can result in variable mechanical properties of the final product.

In an ideal continuous casting situation, the top liquid readily feeds the cavity below, due to shrinkage, thus reducing centreline segregation. The centreline segregation can be explained by the ‘mini-ingot’ formation theory, shown schematically in Figure 3-15. Because of the unsteady liquid flow and heat transfer, some columnar zone grains grow quickly up to the centreline and form bridges, thus preventing fresh liquid from above from feeding the shrinkage cavities. This leads to suction of impure interdendritic liquid from the surrounding

mushy zone into the central region thus increasing centreline segregation. Incomplete feeding will generate centreline porosity [73].

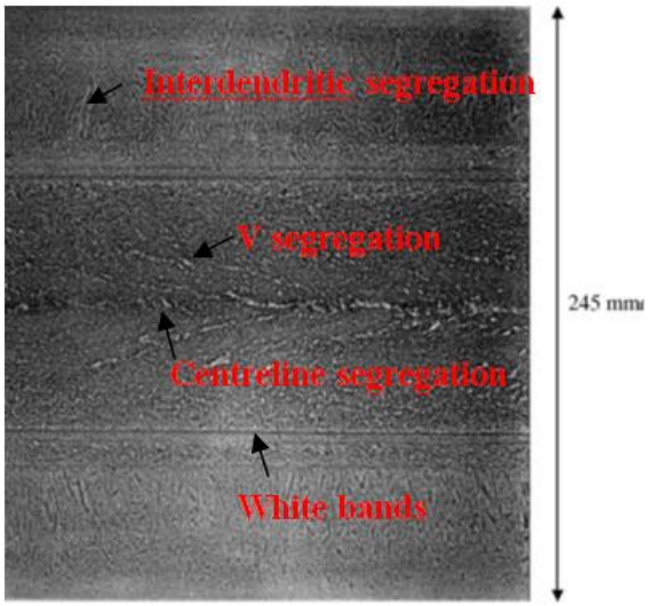

Figure 3-13 Longitudinal section of a continuously cast slab [71].

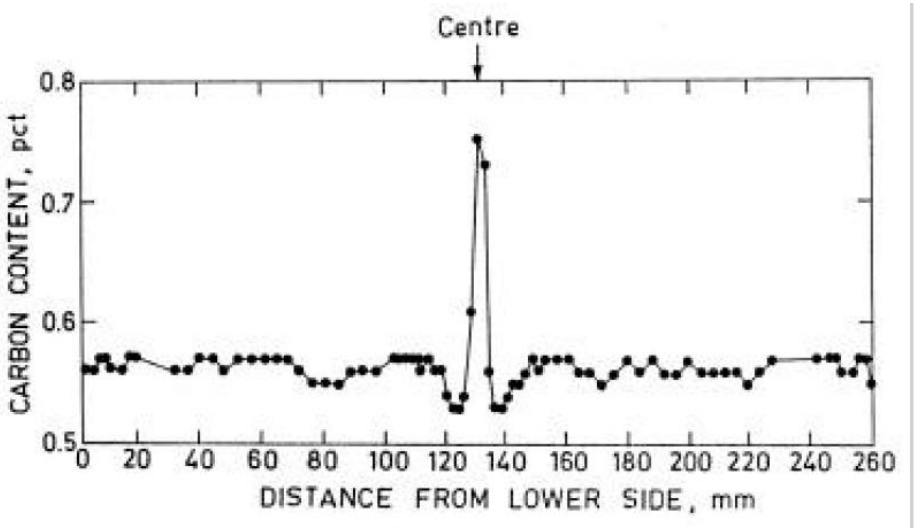

Figure 3-14 A typical carbon concentration profile in CC steel slab [74].

Another interpretation for centreline segregation in CC steel slabs is from large-scale events such as solidification shrinkage and strand deformation which force impure interdendritic liquid from the mushy region into the central region during casting. For example, inadequate roll containment can result in bulging of the already solidified steel shell drawing interdendritic liquid into the centre of the slab, where it freezes. This causes a quite sharp and thin line of positive macrosegregation along the slab centreline, shown in Figure 3-16.

The degree of centreline segregation can be reduced by mechanical or thermal soft reduction of the semi-solidified strand [75]. The principle of mechanical soft reduction is to mechanically decrease the overall thickness of the slab during solidification and cooling [71]. Figure 3-17 illustrates the average value of centreline segregation as the function of soft reduction ratio (expressed with respect to decrease in thickness per unit time along the casting direction) [71]. Thermal soft reduction is applying a high cooling rate close to the end of solidification.

In addition, in-strand or in-mould electromagnetic stirring can be used to reduce the columnar zone size and related interdendritic segregation. The corresponding sizes of columnar and equiaxed zones in the cross section of as-cast steel are influenced by liquid superheating [16, 23]. A small increase in superheat can dramatically affect the percent of columnar and equiaxed zones in continuously cast steel shown in Figure 3-18. Therefore, low superheating in electromagnetic stirring steel can increase the size of the equiaxed zone and reduce the interdendritic segregation together with central-line segregation because of increasing nucleation of equiaxed grains.

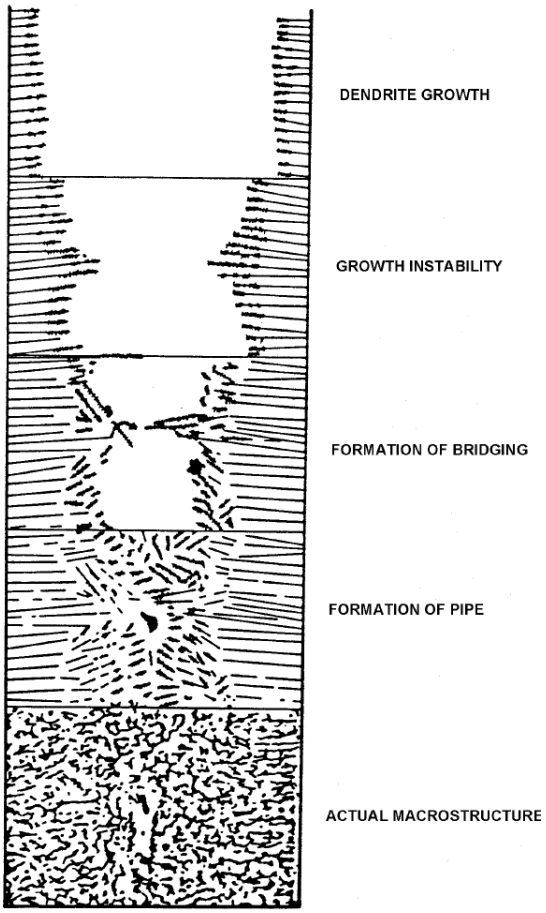

Figure 3-15 Formation of mini-ingot in CC steel [74].

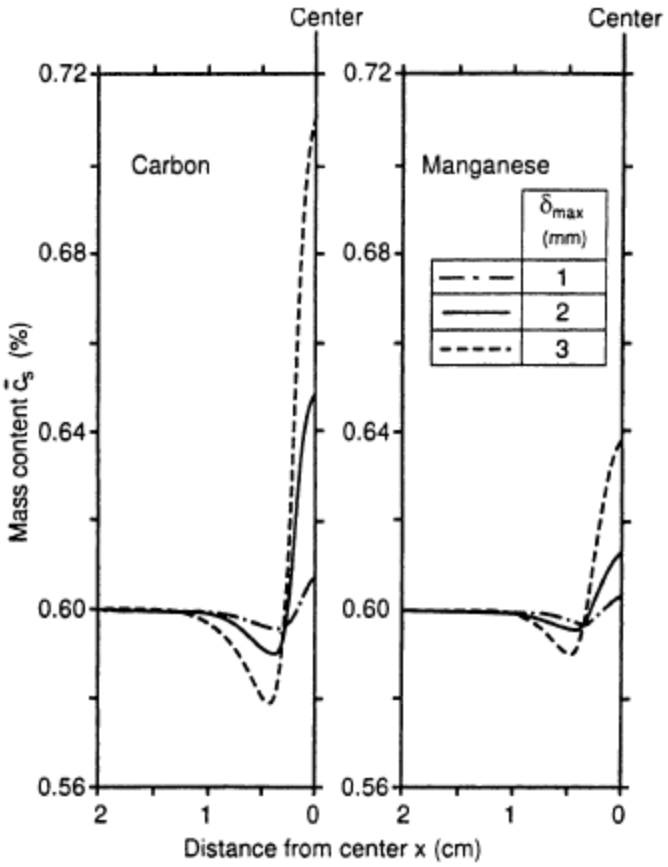

Figure 3-16 Macrosegregaion of carbon and manganese in continuous casting of carbon steel with three different degrees of bulging [76].

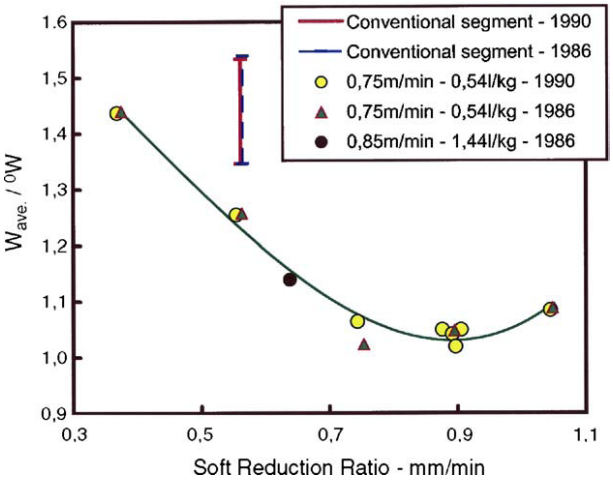

Figure 3-17 The average value of the centreline segregation as a function of the soft reduction ratio [71].

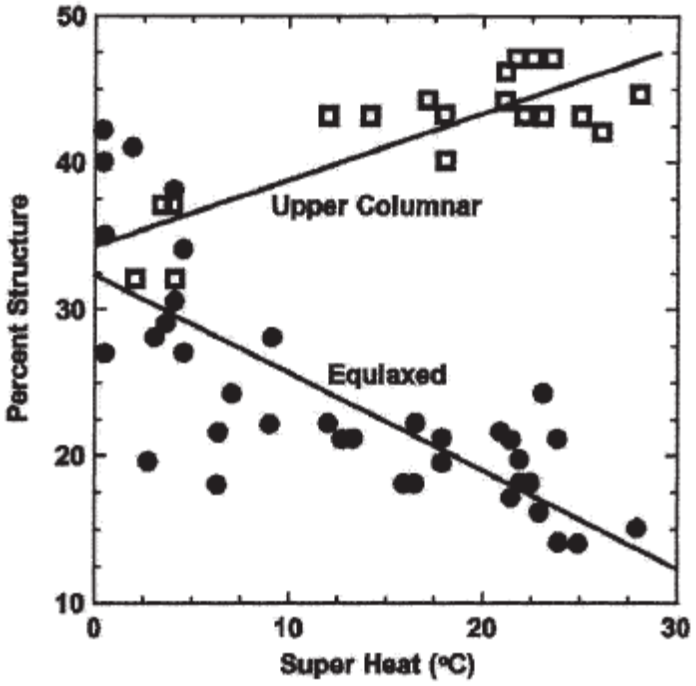

Figure 3-18 Relative amount of columnar and equiaxed zones in continuously cast steel against superheat [22].

3.3.2 Macrosegregation in directionally solidified steels

Solidification rate R and thermal gradient G are the major parameters affecting the directionally solidified microstructure. Thermal gradient is the rate of temperature change with distance in the axial direction. Figure 3-19 shows the 3-D dendrite structure in the quenched mushy zone: the primary dendrite grows along the axial direction from bottom to top, a small deviation in the primary dendrite orientation was found. Near the edge, a few dendrites starting to grow from the wall towards the centre were observed indicating the faster cooling rate near the wall area.

The morphology in the mushy zone is determined by the ratio of G/R in terms of critical values related to the transition between different microstructures. The morphologies related to microstructure of nickel-based super alloy as a function of G and R are shown in Figure 3-20.

If keeping G constant and increasing R, the morphology will change from a planar front through cellular, columnar dendritic to equiaxed dendritic solidification structures. Lee et al. found that for Fe-18Cr stainless steels, dendritic microstructures can be obtained at solidification rates of 50 μm/s or over at G = 10.0 K/mm [77].

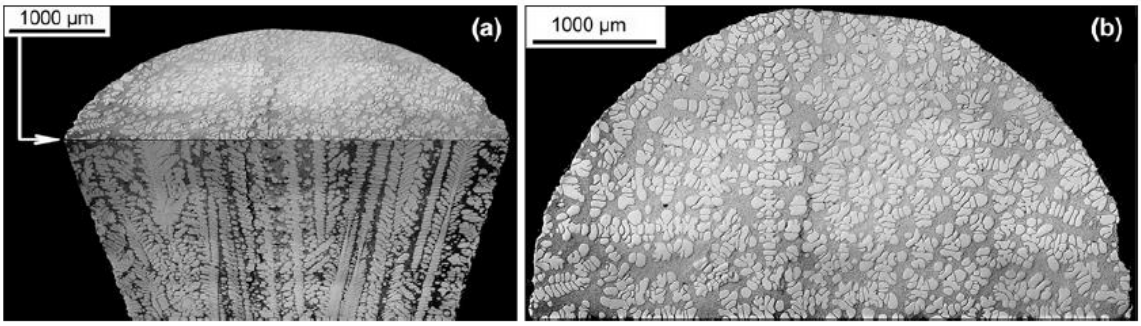

Figure 3-19 Quenched mushy zone of magnesium alloys AZ31 after directional solidification at *GR*= 0.811 K/s: (a) Three-dimensional mushy zone containing both longitudinal and transverse section (b) Transverse section just behind the tips of the dendrites [9].

The temperature gradient associated with the cooling rate is not constant along the axial direction, but is larger at the bottom, constant in the middle and above, which affects the primary arm spacing shown in Figure 3-21. The primary dendrite arm spacing increases with the decreased temperature gradient in the direction of the temperature gradient.

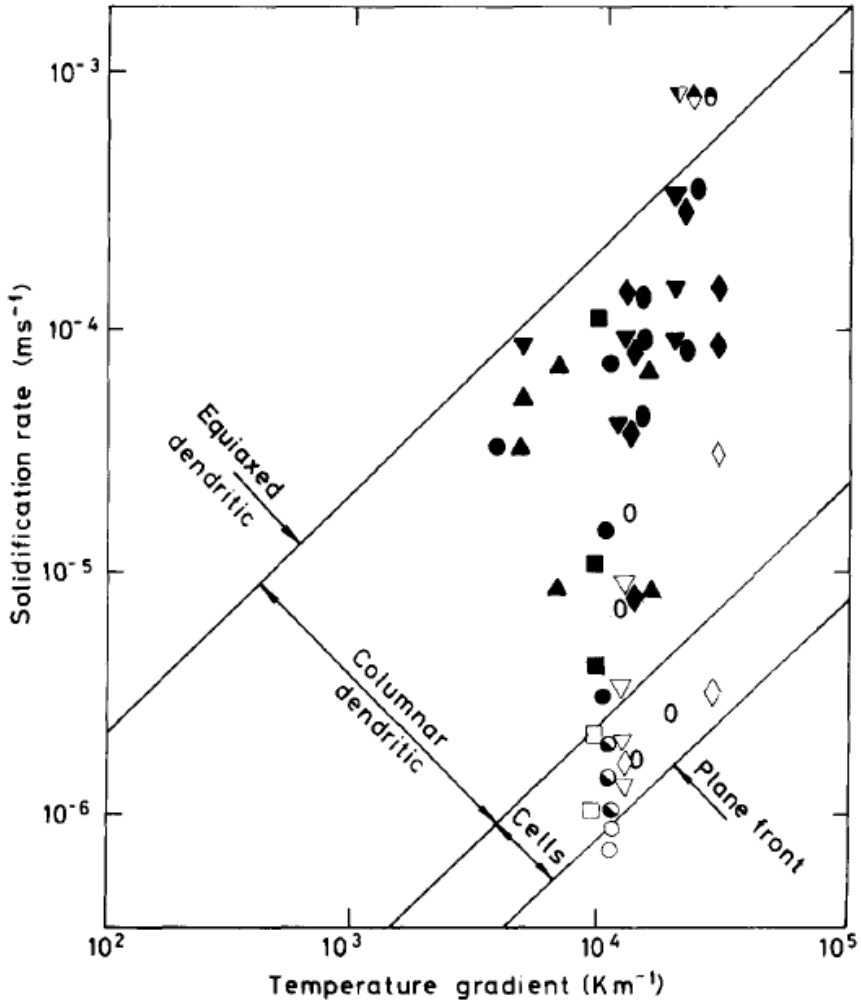

Figure 3-20 Solidification morphologies of Ni-based superalloy by DS displayed on a plot of log R against log G [78].

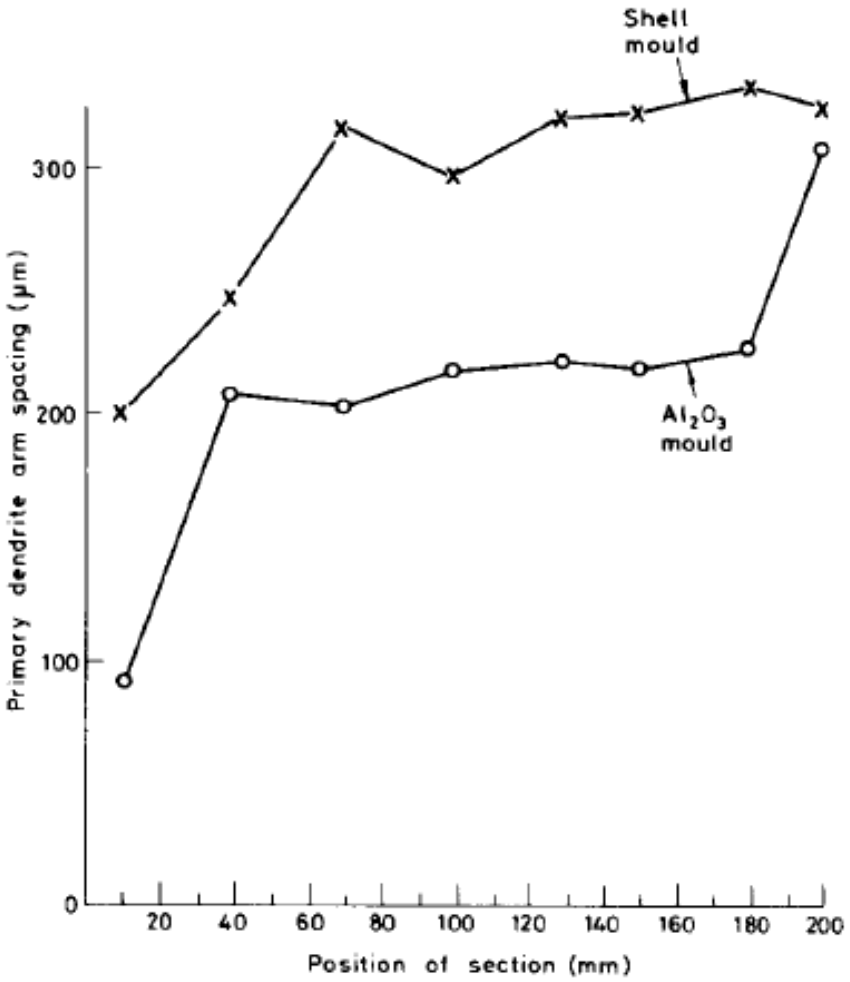

Figure 3-21 Mean primary dendrite arm spacing measured at different positions along the axial direction of directional solidified Ni-based superalloys [78].

Chapter 4 Segregation modelling

4.1 Introduction

Different methods are used to simulate solute redistribution and segregation during phase transformation. Thermo-Calc software is a method to calculate the phase transformations under equilibrium conditions involved with thermodynamic information. Analytical approaches are easy to use to calculate the segregation under different conditions, such as lever rule, Scheil model and Clyne-Kuze model. Thermo-Calc and analytical approaches can be combined to give more accurate segregation results. The numerical methods such as DICTRA are described and show some advantages over analytical approaches.

4.2 Analytical modelling of microsegregation in steels

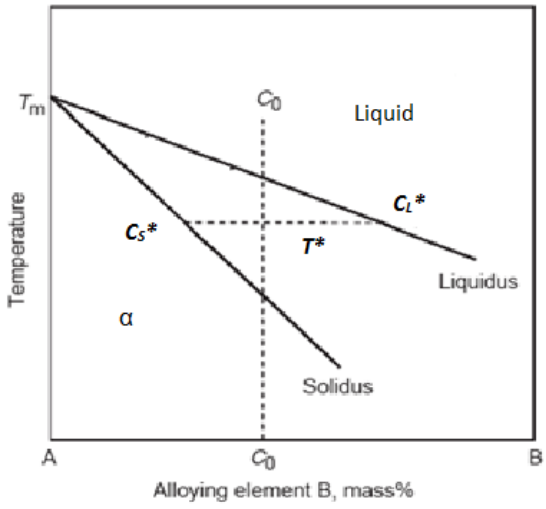

Figure 4-1 Schematic of a partial equilibrium phase diagram.

Microsegregation during steel solidification has been predicted by many models with different assumptions and simplifications. Typically, most microsegregation models consist of an

expression for solute concentration in terms of solid fraction between the neighbouring dendrite arms. There are several common assumptions to all quantitative treatments, which include equilibrium at the liquid-solid interface, no significant undercooling before solid nucleation and constant partition coefficient of solute element. The two basic limiting models are the lever-rule and the Scheil equations [20]. The former is an equilibrium solidification model which assumes complete mixing in the solid and liquid phases. Figure 4-1 shows a partial equilibrium phase diagram of a binary alloy. At temperature T^*, the solid of composition C_S^* and liquid of composition C_L^* are forming in equilibrium at the solid-liquid interface. Assuming complete diffusion in the solid and liquid, the entire solid region has uniform composition $C_S = C_S^*$, and the composition for the entire liquid region is uniform at $C_L = C_L^*$. At temperature T^*, there is a general materials balance as follows:

$$C_S f_S + C_L f_L = C_0 \tag{4-1}$$

where f_S is the solid fraction, f_L is the liquid fraction, and C_0 is the initial liquid concentration.

Since the partition coefficient

$$k = \frac{C_S}{C_L} \tag{4-2}$$

and mass must be conserved

$$f_S + f_L = 1 \tag{4-3}$$

then, the composition of solid as the function of fraction solid is

$$C_S = \frac{kC_0}{1-(1-k)f_S} \tag{4-4}$$

In term of the system temperature, the solid fraction may be written as

$$f_S = \left(\frac{1}{1-k}\right)\left(\frac{T_L - T^*}{T_f - T^*}\right) \tag{4-5}$$

where T_f is the melting temperature of pure material, pure iron for steel, and T_L is the liquidus temperature.

Solid-state diffusion is slow, especially for the larger solute element atoms such as Nb and also solidification is normally a non-equilibrium cooling process, in which the assumption of complete diffusion in liquid and solid is not appropriate. Therefore the lever-rule model is not applicable during solidification [54].

The Scheil equation deals with non-equilibrium conditions, assuming complete mixing in the liquid, no diffusion in the solid and local equilibrium at the solid-liquid interface. In this case, the first solid composition is kC_0 and rejected solute increases the liquid composition above C_0. With the progress of solidification, the newly formed solid would be slightly more enriched in solute than the previously formed solid due to the gradual building up of solute concentration in the liquid. In this circumstance, the last liquid composition can be very high, even up to a eutectoid composition [79].

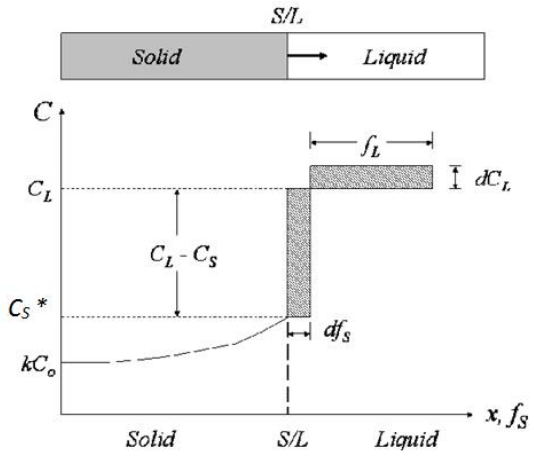

Figure 4-2 Solute redistribution in solidification with no solid diffusion and infinite diffusion in the liquid, at temperature *T**.

The hatched areas in Figure 4-2 respectively represent solute rejected when a small amount of solid forms and the resulting increased solute content in the remaining liquid. Because of mass conservation during solidification, the following quantitative expression can be obtained:

$$(C_L - C_S^*)df_S = (1 - f_S)dC_L \quad 4\text{-}6$$

Substituting the equilibrium partition coefficient; using the boundary condition $C_S^*=kC_0$ at $f_S=0$; the integration can be performed below:

$$\int_0^{f_S} (\frac{1}{k} - 1)C_S^* \, df_s = \int_{kC_0}^{C_S^*} (1 - f_S) \, d\frac{C_S^*}{k} \quad 4\text{-}7$$

Integrating results in prediction of composition of the solid during solidification:

$$C_S^* = kC_0(1 - f_S)^{(k-1)} \quad 4\text{-}8$$

Or, expressing the fraction of solid as a function of temperature

$$f_S = 1 - \left(\frac{T_L - T}{T_f - T}\right)^{1/(k-1)} \quad 4\text{-}9$$

However, the Scheil equation inadequately estimates the final solute composition concentration, as the Scheil equation generates an infinite value of C_S^* at $f_s=1$. This model is only used for very rapid solidification process such as laser welding with cooling rates over 10^2 ℃/s [80]. In many cases at lower cooling rates, the experimental segregation profiles differ considerably from Scheil predicted results [57, 58, 63, 81]. One example is in Al-Cu-Mg alloys at cooling rate of 0.78 K/s by Xie et al. as shown in Figure 4-3.

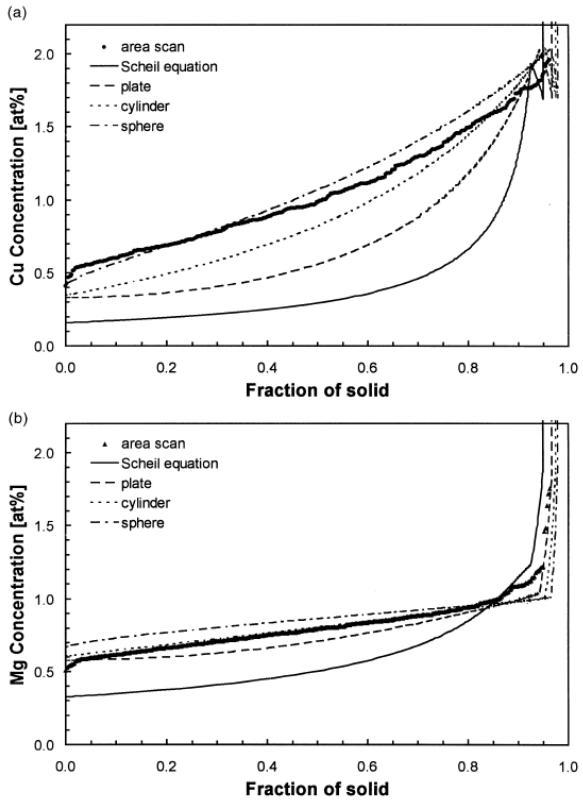

Figure 4-3 Measured concentration profiles by area scan method and predicted concentration profiles containing the Scheil equation of (a) Cu and (b) Mn in Al-3.9Cu-0.9Mn alloy at cooling rate of 0.78 K/s as a function of fraction of solid.

In order to predict microsegregation during solidification accurately, the finite solute atom diffusion in the solid must be considered. Brody and Flemings [82] have proposed a model that assumes finite back-diffusion in the solid and infinite diffusion in the liquid, based on one-dimensional solute redistribution, as follows :

$$C_S^* = kC_0[1 + f_S(\beta k - 1)]^{(1-k)/(\beta k-1)} \quad 4\text{-}10$$

$$f_S = \left(\frac{1}{1-\beta k}\right)\left[1 - \left(\frac{T_f - T}{T_f - T_L}\right)^{(1-\beta k)/(k-1)}\right] \quad 4\text{-}11$$

$$\beta = 2\alpha = \frac{2D_S t_f}{X^2} \quad 4\text{-}12$$

Where β is generally introduced as a back-diffusion parameter; α is a Fourier number. D_S is the diffusion coefficient of the solute element in the solid phase, t_f is the local solidification time, and X is the length scale of the microsegregation, usually regarded as equal to half of the secondary dendrite arm spacing, λ_{SDAS}.

The Brody and Flemings model simplifies into the Scheil model when $D_S \rightarrow 0$ and α =0. Also if elemental diffusion is infinitely fast in the solid phase, the model should change to the lever rule (Equation 4-4 and 4-5), corresponding to β=1 (α =0.5). When β is more than 1, the model is physically unavailable, since mass conversation cannot be satisfied.

Clyne and Kurz [83, 84] modified β to make sure the model is physical reasonable ($0 \leq \beta \leq 1$).

$$\beta = 2\alpha\left(1 - exp\left(-\frac{1}{\alpha}\right)\right) - \frac{1}{2}exp\left(-\frac{1}{2\alpha}\right) \quad 4\text{-}13$$

In this model, all the physical properties, such as partition coefficients and diffusion coefficients, are assumed to be constant. Also, as β and k correspond to one solute element, in Equation 4-5, 4-9 and 4-11, temperature (T) as function of solid fraction (f_S) can only be calculated based on one solute element.

The analytical models were extended to take account of multicomponent alloying in low carbon steels [54, 85]. The cross-element effect was neglected. The liquidus temperature (T_L) can be calculated according to the composition as shown below:

$$T_L = T_f - \sum_i m_i \cdot C_{0,i} \quad 4\text{-}14$$

Where m_i is the liquidus line slope of each component i in the binary Fe phase diagram. The interface temperature (T_{int}) as a function of the interface composition in liquid ($C_{L,i}$) was obtained by modifying Equation 4-14:

$$T_{int} = T_f - \sum_i m_i \cdot C_{L,i} \qquad 4\text{-}15$$

The equations mentioned above are all semiempirical results, but they can be very useful in predicting the microsegregation if applied carefully. The Clyne-Kurz model has been used to predict segregation during solidification [85-89]. In Fe-C-P alloys, the carbon and phosphorus concentrations in liquid as a function of solid fraction at 4.6 and 10 K/s cooling rates calculated by the Clyne-Kurz model showed good agreement with phase-field calculation, Figure 4-4 [88]. The α values used in Clyne-Kurz model are 0.487 for carbon and 0.15 for phosphorous. Won et al. applied the Clyne-Kurz model considering the multicomponent effects to calculate the characteristic temperature such as zero strength temperature (ZST) and zero ductility temperature (ZDT) in steels with a range of carbon contents from 0 - 0.8 wt % and cooling rate up to 20 K/s during solidification [85]. Figure 4-5 shows the predicted ZST and ZDT corresponding to solid fraction of 0.75 and 0.99 respectively were in reasonable agreement with experimental data. However, Khalifa et al. showed that the solidification paths based on the segregation of Fe and Si in Al-Si-Fe alloys at slow (~ 0.2 °C/s) and rapid (~15 °C/s) cooling rates calculated by analytical equations (Scheil model, Brody and Flemings and Clyne and Kurz) did not agree with the actual solidification paths [90]. The interaction between Fe and Si and more effective diffusion may explain the departure from analytical approaches.

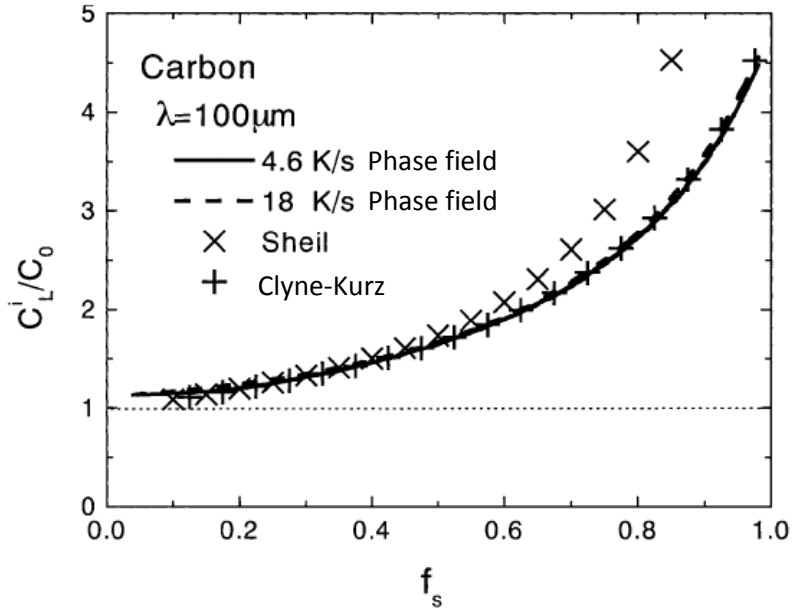

(a)

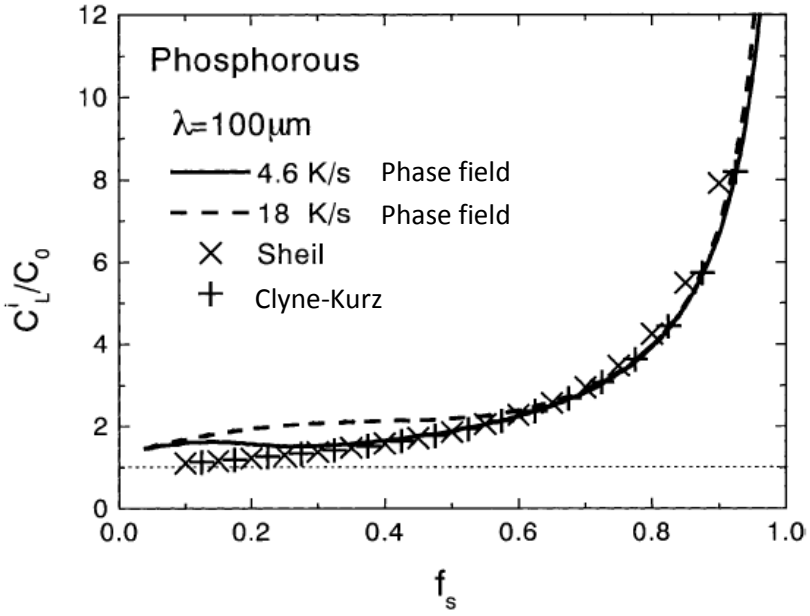

(b)

Figure 4-4 Normalised (a) carbon and (b) phosphorous concentration in liquid as a function of solid fraction [88].

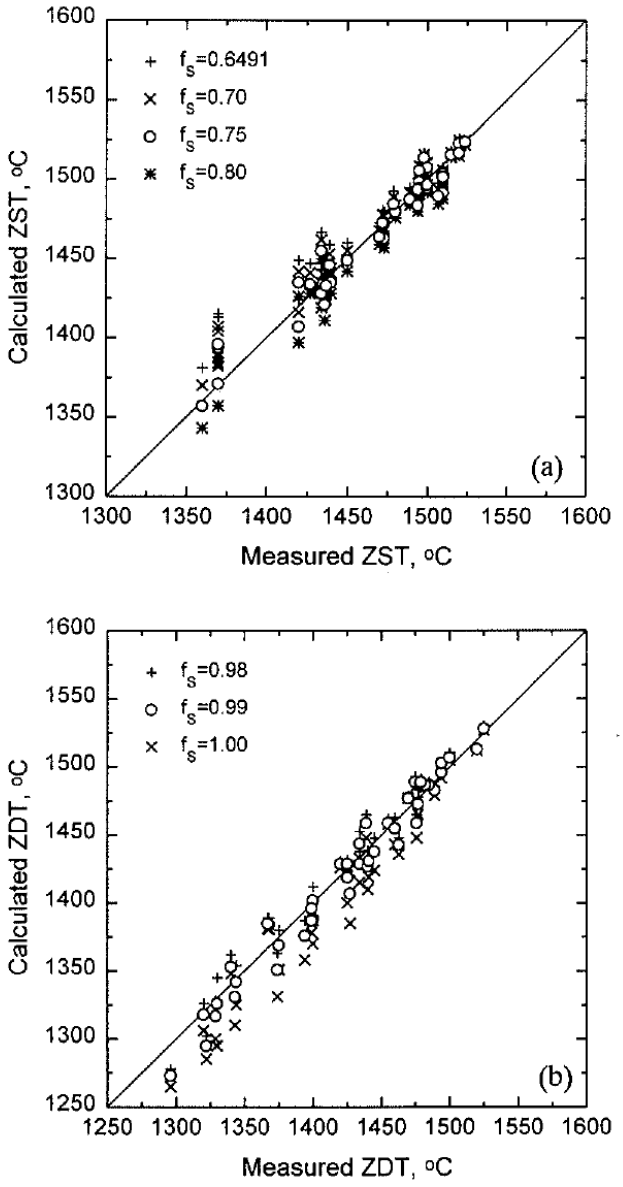

Figure 4-5 Clyne-Kurz predicted and experimental measured ZST (a) and (b) ZDT values [85].

There are very few publications about the accuracy of Clyne-Kurz model for predicting substitutional alloying element segregation in steels. This study used Scheil and Clyne-Kurz models taking into account multicomponent effects to predict microsegregation of substitutional alloying elements during solidification.

4.3 Thermo-Calc

Thermo-Calc [91, 92] is a commercial software package widely used for thermodynamic and phase diagram calculations of multi-component systems for many types of materials. It can effectively process multi-component systems defined with up to 40 elements and many different phases. Because thermodynamics describes the equilibrium state of a system, then Thermo-Calc mainly provides results predicted under equilibrium conditions.

Calculations are based on thermodynamic databases made by evaluation of experimental data using the CALPHAD [93] (calculation of phase diagrams) method. Gibbs energy is expressed as a function of temperature, composition and pressure for each phase. The equilibrium can be calculated by energy minimisation procedure under given conditions. The Thermo-Calc can use different models to deal with the non-ideality of a phase, such as compound energy model. The model parameters used in the free energy expression are evaluated and optimised by comparing with experimental data (such as phase diagram lines, heat capacities) to form the thermodynamic database. Figure 4-6 shows the generalised CALPHAD assessment process. Databases are available for steels, Ti-, Al-, Mg-, Ni-alloys, multi-component oxides and a large number of other materials [94].

Thermo-Calc is a free energy minimisation routine based on sub-regular models for solutions. The general structure of the Thermo-Calc package is shown in Figure 4-7. These modules are commonly necessary for thermodynamic calculation and are linked to each other. For example, POLY module is the polynomial fitting sub-routine that achieves the energy minimisation for a given set of conditions and is often regarded as a sub-module of the POST module which is designed for post-processing of various phase and property diagrams. Many

kinds of results can be present after post-processing, such as a single equilibrium state or map phase diagrams.

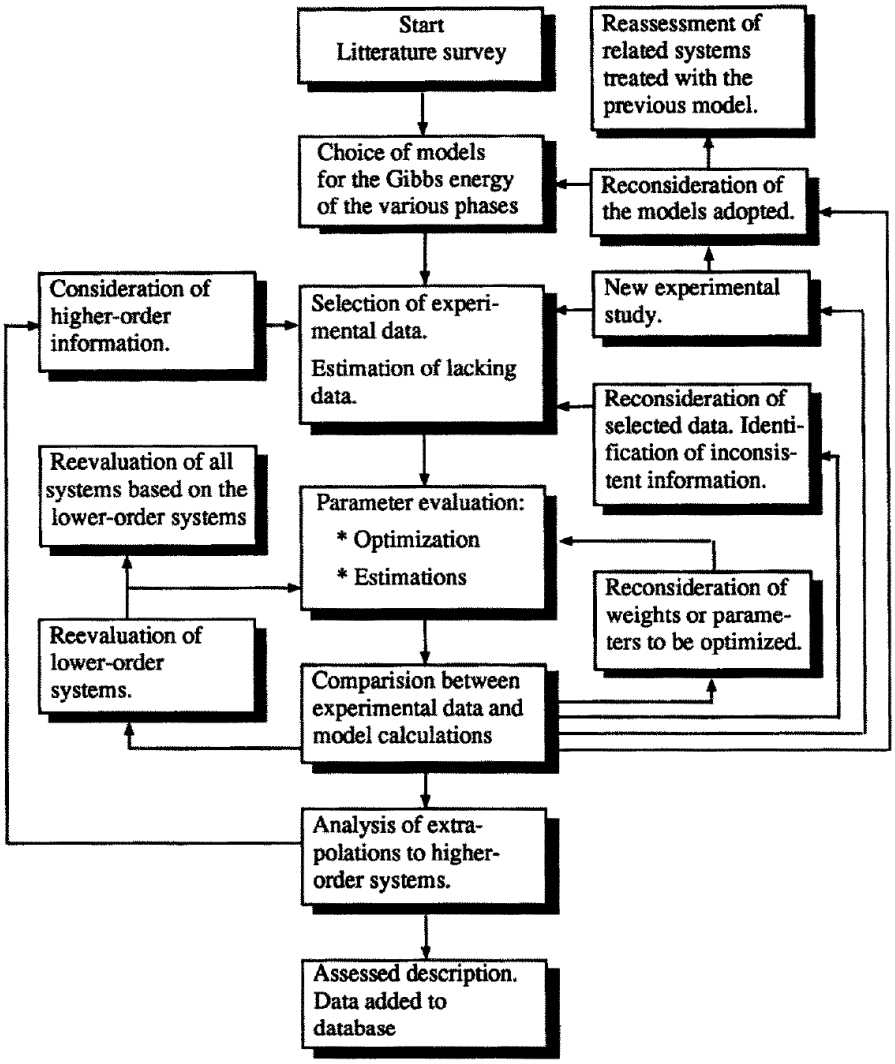

Figure 4-6 Flow chart showing the process of the generalised CALPHAD assessment.

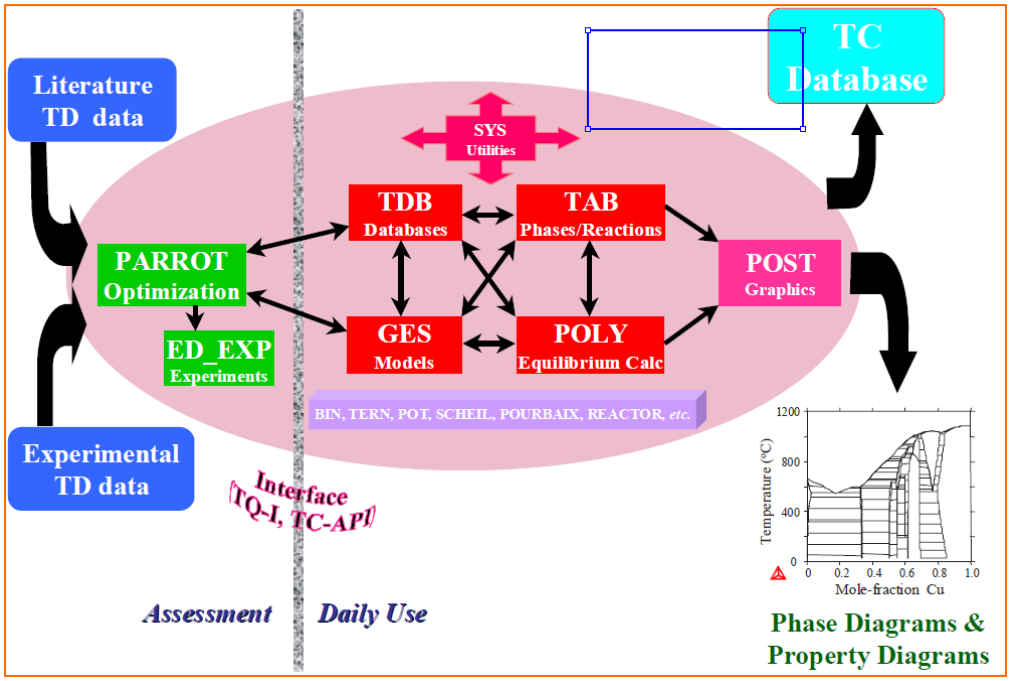

Figure 4-7 General structure of the Thermo-Calc package [94].

Thermo-Calc has been widely used as a powerful tool to develop new materials and processes in industry. The comparison between Thermo-Calc calculation and experimental data for different materials were investigated by various researchers [95-99]. Figure 4-8 shows the calculated Sb-Sn phase diagram together with experimental data. Hakan et.al. [99] reported that the critical temperatures for phase transformations in a low alloy steel predicted by Thermo-Calc are in good agreement with experimental results from differential thermal analysis (DTA).

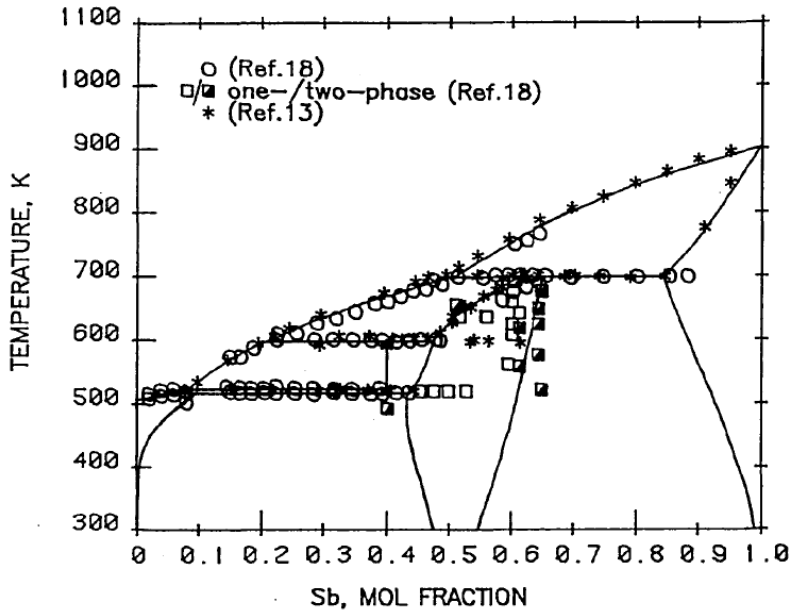

Figure 4-8 Comparison between calculated Sb-Sn phase diagram and experimental data (circles, stars and squares) [96].

4.4 Numerical modelling of segregation

4.4.1 Phase field modelling

Phase field models (PFM) have been used to simulate the microstructure evolution together with segregation during solidification. The method has been developed for one component systems [100, 101], binary alloys [102, 103], and multicomponent alloys [88, 104-106] in dual phase and multiphase systems. The diffuse interface with a certain thickness used in PFM has continuous variation in properties by applying phase field variables which are continuous functions in space and time. Figure 4-9 shows how the phase field variable η separates the different phases in the phase field model: $0 \leq \eta \leq 1$ corresponding to the interface.

It can be applied not only for quantitative simulation in 1D but also to phase transformations in 2D and 3D as explicit tracking of the interfaces is not necessary. Two kinds of phase-field

model exist. One uses the order parameter which is a physical parameter and can be introduced into thermodynamic databases. The second one uses a well-defined physical order parameter for phase transformations. The microstructure evolution is assumed to be determined by the phase-field equation in both types. Microsegregation in Fe-C-P ternary alloys has been investigated using a phase-field model by Alexandre [107]. The phase-field model has been built as a computational tool (such as Micress software) which can access Thermo-Calc thermodynamic and kinetic databases and model the microstructure. However, considering the accuracy of PFM, the grid size should be small (less than 1 micron) which leads to long simulation times for multicomponent alloys and low cooling rates during casting.

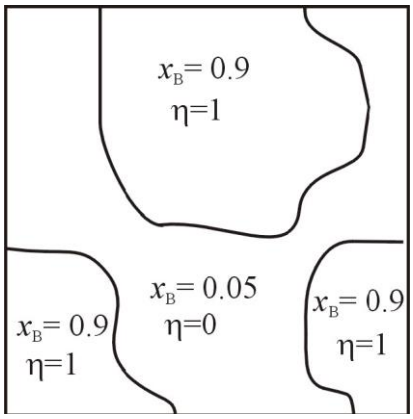

Figure 4-9 In binary alloy A-B, phase α: η=0; phase β: η=1.

4.4.2 Finite-difference modelling

A finite-difference model was developed by Matsumiya et al. [51] to simulate the interdendritic microsegregation between primary columnar cells with an hexagonal cross-section. It takes into consideration solute diffusion in both solid and liquid phases during solidification with one dimension perpendicular to the axial direction. Equilibrium was assumed at the interface of solid and liquid. The liquidus temperature, calculated according to the composition in the liquid phase at the solid/liquid interface, was equal to the actual

temperature all the time and was assumed constant throughout the whole cross-section of columnar cells. T_L was calculated by the equation as follows.

$$T_L = T_f - \sum_i m_i C_L^{i*} \qquad 4\text{-}16$$

Where T_f is the melting point of pure iron, 1536 ℃; m_i is the liquidus line slope of each component in the peseudobinary Fe- phase diagram.

The area was divided into certain elements shown in Figure 4-10. The interface is restricted to the nodal boundaries and was determined explicitly only when it move from one nodal boundary into the adjacent nodal boundary.

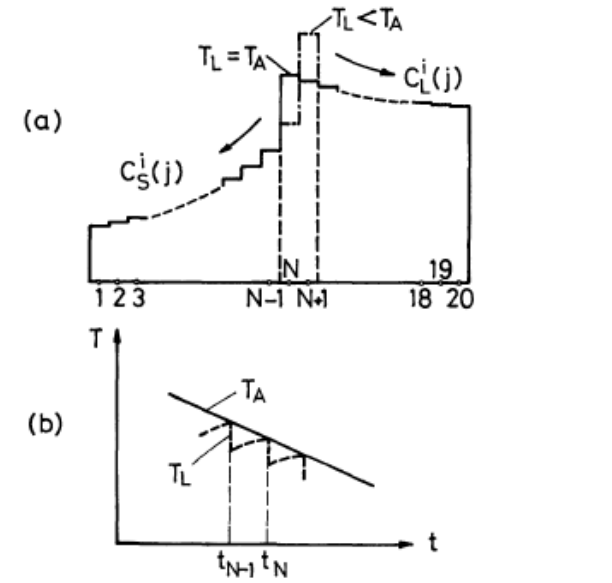

(a) ——: When $(N-1)$-th element completes its solidification
——: When N-th element solidifies subsequently
(b) ——: Actual temperature given
----: Liquidues temperature calculated from the solute contents in the liquid at the solid–liquid interface.

Figure 4-10 Solute distribution on the nodal points (a) and temperature change with the passage of time (b).

Ueshima et al. [108, 109] extended the above method to analyse phase transformations and microsegregation of a steel solidified through the peritectic transformation between primary columnar cells.

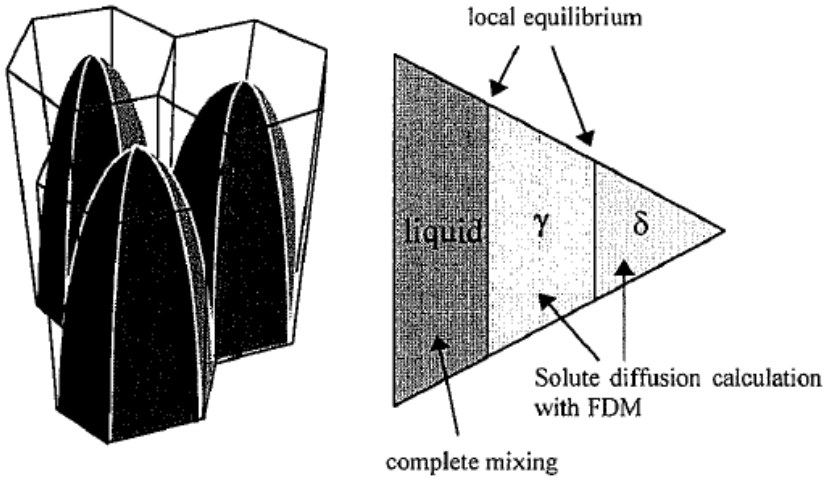

a) b)

Figure 4-11 Schematic diagram showing the cellular array and b) cross-section presumed in the FDM.

The cross section of the columnar grain is assumed to be a regular hexagon and one sixth of which is shown in Figure 4-11. Complete mixing in the liquid was assumed. When the liquidus temperature T_L or peritectic temperature T_{Ar4} was equal to the actual temperature, that element was taken to have completed the solidification or δ/γ transformation and the interface moved to the next element. T_L and T_{Ar4} are calculated from the Equation 4-16 and 4-17 respectively.

$$T_{Ar4} = 1392 + 1122(wt\%C) - 60(wt\%Si) + 12(wt\%Mn) - 140(wt\%P) - 160(wt\%S) \quad 4\text{-}17$$

The agreement for calculated and experimental phosphorus and Mn profiles is good before the occurrence of the peritectic reaction at a cooling rate of 2.7 K/s and not good during the peritectic reaction at this cooling rate or for the whole solidification at a cooling rate of 27 K/s.

One concern is the solute gradient is not taken strictly at the interfaces, so the accuracy of this method may be doubtful in the area where the solute gradient changing is rapid.

A numerical model which used Crank's lagrangian interpolation technique [110] and allowed the position of the interface to be freely located between two nodal points and also took the coarsening of secondary dendrite arms into consideration was proposed by Howe et al. [111].

The mass conservation equation is shown blow

$$C_1(1-k)\frac{dX}{dt} = D(\frac{\partial C}{\partial x})_X + \left(\frac{dC_1}{dt}\right)\left(\frac{\lambda}{2} - X\right) + \frac{1}{2}(C_1 - C_0)\frac{d\lambda}{dt} \qquad 4\text{-}18$$

Where, C_l is composition in liquid, X is the position of interface, C_0 is the bulk composition in the computing cell, x is the direction of growth perpendicular to the interface plane. λ/2 is the size of the cell. The last part on the right hand side represents the solute build-up due to growth of the liquid region for coarsening effect. The diffusion coefficient *D* and partition coefficient *k* was based on the binary system and the cross-effect between different elements was neglected.

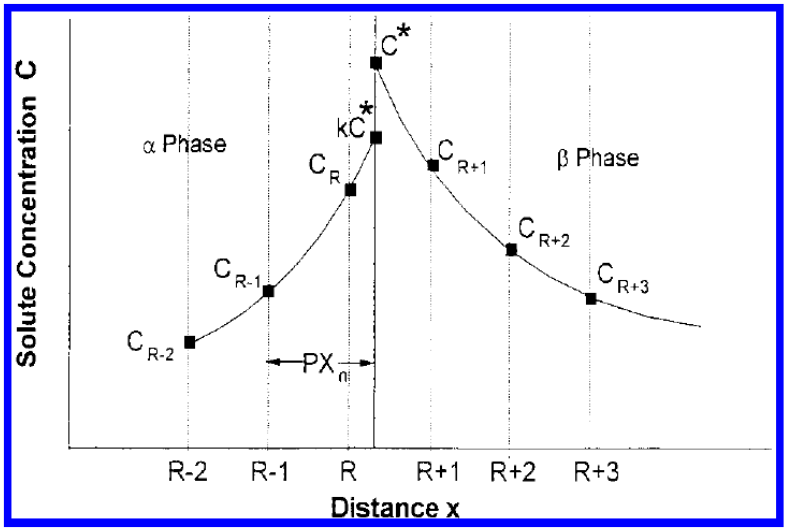

Figure 4-12 Schematic diagram showing the solute concentration C on the nodal points in α, β phases and α/β at time$(t + \delta t)$.

Referring to Figure 4-12, the Crank scheme used to calculate the solute gradients in each phase at the interface is shown below

$$\left(\frac{\partial C}{\partial x}\right)_{\alpha}^{*} = \frac{1}{X_n}\left(\frac{P}{1+P}C_{R-2} - \frac{P}{1+P}C_{R-1} + \frac{1+2P}{P(1+P)}C^{*}\right)$$
$$\left(\frac{\partial C}{\partial x}\right)_{\beta}^{*} = \frac{1}{X_n}\left(-\frac{3-P}{4-P}C_{R+3} + \frac{4-P}{3-P}C_{R+2} - \frac{7-2P}{(3-P)(4-P)}kC^{*}\right) \quad 4\text{-}19$$

This method is basically explicit, although the compositions at the interface C* and P related to the position of interface were determined in an implicit manner. Besides, in this model, the composition of rapid diffusing solute elements in each phase was assumed to be uniform to save computing time. Planar, cylindrical, or spherical geometries can be calculated using this method. Also, the temperature dependent diffusion coefficient and partition coefficient can be taken into consideration.

4.4.3 DICTRA

DICTRA software is used for simulating diffusion controlled phase transformations in multi-component alloy systems, according to a numerical solution of the multi-component diffusion equations. In order to execute a DICTRA simulation, both a thermodynamic and a kinetic database are required. The thermodynamic databases used in multicomponent systems are the same as those in Thermo-Calc [91], extrapolated using the CALPHAD method by assessing experimental data collected and chosen from literature. The calculation of phase diagrams (CALPHAD) method [93] in which the Gibbs energy has a relation with temperature and composition, has been proved to be a very powerful tool in industrial design of new materials and processes. A free-energy minimisation is used to determine the phase equilibria. Similarly, the atomic mobility of each species as a function of temperature and composition was chosen to form the kinetic database called the mobility database created through an assessment

procedure similar to the one used for thermodynamic databases. Combined thermodynamic and mobility databases are implemented in DICTRA [112] to model diffusion controlled phase transformations. DICTRA simulations are one-dimensional and available for three different geometries (planar, cylindrical and spherical). Up to 10 components may be simulated at the same time, due to the available necessary kinetic and thermodynamic data.

Many researchers have used it to simulate the phase transformation and segregation in steels [113-118]. Lippard et al. [116] predicted the Cr and Mo concentration profiles in as-cast AerMet100 steel (Fe-9Cr-1Mo-0.2C) ingots during solidification and homogenisation processes by DICTRA. The prediction during solidification agrees well with the experimental composition analysis, Figure 4-13 and the homogenisation process had a little faster diffusion rate than the prediction due to the uncertainty of Mo mobility in iron. In a concentrically solidified specimen of a Fe-4.2Ni peritectic alloy which was used to simulate experimentally the centreline segregation in continuous casting, Ni concentration profile predicted by DICTRA compared quite well with experimental profiles at a cooling rate of 5 K/s as shown in Figure 4-14 [115]. The ferrite growth in austenite in boron-bearing low-alloy steel was also predicted by DICTRA and had satisfactory agreement with experimental results, Figure 4-15.

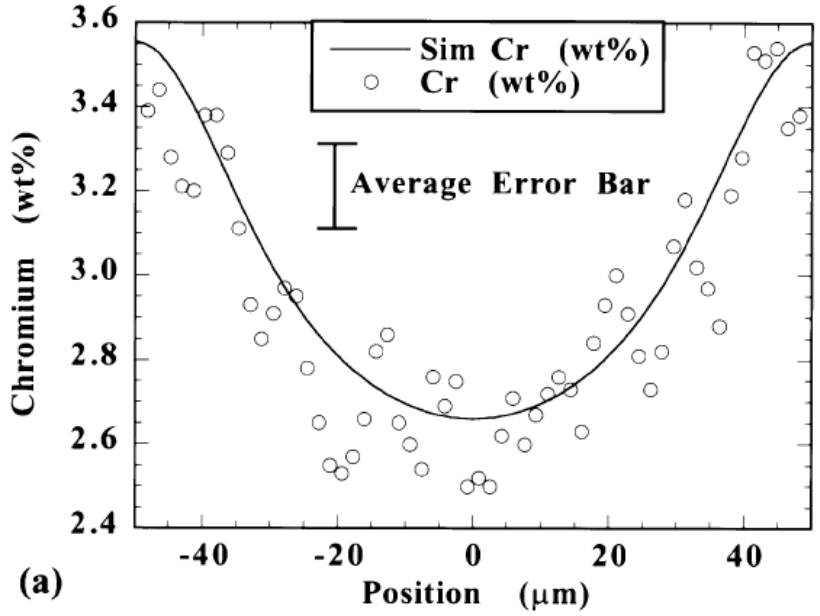

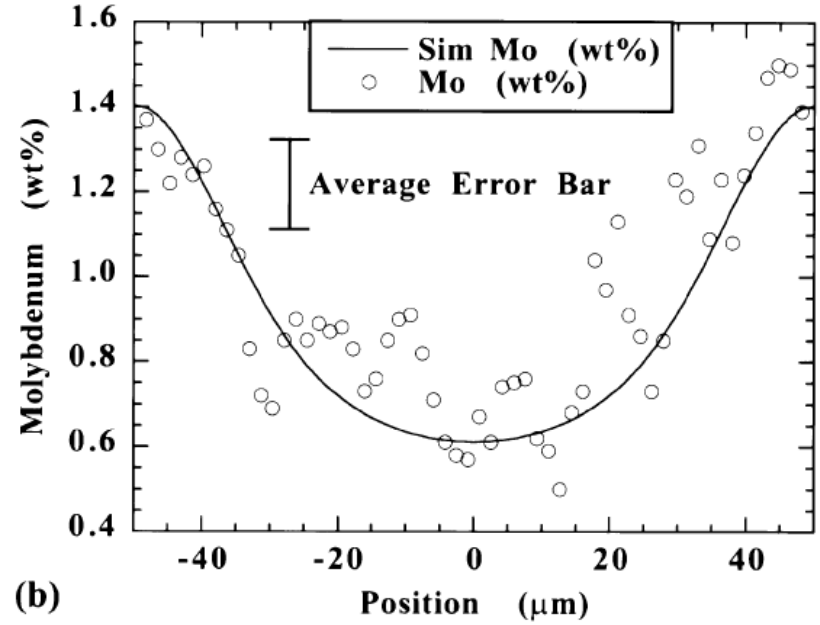

Figure 4-13 Experimental and DICTRA predicted segregation profiles of (a) Mn and (b) Mo in as cast steel (Fe-9Cr-1Mo-0.2C) across a 100 μm length of second dendrite arm.

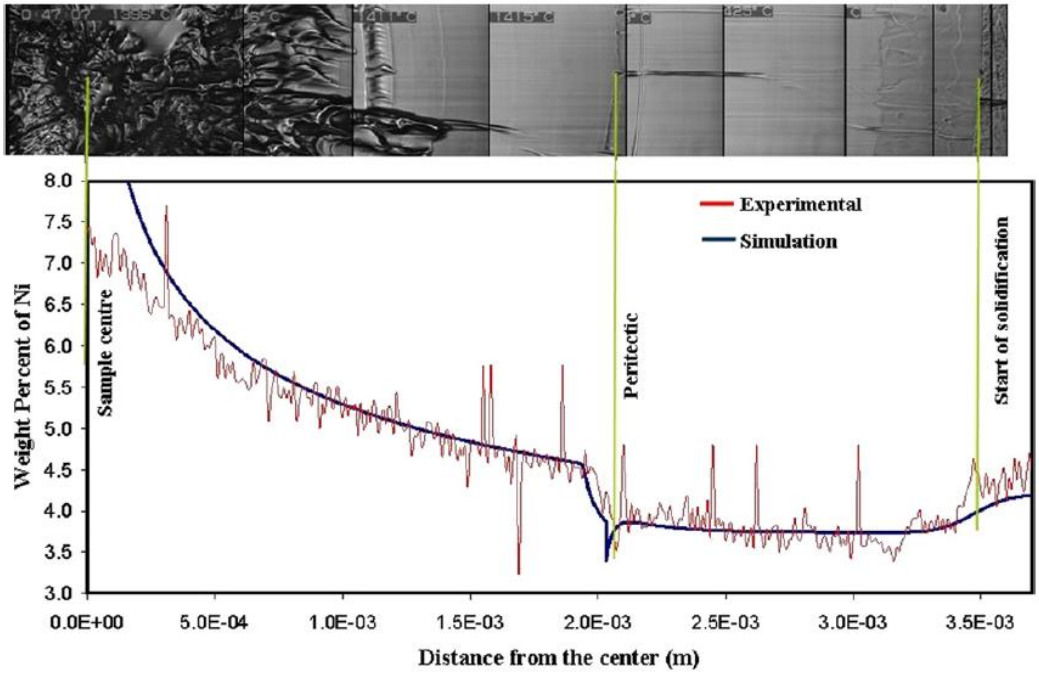

Figure 4-14 The phase transformation sequence which occurred during solidification of Fe-4.2 wt % using concentric solidification technique at a low cooling rate of 5 K/s with corresponding Ni profiles determined experimentally and by simulation.

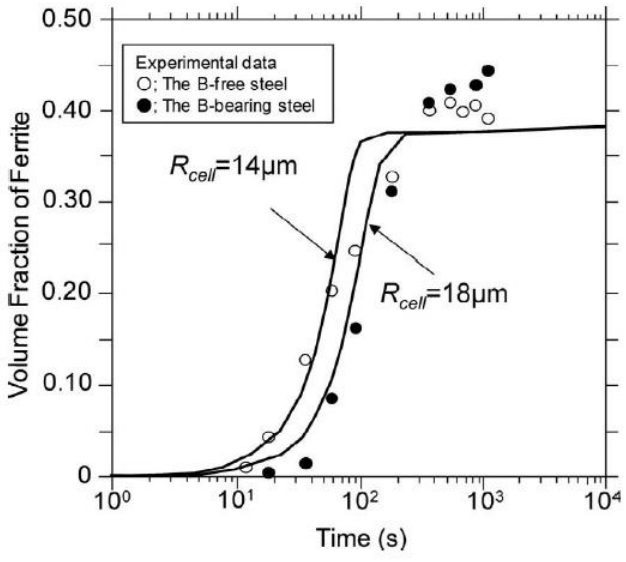

Figure 4-15 Volume fraction of ferrite as a function of time from experimental data and predicted by DICTRA in B-free steel and B-bearing steel corresponding to diffusion cell size R_{cell}=14 and 18 μm respectively.

4.4.3.1 Theory of DICTRA

In the presence of a concentration gradient of species k, the flux of corresponding species is expressed by Fick's first law which is shown below for a single phase, binary alloy system and isothermal conditions

$$J_k = -D_k \frac{\partial c_k}{\partial z} \tag{4-20}$$

Where, J_k (kg/s·m^2) is the interdiffusion mass flux of species k, which is the amount of k transferred by diffusion per unit time and per unit area perpendicular to the diffusion direction z. D_k is mass diffusivity or interdiffusion coefficient mainly depending on the temperature and concentration. C_k is the concentration of species *k*.

When Fick's law is combined with the continuity equation,

$$\frac{\partial c_k}{\partial t} = \frac{\partial}{\partial z}(-J_k) \tag{4-21}$$

the fundamental differential equation of diffusion is obtained:

$$\frac{\partial c_k}{\partial t} = \frac{\partial}{\partial z}(D_k \frac{\partial c_k}{\partial z}) \tag{4-22}$$

generally called Fick's second law.

In practice, more than 2 species are contained in the majority of alloys. As shown in Figure 4-16, in a binary Ni-Al system, with increasing concentration of Al and temperature, diffusivity of Al increased. Microsegregation in alloys can affect the diffusivity of that element: the higher concentration positions of one element can speed up the diffusion of this element to lower concentration areas so that the predicted segregation of that element can be decreased more than that using composition independent diffusion coefficients.

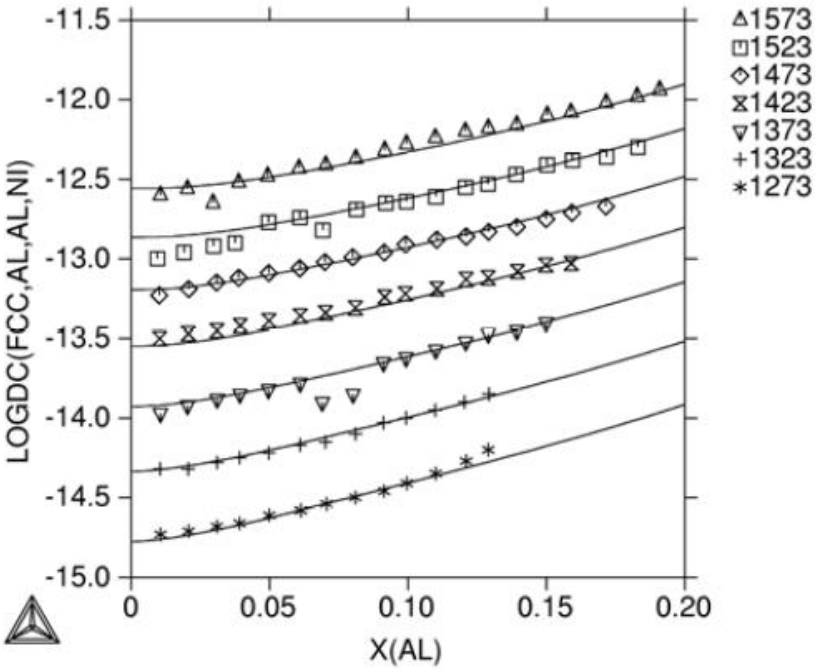

Figure 4-16 Logarithm of the mass diffusivity ($\widetilde{D}$) in the FCC-phase of a binary Ni-Al system versus the concentration of species Al, X(Al), at different temperatures (K). DICTRA predictions are shown as lines and experimental data are shown as symbols [119].

On the other hand, one element's concentration gradient may lead to diffusion of another element. Figure 4-17 shows the up-hill diffusion [120] of carbon achieved by welding two Fe-Si-C steels with similar carbon content and different Si contents together. There is discontinuity in carbon content at the jointline of these two steels. The higher Si content in the left hand side of the profile increases the activity of carbon so that the silicon concentration gradient causes movement of carbon atoms to the right.

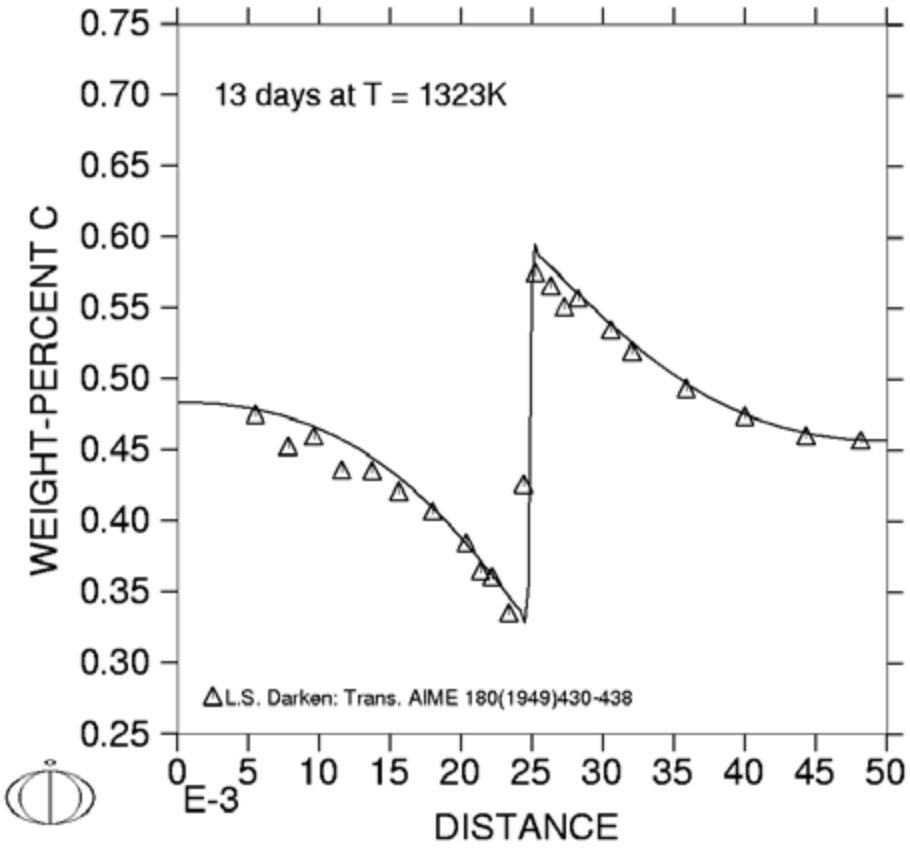

Figure 4-17 Carbon concentration profile in a joint between two Fe-Si-C steels with similar C contents and different Si contents.

The multicomponent equation extended from Fick's first law was first proposed by Onsager [121]. It is assumed that each thermodynamic flux was linked to every thermodynamic force, so that:

$$J_k = -\sum_{i=1}^{n} L'_{ki} \frac{\partial \mu_i}{\partial z} \qquad 4\text{-}23$$

The parameter μ_i is the chemical potential for species i and is postulated to have a unique relationship with composition, i.e., $\mu_i = f(c_1, c_2, c_3 \ldots c_n)$. L_{ki}' is a proportional factor depending on the mobility of a species. This can also be rewritten to express it as a function of

concentration gradient rather than chemical potential gradient by introducing unreduced diffusivities, D_{kj}.

$$J_k = -\sum_{j=1}^{n} D_{kj} \frac{\partial c_j}{\partial z} \quad 4\text{-}24$$

and the D_{kj} can be identified as

$$D_{kj} = -\sum_{i=1}^{n} L'_{ki} \frac{\partial \mu_i}{\partial c_j} \quad 4\text{-}25$$

The $\partial\mu_i/\partial c_j$ is a purely thermodynamic property, so the flux of species k can be divided into two parts, one thermodynamic and one kinetic.

With reference to a volume-fixed frame, only substitutional species contribute to the volume. One concentration gradient can cancel one of the others. When choosing n as a solvent element, the modified Equation 4-24 can be expressed as

$$J_k = -\sum_{j=1}^{n-1} D_{kj}^{n} \frac{\partial c_j}{\partial z}$$

$$D_{kj}^{n} = D_{kj} - D_{kn} \text{ when } j \text{ is a substitutional element} \quad 4\text{-}26$$

$$D_{kj}^{n} = D_{kj} \text{ when } j \text{ is an interstitial element}$$

This equation indicated that concentration gradient of one element can cause diffusion of another element.

Combining Equation 4-21 and 4-26, the coupled partial differential equations (PDEs) are obtained to calculate the diffusion in a multicomponent system.

The flux-balance equation is shown below

$$v^{\alpha} c_k^{\alpha} - v^{\beta} c_k^{\beta} = J_k^{\alpha} - J_k^{\beta}, k = 1,2 \ldots\ldots, n \quad 4\text{-}27$$

Where v^{α} denotes the interface velocities in the α phase. c_k^{α} and c_k^{β} are phase concentrations at the interface; J_k^{α} and J_k^{β} are the diffusional fluxes of element k in the corresponding phases.

The accuracy of simulations by DICTRA dramatically depends on the accuracy of both the thermodynamic and kinetic data. As the calculation of phase diagrams (CALPHAD) method [91] in which the Gibbs energy has a relation with temperature and composition, the atomic mobility of each species as a function of temperature and composition was chosen to form the kinetic database. The equation of mobility of coefficient for species B is expressed as

$$M_B = \frac{M_B^0}{RT}\exp(\frac{-Q_B}{RT}) \qquad 4\text{-}28$$

M_B^O is a frequency factor, Q_B is an activation enthalpy. Both M_B^O and Q_B usually depend on composition, temperature and pressure.

The interdiffusion coefficients can be calculated by mobility and thermodynamic factors, shown below

$$L'_{kj} = \sum_{i=1}^{n}(\delta_{ik} - c_k V_i)c_i y_{va} M_i \qquad 4\text{-}29$$

Where δ_{ik} is the Kronecker delta; i.e., δ_{ik}=1, when j=k and δ_{ik}= 0 otherwise. c_k and c_i are the concentrations of elements k and i, V_i is the partial molar volume of element i, y_{va} is the fraction of vacant lattice sites on the sublattice where i is dissolved. The M_i is the mobility of i when i is an interstitial and the mobility divided by y_{va} when i is substitutionally dissolved.

The DICTRA software can solve the 1D diffusion controlled phase transformation and is the simplest method in obtaining quantitative kinetic information in many cases of interest. Phase transformation is solved by calculating the diffusion equation with a boundary condition such as equilibrium condition and closed system. Compared to the analytical and Howe's models I described above, DICTRA is better than them in some aspects: it uses thermodynamic and kinetic databases in consideration of the cross effects of different elements such as diffusion

coefficients and partition coefficients dependent on composition and temperature; it also uses a variable self-adjusting mesh.

4.5 Objective of this study

The aim of this work is to characterise the extent of segregation and compare that with analytical and numerical models for segregation behaviour in continuously cast microalloyed steel slabs and to identify composition-processing combinations with less segregation and better properties. The microstructure of as-cast continuously cast microalloyed steel slabs will be characterised by optical microscopy and scanning electron microscopy (SEM) in order to identify the dendritic structure. The cumulative profiles will be used to characterise the mirosegregation in different steel slabs. Phase transformation and segregation forming processes during casting will be simulated using Thermo-Calc software. The analytical approaches (Scheil and Clyne-Kurz) and DICTRA will be used to predict the microsegregation bahaviour for comparison with the experimental results. Based on the obtained results, the accuracy of these segregation models will be evaluated and experiments such as directional solidification trials may be carried out to further verify the models.

Chapter 5 Materials and Experimental Techniques

5.1 Materials

Four as-continuously cast low carbon microalloyed steel slabs (pipeline, structural, ship building and slab 1 steels) were investigated. Pipeline, structural and ship building (220 mm thick) steels were supplied by Shougang Steel Company, China, whilst slab 1 (290 mm thick and 1800 mm wide) was made by Corus, UK. The slab compositions are shown in Table 5-1; the analyses for the slabs supplied by Shougang did not include nitrogen, but the likely N levels should not strongly affect the solidification mode and segregation.

Table 5-1 Chemical compositions of as-cast continuously steel slabs and investigated ingot steel before and after DS (wt %)

	C	Si	Mn	P	S	Cr	Mo	Ni	Al	Nb	N	Ti	V	Cu
Pipeline	0.03	0.25	1.7	0.008	0.005				0.052	0.063			0.082	
Structural	0.06	0.3	1.52	0.01	0.003	0.021			0.0358	0.052				
Ship building	0.14	0.38	1.35	0.015	0.007	0.027	0.001	0.01	0.039	0.002		0.004	0.003	0.01
Slab 1	0.1	0.31	1.42	0.017	0.005			0.32	0.046	0.045	0.008	0.002	0.052	
High Al	0.1	0.29	1.42	0.018	0.004	0.01	0.005	0.32	0.057	0.019	0.008	0.001	0.052	
After DS	0.046	0.51	0.41	0.018	0.004	<0.01	-	0.48	<0.01	0.02	-	-	0.05	

Directional solidification (DS) casting trials were carried out using material from a high Al steel ingot (130×130×340mm). Casting shots and penny-shaped samples which are cylinders with a diameter of 50 mm and 25 mm and lengths of 30 mm and 3 mm respectively were cut from the high Al steel ingot and used for DS casting trials described later. After DS casting, the chemical composition was measured again, from a cross-section of the DS casting sample

in the middle position above where the thermocouple was located shown in section 5.1.1 using LEC1 (Leco CS444 Analyser) for carbon and ICP (Inductively Coupled Plasma Optical Emission Spectrometry) for the other elements in compliance with ISO/IEC 17025 because of evaporation of some of the alloying elements during casting. The chemical compositions of the high Al ingot steel before and after DS are shown in Table 5-1.

5.1 Directional solidification

5.1.1 Lost wax investment casting

A mould consisting of a circular cross-section bar with a cup top and flat bottom was made by lost wax investment casting, shown in Figure 5-1. The process used to make the moulds is summarised below.

First, the wax pattern which is the exact negative of the inner mould was made using a Mueller-Phipps wax injection machine fitted with a pre-existing die. Molten wax was injected into a standard mould to make a 200 mm height and 15 mm diameter cylinder; a cup-shaped top in which a cavity insert for a threaded hanger was embedded; and a flat bottom at high temperature and pressure. These three pieces were welded together to form a whole wax pattern and a manipulator handle was inserted, shown in Figure 5-2. Also, a 6 mm diameter and 15 mm length wax cylinder from the material left in the channel used to connect different parts in mould was welded onto the middle height surface of the wax bar, as drawn in Figure 5-2 as a green rectangle. The wax patterns were then degreased in Trisol 60 plus wax pattern cleaner for 45 s and dried by hanging on a carousel with a central diffuser (air blower).

Second, the ceramic shell was made by the investment casting process. This process consisted of two primary coats and six secondary coats and a final seal on the wax pattern. For each

primary coat or secondary coat, the operating process is summarised as follows. The wax patterns were invested in slurry made of silica sol and zirconium silicate filler and then alumina stucco was placed onto the surface of the wax model with a sieve. Before the next coating started, the previous coat was dried. Each primary coat was dried overnight and each secondary coat was dried for two hours. The final seal was applied by investing into slurry only without putting stucco on. The slurry and stucco particles (190 - 200 micro in diameter) as used for the primary coating were thicker and finer, to make a smooth inner surface, in contrast the outer of the mould is made of thinner slurry and greater sized stucco particles (350 - 600 micron in diameter) which made the coating strong enough to support the inner mould.

The viscosity of slurry was measured by the flow cups method in compliance with EN ISO 2431. The Cups with same volume and different sizes of orifices in the middle of the bottom were designed to measure the various viscosity ranges. Suitable cup was chosen according to experimental requirement. The orifice was sealed by a finger and a certain volume of slurry was poured into the cup. After removing the finger, the flow time was measured to control the viscosity of slurry. 28 - 32 s, B5 cup with 70 ml volume of slurry was used in primary coating process and 50 - 55s, B4 cup (whole cup) was used in secondary coating and final seal process identical with the standard method used in industry.

The ceramic moulds were then de-waxed in a kiln, whose heat hardens the silica coatings into a shell, and steam melts the wax quickly in order to avoid expansion and any cracking of the ceramic shell. The moulds were heated and pressurised to 453 - 553 K and 8.5 bar, kept in these conditions for 5 min and depressurized at 0.2 bar/min. The mould was then fired at 800 ℃ for 1 hour to increase the mechanical strength of the mould and also burn off any remaining wax and kept in a dry oven at 130 ℃ to stop moisture before DS casting.

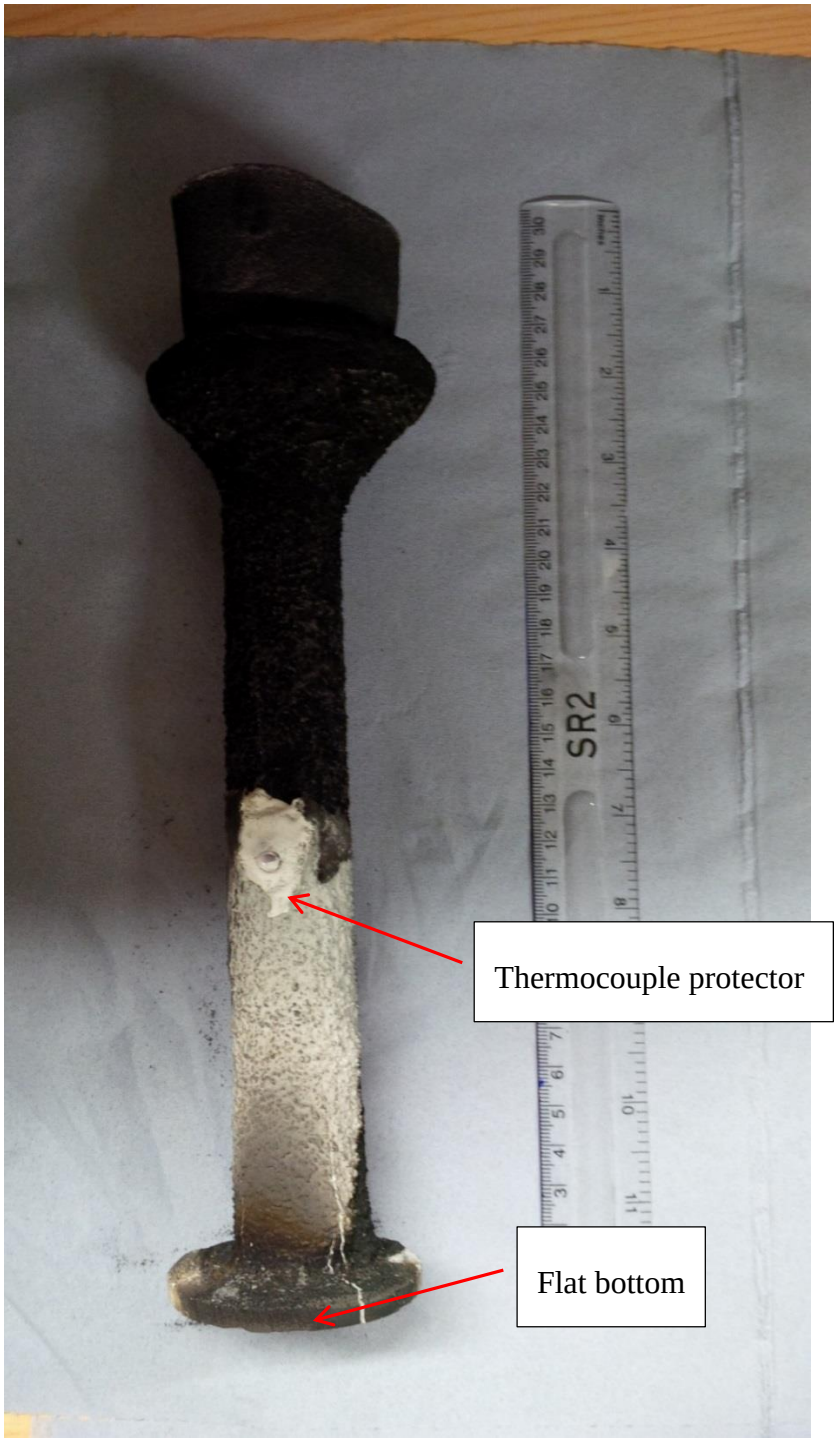

Figure 5-1 Mould made by lost wax investment casting after DS casting with thermocouple protector in the middle length of mould.

Figure 5-2 Wax pattern used for lost wax investment casting with a manipulator handle.

5.1.2 Thermocouple

Type B thermocouples containing two wires made out of platinum-30% rhenium for the positive leg and platinum-6% rhenium for the negative leg with twin-bore ceramic insulators were used to monitor the temperature during directional solidification in a temperature range from 300 to 1550 ℃. The 300 mm long thermocouples have a weld junction at one end and a

miniature plug at the other end. The measuring junction was covered by a 20 mm long, 4 mm ID alumina tube closed at one end which was put into the middle of the mould in order to protect the junction from dissolving by contacting the liquid metal directly. The thermocouple measured the metal temperature during casting based on an assumption that the inside of the one end closed alumina tubes has the same temperature as the metal it contacted. The gaps between the mould wall and alumina tubes were sealed by the Dyset air setting refractory cement to prevent the liquid metal from leaking through.

5.1.3 Directional solidification casting

The directional solidification (DS) of high Al low carbon steel was carried out in a vacuum casting furnace. The structure of the chamber in the furnace is shown in Figure 5-3. It contains a crucible, a heater with heating elements and built in thermocouples, chill spool and copper chill platform moved by a withdrawal system. Cold water goes through the chill spool and copper chill to remove heat. A baffle with a hole in the centre was put under the heater for insulation.

The directional solidification process is summarised below. The bottom of the mould was cut and ground to be flat (Figure 5-1) so that it can be put onto the copper chill platform and the liquid metal can contact the copper chill directly during casting. The junction terminal of the thermocouple was inserted into the one end closed ceramic tube and the other end was plugged into the socket under the copper chill, schematically shown in Figure 5-4. Vitreous aluminosilicate fibre was wrapped over the thermocouple hanging down in order to protect it from being splashed by metal liquid during pouring.

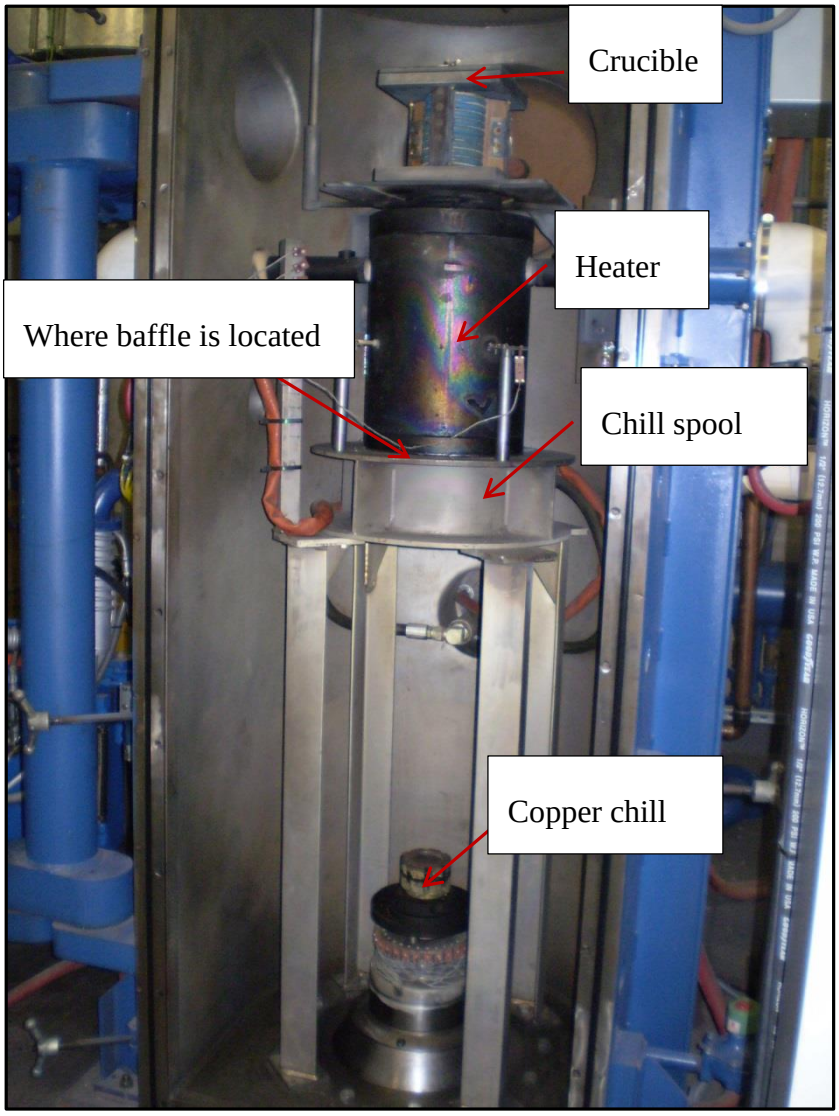

Figure 5-3 Structure of the chamber of the vacuum furnace for directional solidification.

The 50mm diameter and 30 mm height cylindrical sample was put into the crucible where they were melted and one penny shaped sample was used to cover the hole in the middle bottom of the crucible, as shown in Figure 5-5. The platform position was controlled to move up until the entire mould was inside the heater except the flat bottom through the centre hole of the baffle, then the chamber was evacuated to 0.04 mbar. The machine control system raised the temperature of the heater up to 1550 ℃. The cylindrical sample in the crucible first melted by heating elements and then the liquid metal dropped down and heated the penny

shaped sample in the bottom of the crucible. When the penny shaped sample melted, liquid metal poured down into the mould through the hole and was held in the mould for a 2 - 3 minutes. After that, the platform position was lowered at a specific withdrawal rate set up in advance until the mould completely exited the heater. The platform was withdrawn to the bottom of the chamber and the caster was shut down to cool down the whole chamber. During the whole casting procedure the thermocouple read the temperature every 1 second which was recorded by the computer connected to the furnace. Two DS trials were carried out. One withdrawal rate was 50 mm/hour, while the other withdrawal rate was 200 mm/hour initially and changed to 100mm/hour when the ram position had moved down by 140mm in order to decrease the portion of bainite in the microstructure and obtain a more clearly defined dendritic microstructure.

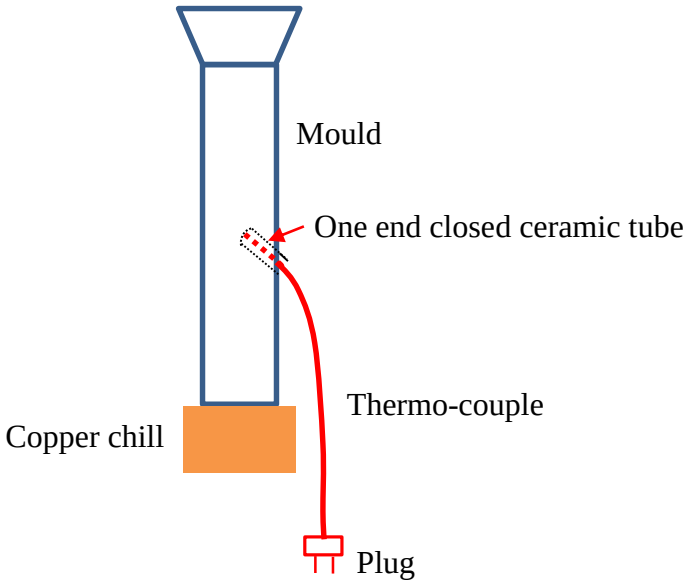

Figure 5-4 Schematic diagram showing the position of thermo-couple and one end closed ceramic tube in the mould.

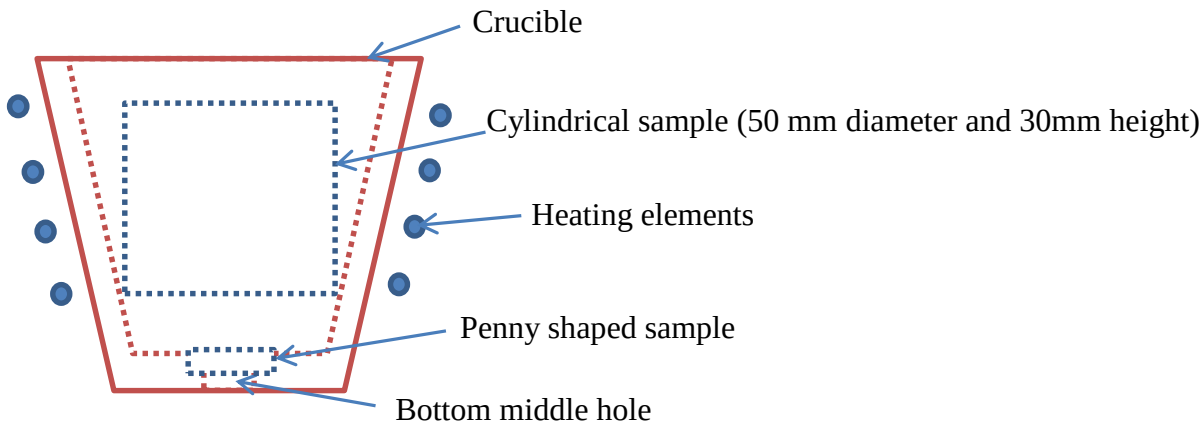

Figure 5-5 Schematic diagram of crucible with cylindrical sample and penny shaped sample inside.

5.2 Microstructural characterisation

5.2.1 Sample preparation

Longitudinal sections (parallel to the casting direction) of the structural steel slabs were cut from sub-surface (20 mm from top of the slab); quarter thickness from the top; mid-thickness: quarter thickness from the bottom and sub-surface from the bottom (20 mm from the bottom). Samples from the ship building, pipeline and slab 1 steels were taken at quarter thickness. The sections investigated in continuously cast steel slabs are schematically shown in Figure 5-6.

For the directionally solidified sample, a cross-section was cut 10 mm above the thermocouple position and a longitudinal section was cut 10 mm length above the cross-section. The DS sample with a fresh cross-section was sent to IncoTest for the elemental analysis.

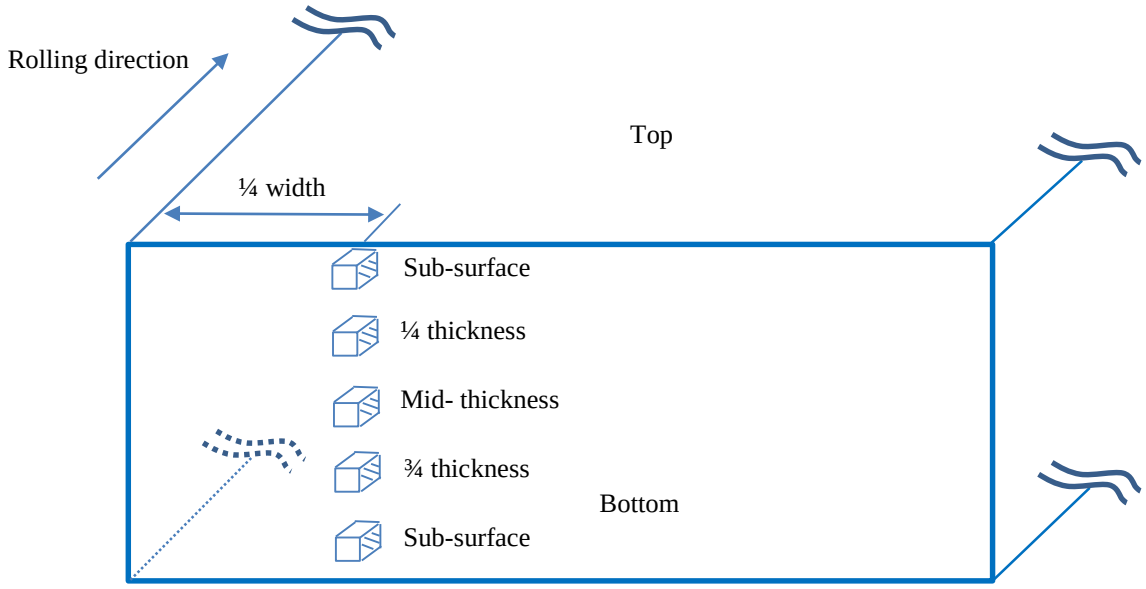

Figure 5-6 Schematic diagram showing the longitudinal sections (shaded areas) investigated at different positions along the thickness direction at ¼ width of a continuously cast steel slab.

For other samples, the fresh sections were mounted in conductive Bakelite and polished to a 0.05 μm OPA suspension finish. Some polished specimens were etched in 2% nital solution which contained 2 ml HNO_3 and 98ml ethanol for 5 - 10 seconds to show microstructures of the ferrite, pearlite, bainite and martensite.

5.2.2 Optical microscopy

The continuously cast and DS optical specimens were examined on a Zeiss Akioskop-2 microscope equipped with AxioVision image capture and analysis software. Image analysis software was used to measure quantitatively the ferrite grain size distribution with respect to the equivalent circle diameter (ECD); the fraction of second phase (pearlite); and the secondary dendrite arm spacing (SDAS). A number of images were captured at equal intervals on the etched surface at quarter thickness of the structural steel by the image capture

software. From these, a total of exactly 1000 ferrite grains were identified by the software automatically according to the contrast difference between the boundary and the inside of grains combined with manual correction. ECD of each grain was calculated by the analysis software. Similarly, ten images for each sample were taken at the same intervals to measure the pearlite fraction in terms of area fraction. By increasing the contrast difference between ferrite and pearlite, the analysis software picked up the black pearlite phase and calculated the ratio of black phase area to the whole frame area which is equal to the area fraction of pearlite phase. The average area fraction and standard deviation were calculated from the ten images for each sample. The secondary dendrite arm spacings (SDAS) were determined by measuring the distance from centre to centre of the interdendritic phase (pearlite). More than 100 SDAS values in each sample were measured on a montage merged from around 60 continuous views captured by the MosaiX Acquisition system with a 50x objective lens. The average SDAS values and standard deviations were calculated.

5.2.3 Scanning electron microscopy

The morphology of (Nb,Ti)(C,N) precipitates (approximate 40 – 400 nm diameter) in the as-cast slabs was characterised by a Jeol 7000 scanning electron microscope (SEM) at 20 kV with a field emission gun (FEG) to give high resolution at all operating voltages. The number density and area fraction of precipitates were measured from 10 continuous images on etched surfaces at quarter and mid-thickness positions of the structural steel slab. The precipitate sizes in terms of ECD and area fraction were measured by analysis software in the Zeiss Akioskop-2 microscope. The chemical composition of precipitates together with inclusions (MnS) were determined using the Jeol 7000 SEM fitted with Oxford INCA energy dispersive X-ray spectroscopy (EDS) at 10 mm working distance at 20 kV accelerating voltage. A dead time of around 30 % with a total count time of 120 s at an acquisition rate of more than 2kcps

was applied in EDS measurements by controlling the spot size. The process time was 5 s for point analysis. EDS grid scanning with 200 or 300 grid points in total for each sample was carried out in a number of continuous fields of view on polished samples at magnifications of 150x or 200x. The grid function in the INCA software was used to locate the spots where the electron beam sampled by setting up the distances between two adjacent points in x and y axial directions, shown in Figure 5-7. The element peaks in the spectra were checked manually by using the KLM markers and comparing the relative intensity between different lines. After confirming the elements according to the bulk composition and characteristic peaks in the EDS spectrum, the element concentrations and standard deviations were obtained in quantify spectra option in the Inca software.

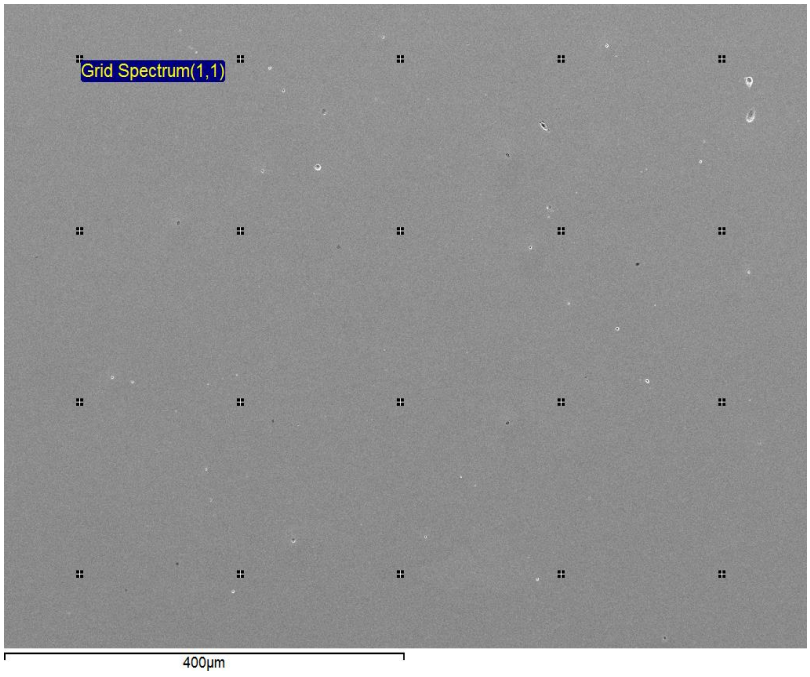

Figure 5-7 SEM picture overlaid by grid points on the polished surface.

5.3 Thermo-Calc and DICTRA

Version 4.0 of the Thermo-Calc software package with Thermo-Calc and DICTRA programs were used to model the microsegregation of continuously cast steel slabs and DS steels. The processes of using them were summarised below.

5.3.1 Thermo-Calc

There are two modes in Thermo-Calc: console mode and graphical mode and the graphical mode was chosen because it does not need to use the codes like console mode. A project for each steel was created and the chemical composition and specific phases (fcc, bcc, liquid, cementite, some inclusions and precipitates such as MnS) were input to define a system based on TCFe-7 database. In the system, the temperature range was 500 to 1600 ℃ and the pressure was 1.01325 bar. The property diagram equilibrium calculation was run in the interval of 10 degree from 1600 ℃ to 500 ℃. Different properties (amount of phase, composition of phase or enthalpy) can be plotted against temperature.

5.3.2 DICTRA

The basic workflow of the approach used in DICTRA simulation of solidification / cooling (Figure 5-8) is summarised below. A DICTRA simulation starts with the SYS module and defines the system by inputting the elements and phases and retrieves both thermodynamic and kinetic data from database files in the DATA module. After these, the DICTRA module is able to access the retrieved data used for defining the system. In the DICTRA module, the cooling rate, composition, geometry, boundary conditions and initial status of the system are defined. A system can contain several cells, each cell can contain several regions and the phase which each region contains must be defined. Parameters for numerical calculation can

be set as well in the DICTRA module, such as grid point distribution (grid spacing) and maximum time step etc. Finally simulation starts to run within the DICTRA module. The numerical procedure of DICTRA is shown in Figure 5-9. During simulation, at each grid point for each time step for a given temperature profile, thermodynamic and mobility data were retrieved to solve the diffusion equations. The diffusion equations at different grid points together with interfacial equilibrium equations from Gibbs energy were employed to solve the flux balance in order to obtain elemental composition at each grid point for each time step.

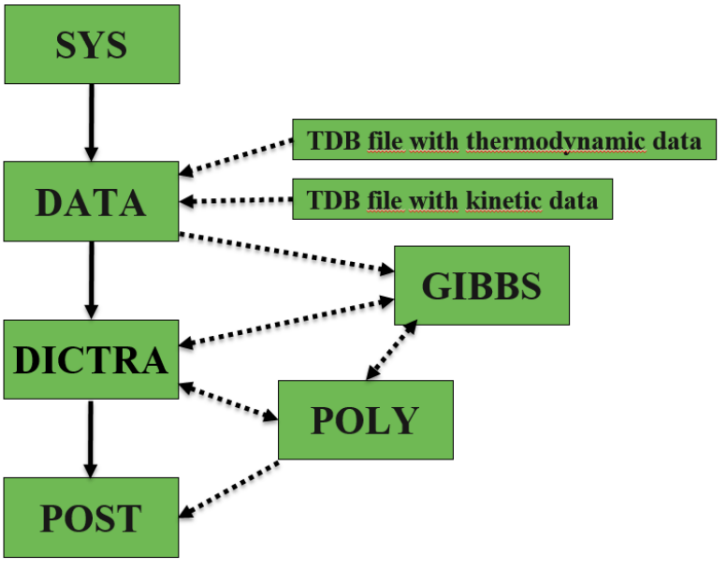

Figure 5-8 The basic workflow in DICTRA of different modules [122].

After running the simulation, all the information related to phase transformations containing phase forming temperature, composition distribution in the phase along the distance, phase growth velocity with time etc were stored in a dic format file. The chosen data can be plotted and visualised in the POST module. Among those results, the composition profiles as a function of distance between dendrite centre and interdendritic centre as a function of time (temperature) were used to compare with the experimental composition profiles.

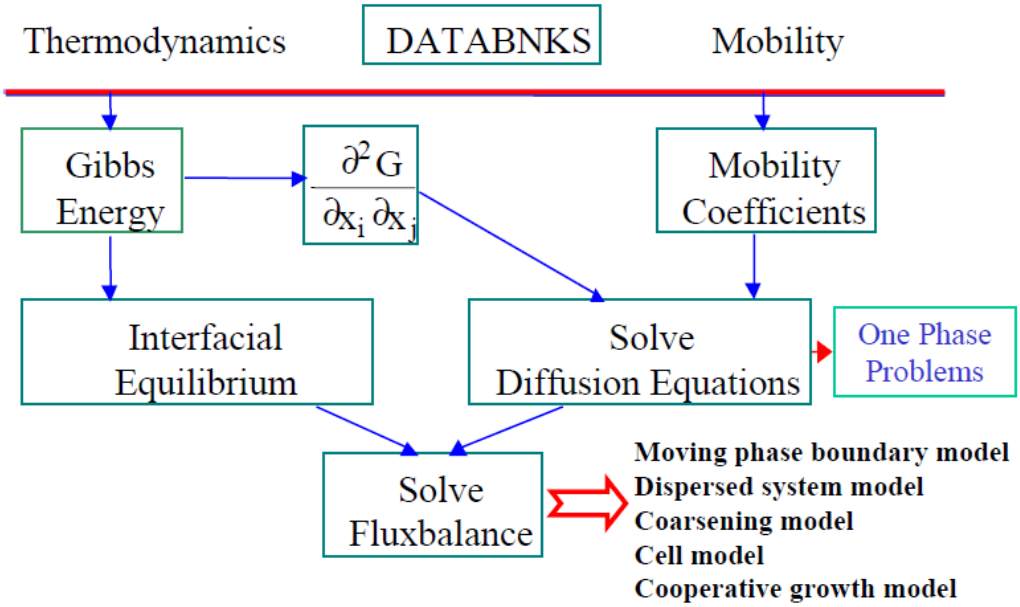

Figure 5-9 Numerical procedure of databanks.

DICTRA version 27 with the TCFe-7 thermodynamic database and the MOBFE-2 mobility database were used in this study. The composition investigated by DICTRA was simplified to be: Fe-C-Si-Mn(-Ni) for the whole casting process and Fe-C-Si-Mn(-Ni)-M (M is microalloying element M consisting of Nb and V) for the temperature range from the liquidus to the M-rich particle forming temperature in order to get the microalloying element distributions. During the whole casting process, the involved phases are liquid, δ-ferrite (bcc), γ-phase (fcc), α-ferrite (bcc) and cementite. The system was defined based on the elements and the phases were restored in both TCFe-7 thermodynamic and MOBFE-2 mobility databases for steels. 1-D linear modelling was adopted to be representative of the direction from the centre of dendrite to the interdentritic region. There was one cell used for the simulations which extended for half the SDAS length and one or more regions were set up within the cell to represent specific phases, such as a liquid phase region, bcc region and fcc region, as shown in Figure 5-10. In the cell the system was closed and mass conservation was maintained. The region was divided into a number of grids which was investigated in section

8.1.1 . The status of phases were active or inactive. Active phase means that it exists at the present condition and the inactive ones will form with time from the left hand side to right hand side by default. The interfaces in DICTRA were assumed to be under equilibrium or paraequilibrium conditions. No phase nucleus energy barriers (undercooling) were set up for all phase transformations. The composition was input in weight percent for the active phase in each region. The simulation time, the smallest and largest time steps were input to control the simulation; the simulation time was determined according to the cooling rates; the smallest time step is 1e-7 s by default; the largest time steps was discussed in the section 8.1.1 .

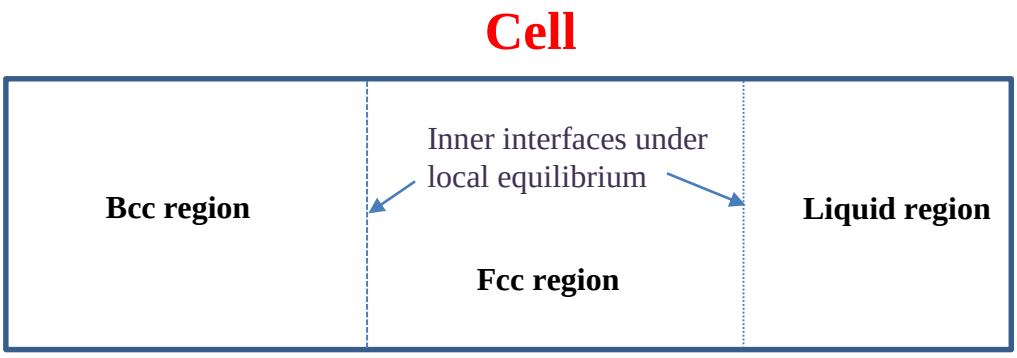

Figure 5-10 Schematic diagram of cell in which several regions (bcc region, fcc region and liquid region) exist with inner interfaces under local equilibrium.

Chapter 6 Microstructure and microsegregation characterisation of as-cast steels

Accurate quantification of microsegregation in low carbon continuously cast microalloyed steel slabs e.g. the solute- rich fractions and the distribution of alloying elements at the micro-scale is essential for the design of the subsequent hot rolling process. Hence it is necessary to characterise the microstructure and segregation of as-cast steels in order to understand solidification and segregation behaviour, which is reported in this chapter.

6.1 Macrosegregation characterisation in continuously cast structural steel slab

The chemical analyses for the as-cast slabs (Table 5-1) represent the overall composition; if these are to be used as a basis for microsegregation simulation, then it is necessary to confirm that macrosegregation is not significantly altering the overall composition where microsegregation is studied. The microstructures of the as-continuously cast structural steel slab at sub-surface, quarter-and mid-thickness positions are presented in Figure 6-1. At the sub-surface position the microstructure is composed of ferrite, acicular ferrite and pearlite, Figure 6-1 a). The region near the surface experienced the highest cooling rate so that acicular ferrite plates can be nucleated heterogeneously on non-metallic inclusions (Figure 6-2). Moving towards the inner part of the slab, the cooling rate decreases and the microstructures are mixture of ferrite and pearlite. In the central region, due to the centreline segregation, two narrow positive macrosegregation strips formed (about 1 - 3 mm wide for each strip), containing mixed microstructures of allotriomorphic ferrite, bainite and martensite, shown in Figure 6-3. According to reference [123], after heat treatment at 725 ℃ for 4 hours

(normalization) and air cooling, the microstructures through thicknesses in steels were transformed into near-equilibrium binary phases: ferrite and pearlite. Davis et al. reported that as-cast or normalised shipbuilding, structural steel and pipeline steels cast on the same caster (by Shougang company) show increased amounts of second phase (pearlite) towards the centre of the slab thickness, consistent with centre-line segregation increasing carbon and other alloying elements to increase hardenability and the amount of second phase formed on cooling; the variation for Slab 1 is much less because this was cast using soft reduction and so the level of macrosegregation was reduced leading to a more uniform microstructure [123].

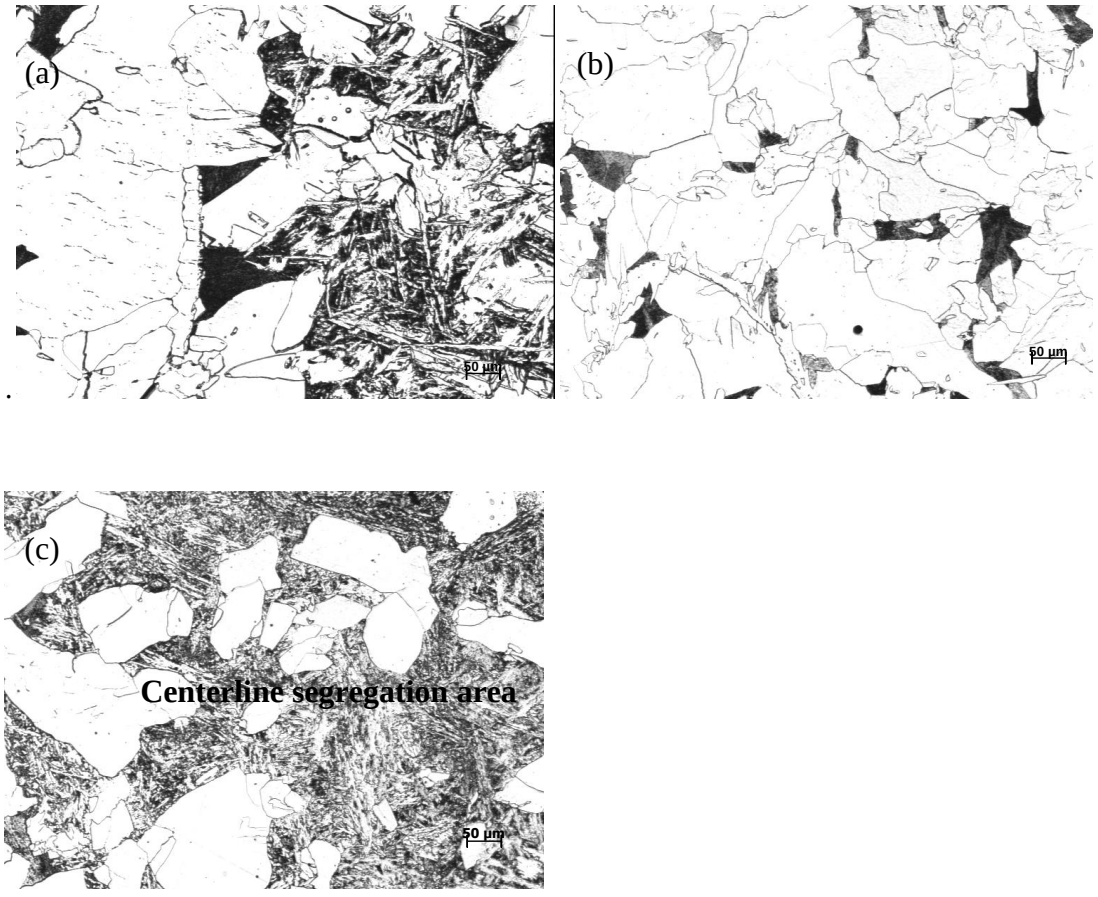

Figure 6-1 Microstructures at the depth of (a) 25.5 mm (sub-surface), (b) 71.5 mm (quarter thickness) and (c) 101 mm (mid thickness) in the structural steel.

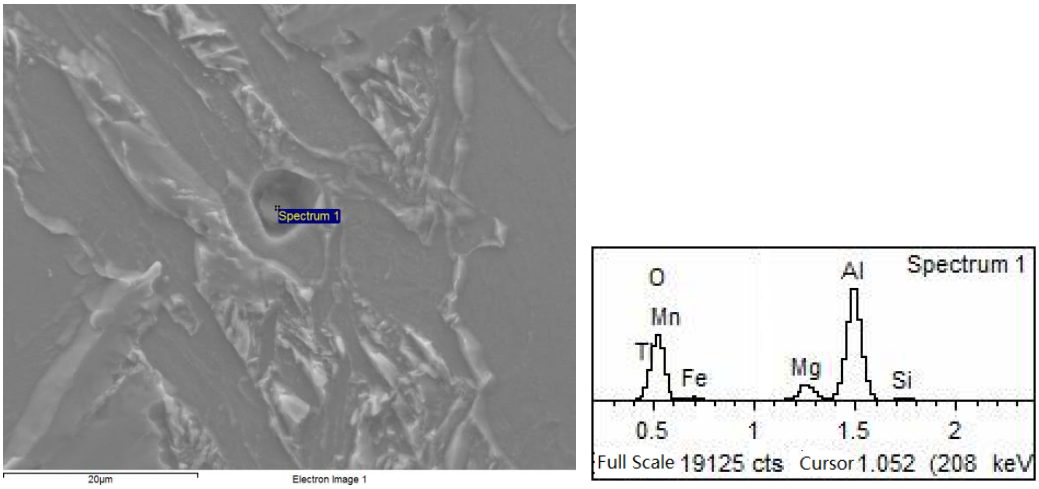

Figure 6-2 SEM image and EDS spectra of a non-metallic inclusion in as-cast structural steel in the sub-surface sample.

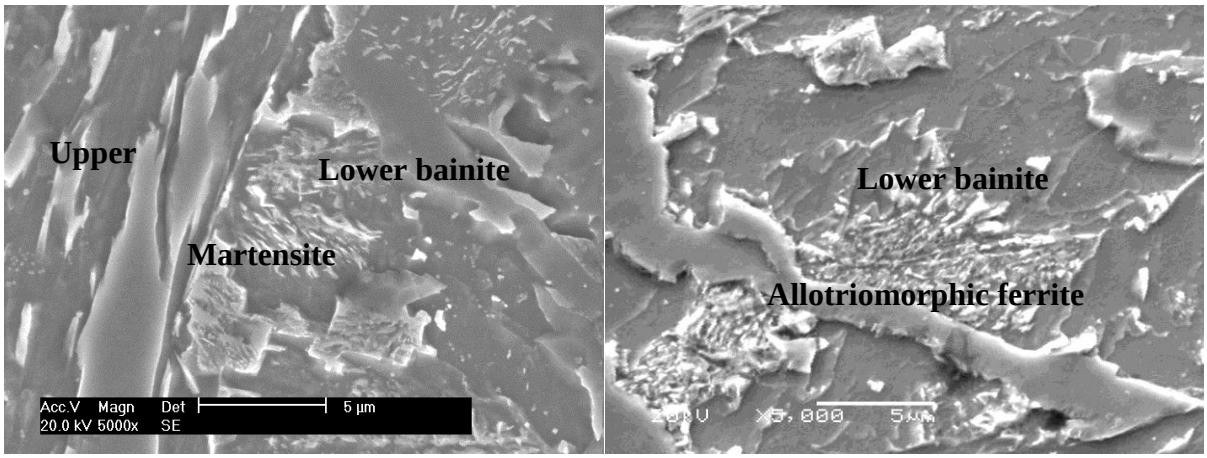

Figure 6-3 The SEM image of the centreline segregation region in the as-cast structural steel.

Nb-bearing steels are expected to show Nb concentration differences between centre-line and bulk regions due to its high partition coefficient (section 3.1.1). Spatial variation in the volume fraction of Nb(C,N) at sub-surface and mid-thickness in microalloyed steel has been observed [2]. The distribution of Nb(C,N) particles in as-cast structural steel at the centreline and the quarter thickness were determined and shown in Figure 6-4. Nb-rich precipitates were

in the size range 0 to 280 nm at the quarter thickness and 0 to 400 nm at the centreline segregated area. The average size, areal number density and volume fraction of Nb-rich particles at the centreline and the quarter thickness positions are shown in Table 6-1. The centreline segregated area has greater average size and volume fraction of particles than the quarter thickness position. Greater average size may be caused by slower cooling rate in the centre of slab allowing more time for the precipitates to grow. The greater volume fraction of particles in the centreline area indicates that macrosegregation has increased the Nb content.

Although centreline segregation exists in the as-cast steel slabs, most of the investigated steel slabs solidified with the bulk composition [123]. Within the region solidifying at the bulk composition, microsegregation was observed. Optical micrographs (Figure 6-5) revealed the as-cast microstructures of all steels from the quarter thickness position which consist of dendrites of ferrite separated by interdendritic pearlite. Average pearlite fraction values are shown in Table 6-2. The average spacing between pearlite colonies, taken as equal to the secondary dendrite arm spacing in as-cast continuously cast steel at the quarter thickness was measured, shown in Table 6-2. It was observed that some pro-eutectoid α-ferrite also formed on the MnS inclusions in the solute-rich region (pearlite region) shown in Figure 6-6. The dendritic structures of pipeline steel could not be observed clearly in optical micrographs due to the very small pearlite fraction, less than 2.0 %. Equation 3-1 was used to calculate the SDAS of pipeline steel listed in Table 6-2 by assuming a similar cooling history to the ship building steel because both of them contain the microalloying element Nb and were produced in same caster.

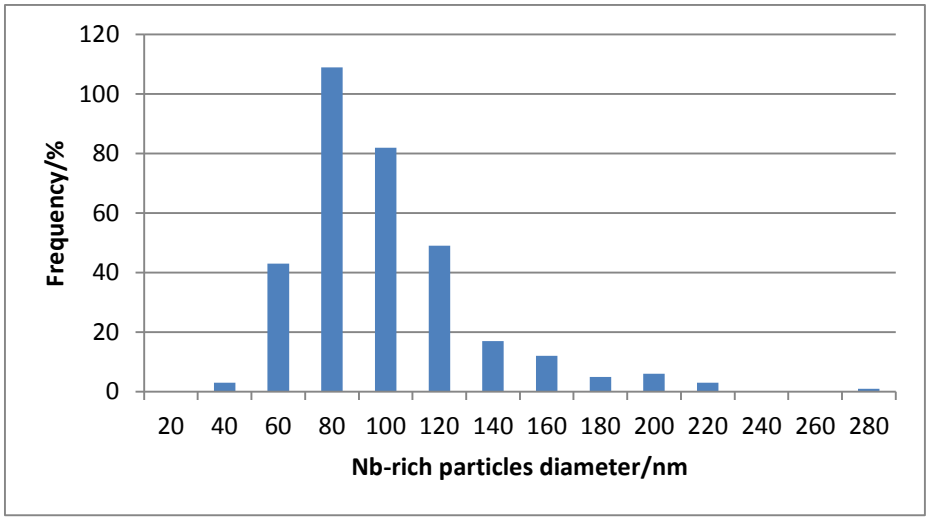

a)

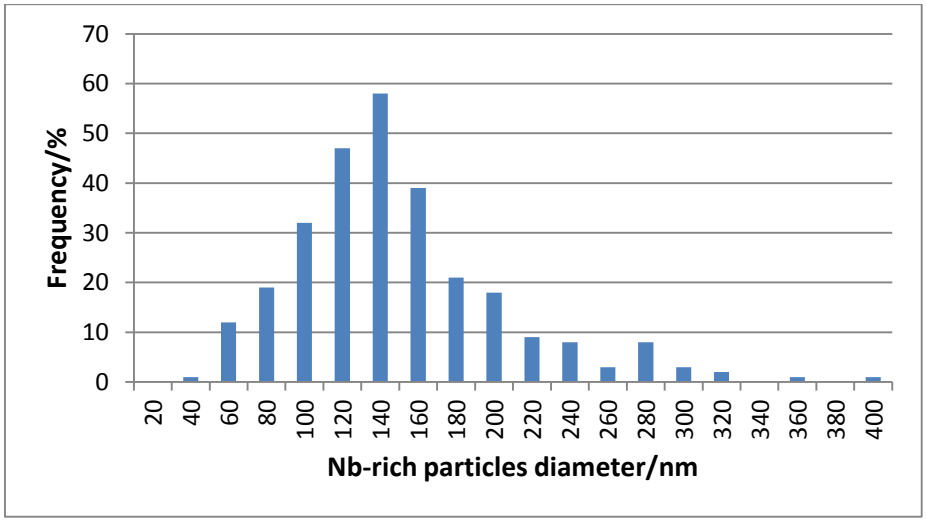

b)

Figure 6-4 Nb-rich particles size distribution at a) quarter thickness and b) centreline segregation area.

Table 6-1 Quantification of Nb-rich precipitate distribution in as-cast slab.

	Precipitate Area Density/ Number/mm^2	Precipitate average diameter/ nm	Volume fraction (%)
Quarter thickness	(20±12)×10^4	90±33	0.162
Centerline segregation areas	(13±4)×10^4	140±57	0.255

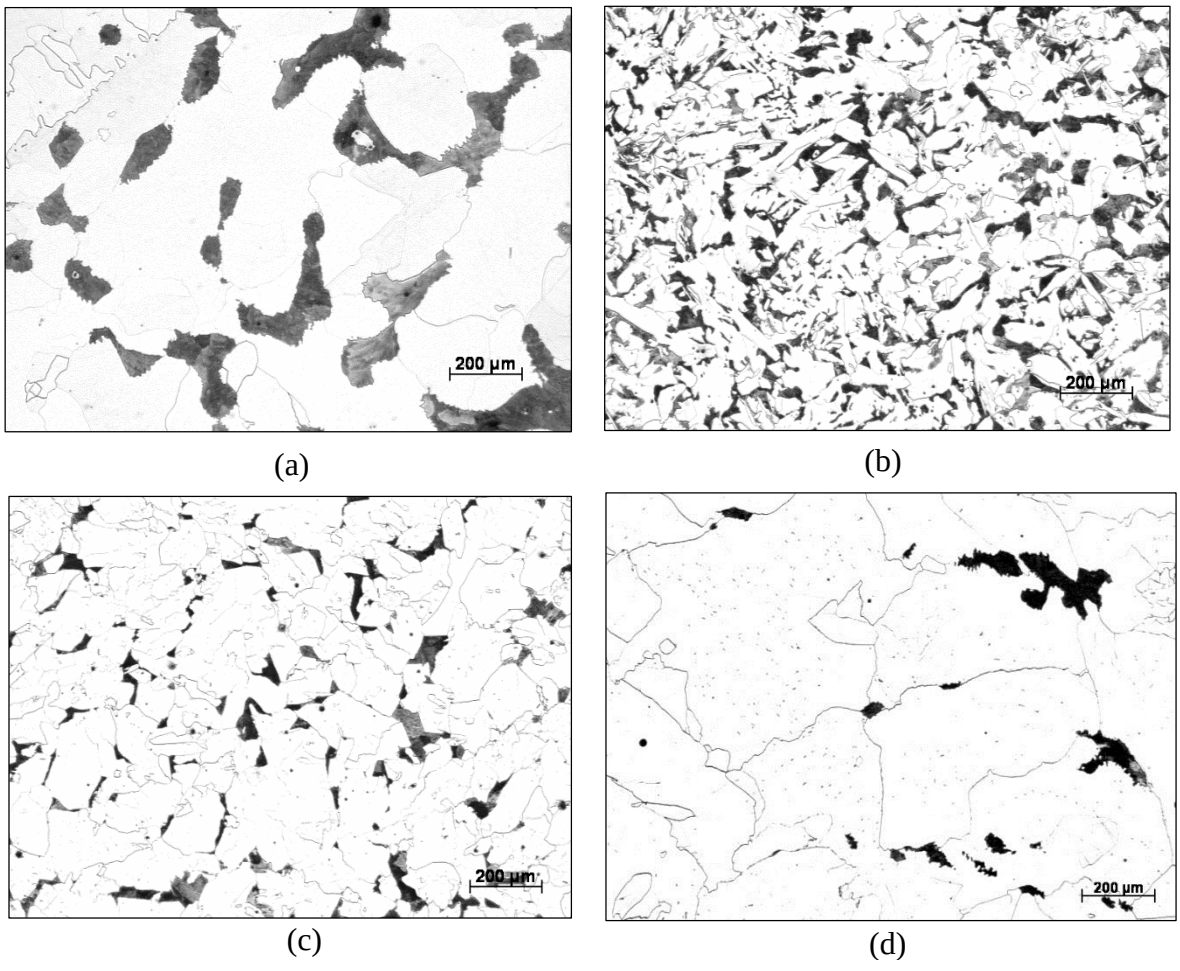

Figure 6-5 Example micrographs from (a) slab 1, (b) ship building, (c) structural and (d) pipeline steel slabs showing pearlite distribution in ferrite matrix at quarter thicknesses.

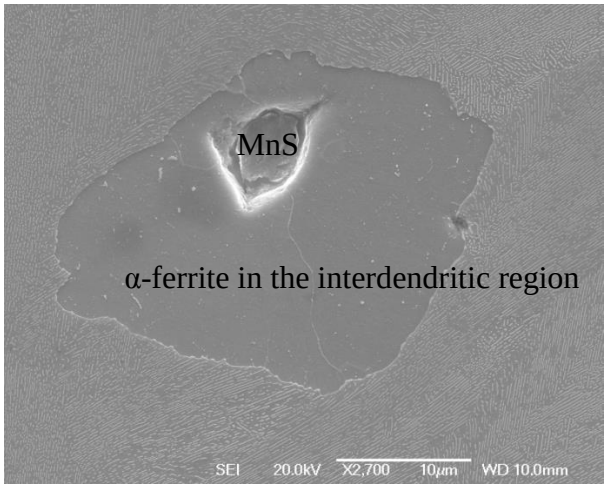

Figure 6-6 SEM image showing ferrite forming on the MnS inclusion inside pearlite corresponding to the solute rich region.

Table 6-2 Measured pearlite area fraction (%) and SDAS (μm) in as-cast continuous steel slabs

	Ship building	Slab 1	Structural steel	Pipeline
Measured Pearlite	22.4±1.4	17.7±2.4	8.3±1.3	<2.0
λ_{SDAS}	90±15	270±50	140±20	165

6.2 Quantification of microsegregation

Microsegregation affects microstructure and properties in as-cast steel and its response during subsequent processing, e.g. hot rolling. Therefore microsegregation at the quarter thickness position was characterised by grid-mapping, line scanning and cumulative profile methods using SEM-EDS detection technique.

6.2.1 Grid-Mapping

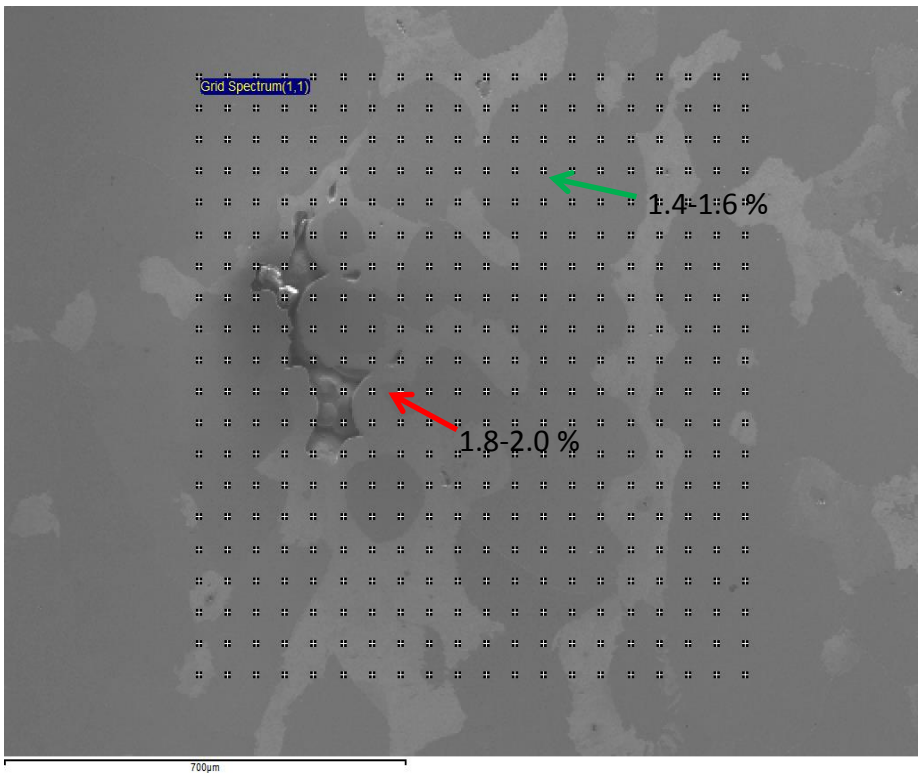

Figure 6-7 SEM image of an etched (in 2 % nital) as-cast slab 1 steel showing the dendritic and interdendritic areas with overlaid sampling square grid points.

The grid-mapping method was carried out on two fields of view of the etched surface in slab 1 steel at quarter thickness. The representative SEM image with overlaid grid points is shown in Figure 6-7. The results show that generally the Mn concentration in the pearlite phase (bright phase) is greater than that in ferrite phase (dark phase), e.g. pearlite near shrinkage cavity indicated by the red arrow with 1.8 - 2.0 Mn wt % and ferrite indicated by the green arrow with 1.4 - 1.6 Mn wt % with standard deviation of 0.12. This observation indicates that microsegregation exists in the as-cast steel and confirms that pearlite and ferrite phases correspond to solute-rich and solute-depleted regions.

6.2.2 Line-scans

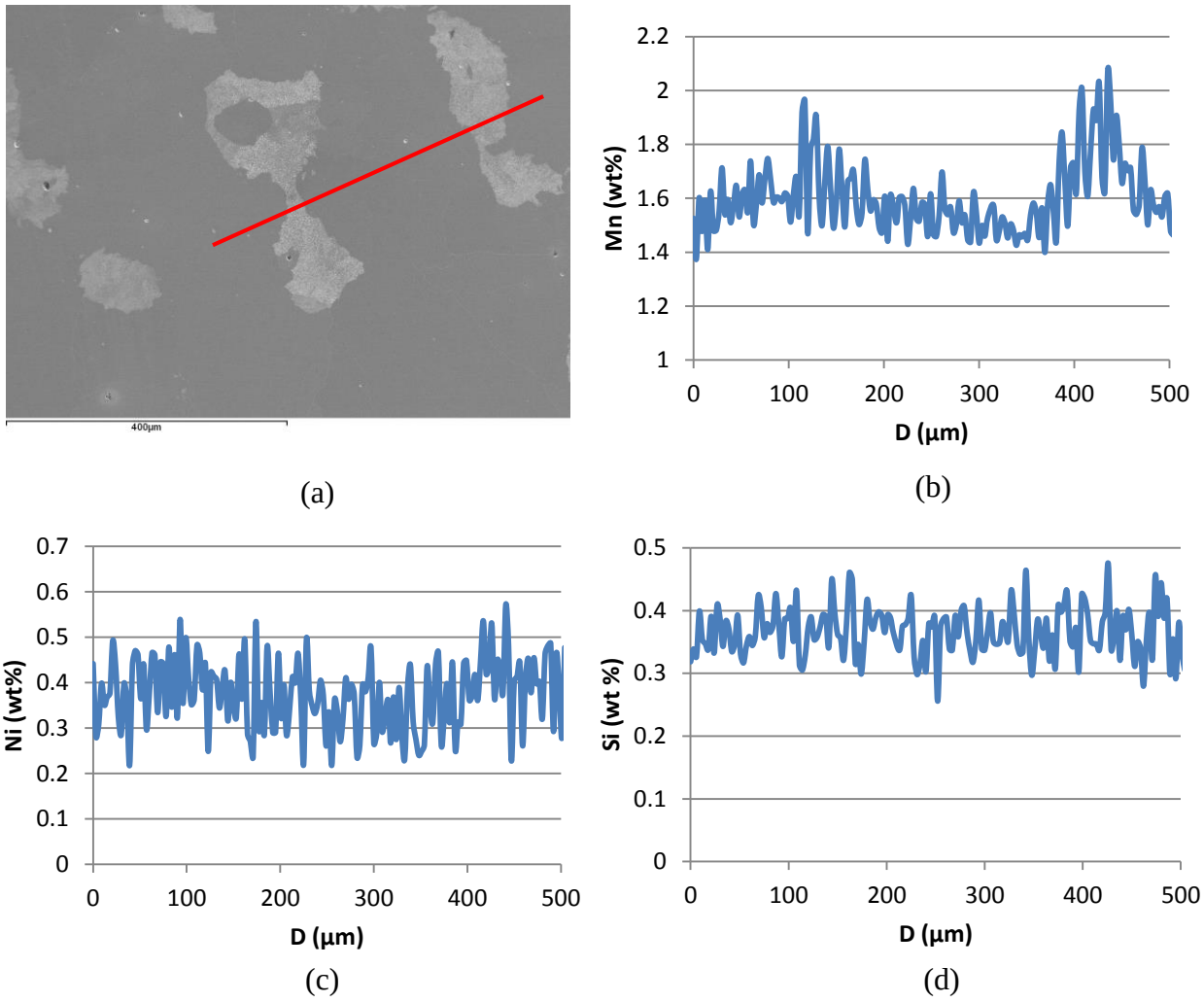

Figure 6-8 Representative line-scans analysis in slab 1 steel at quarter thickness across several dendritic structures (a) SEM image showing the dendrite and interdendritic regions with line-scan trace and composition distribution of (b) Mn, (c) Ni and (d) Si along the red dotted line.

In order to obtain more detailed segregation information, several line-scans analyses were carried out on the as-cast slab 1 steel across several dendritic regions. Figure 6-8 shows a representative EDS line-scan position (red line) across pearlite interdendritic solute-rich regions and ferrite dendrite solute-depleted regions and elemental (Mn, Si, Ni) distribution along the corresponding selected line. From the EDS line scan analysis, the peak of Mn and

Ni distribution with higher concentration corresponds to interdendritic pearlite region, however Si element distribution seems to show higher concentration even in the ferrite. Therefore, the Mn and Ni segregated into the interdendritic region, whereas the Si partition direction seems to be more complicated. The uncertainty and concentration range of each element in slab 1 steel are listed in Table 6-3. The uncertainty in Si and Ni element contents can affect the segregation profile more significantly than that of Mn. Therefore experimental segregation profiles may need to be analysed with consideration of partition direction during solidification. Line-scans are a 1-D method and EDS detection volume is about 1 micron below the surface, so the centre of the dendrite and the interdendritic region may not be detected fully by this method. Both line-scan and grid-mapping results show that Mn segregated to the interdendritic regions.

Table 6-3 Standard deviation and concentration range of each element from quantitative chemical analysis by SEM-EDS.

Element	Mn	Si	Ni
Statistical error σ (wt%)	0.13	0.08	0.13
Range	1.37-2.07	0.26-0.48	0.22-0.57

6.2.3 Cumulative profiles

In order to obtain more precise segregation distributions, the cumulative profiles method was used in the continuously cast steel slabs. EDS grid function was used on the polished surface to analyse a total of 200 or 300 points in each sample. The grid point spacing was greater than the SDAS values, which together with the number of grid points measured, are listed in Table 6-4.

Table 6-4 Experimental parameters used for SEM-EDS grid scanning to obtain cumulative profiles.

Steel	Structural	Pipeline	Slab 1	Ship building
Grid point spacing (μm)	400	280	400	150
Number of points	200	200	300	300

The average compositions and statistical deviations of various elements in the as-cast steel slabs determined by EDS are listed in Table 6-5. The differences between experimental average compositions and the nominal alloy composition (Table 5-1) for most results are beyond the accuracy ±5% of EDS measurements. Quantitative optimisations using copper and iron elements were carried out on all steel samples except slab 1. The degree of fit between reconstructed spectra based on the identified elements and real spectra was generally between 95% and 105%. The reason for the discrepancy may be contamination of the detector which affects the accuracy of the EDS results or the low level of macrosegregation in the quarter thickness region. Other microalloying elements such as Nb, are beyond the detection limitation of EDS (0.1 - 0.3 wt %) and could not be detected accurately.

Table 6-5 Nominal composition, C_0, mean composition, C_0^{EDS} of analysis region by SEM-EDS and their associated measurement uncertainties, σ_0^{EDS}.

Steel		Mn	Si	Ni
Slab 1	C_0	1.42	0.31	0.32
	C_0^{EDS}	1.54	0.37	0.34
	σ_0^{EDS}	0.11	0.07	0.13
Ship building	C_0	1.35	0.38	-
	C_0^{EDS}	1.44	0.43	-
	σ_0^{EDS}	0.12	0.08	-
Pipeline	C_0	1.7	0.25	-
	C_0^{EDS}	1.89	0.34	-
	σ_0^{EDS}	0.14	0.09	-
Structural	C_0	1.52	0.3	-
	C_0^{EDS}	1.60	0.33	-
	σ_0^{EDS}	0.12	0.08	-

6.2.3.1 Ranking of EDS data and assignation of solid fraction

According to the analysis of line-scans, both Mn and Ni segregated into the interdendritic region and can be used as weighted elements in WRIS method. In this study, only three elements (Mn, Si and Ni) can be detected in the matrix of steels and the WRIS method requires at least two weighted elements. Therefore, for the slab 1 steel with Mn, Si and Ni, both WRIS (based on Mn and Ni) and Mn single-element sorting (SES) methods can be applied to sort the data, while for the structural, ship building and pipeline steels with Mn and Si only, Mn SES sorting has been employed to obtain the segregation profile. The elemental

data for Mn, Si and Ni were first normalised by dividing by the average composition. The normalised data were ranked and assigned solid fraction according to section 3.2.3 .

6.2.3.2 Results

The Mn concentration data were sorted and assigned a solid fraction as mentioned in section 3.2.3.5 . The Mn distribution profiles against solid fraction sorted by Mn SES method are shown in Figure 6-9. Mn content increased steadily and continuously without any scatter. Mn concentration profiles had similar shapes: with increasing solid fraction, the Mn content initially increased quickly and the slope decreased to a constant value and then increased again in the last, right-hand part of the profile. The slope change in the right-hand part of the profiles may correspond to the change of partition coefficients between solid and liquid due to peritectic reaction during solidification which will be discussed in the further sections. Therefore, the slope changing points in the right-hand part of the profiles were regarded as the separation points between solute-rich and solute-depleted regions. The fractions of solute-rich regions obtained from the Mn segregation profiles are listed in Table 6-6 and increased with increasing carbon content which affected the peritectic temperature. Lower carbon steels (structural, and pipeline steel) have less solute-rich fraction (of around 3 %). In contrast, slab 1 and ship building steels have greater solute-rich area (more than 10%).

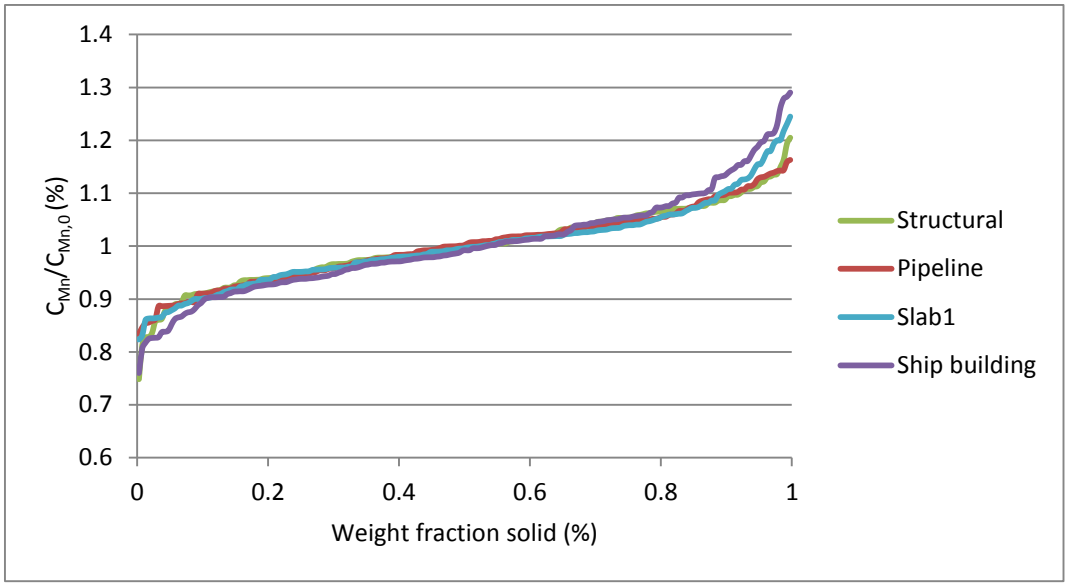

Figure 6-9 Mn content as a function of solid fraction in Pipeline, Structural, Ship building and Slab 1 steels.

Table 6-6 Solute-rich fractions of steels from experiment measurements.

	Slab 1	Ship building	Structural	Pipeline
Solute rich fractions (%)	10-17	12-20	3	0

The comparison between SES and WIRS was investigated in slab 1 steel shown in Figure 6-10. The scatter-free Mn profile by SES fitted well with the scattered WIRS profile except the very left-hand part in which SES data were lower than WIRS data and produce a small tail. Si profiles sorted by SES and WIRS have similar results in which the Si content seems to decrease with increasing solid fraction. However, SES Ni profile shows greater scatter than WIRS Ni profiles. The uncertainty of WIRS profiles is similar as the standard deviation of normalised element content ($C_M/C_{M,0}$) produced by EDS, listed in Table 6-7. Therefore WIRS is better than SES in terms of less scatter in the Ni profiles. SES sorting gives reasonable

results for Mn and Si profiles and can be used for sorting Mn and Si data with consideration of the standard deviation produced by EDS.

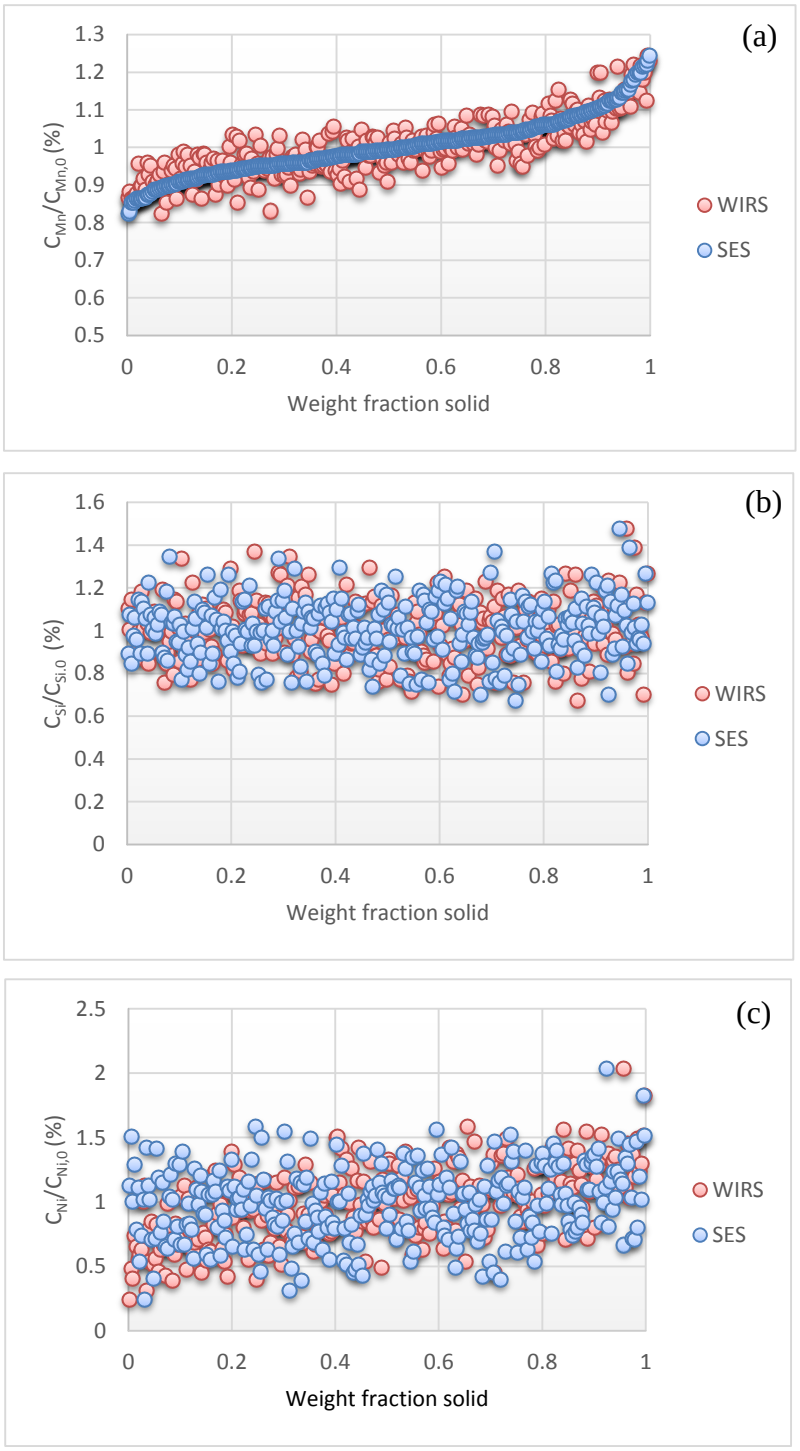

Figure 6-10 The cumulative composition profiles of (a) Mn, (b) Si and (c) Ni sorted by SES and WIRS for slab 1 steel.

Table 6-7 The uncertainty of normalised elemental concentration ($C_M/C_{M,0}$) produced by EDS.

Steel	Mn	Si	Ni
Slab 1	0.08	0.19	0.35

6.3 Conclusions

In continuously cast steel slabs, macrosegregation existed across the thickness direction. In structural steel, centreline segregation regions were observed in the mid- thickness position with harder microstructures containing bainite and martensite. In the quarter thickness, the microstructures are a mixture of pearlite and ferrite representative of the bulk composition. The secondary dendrite arm spacing (SDAS) at quarter thickness was characterised by measuring the distance between adjacent parallel pearlite colonies.

Mapping, line-scan and cumulative profile methods were executed to characterise the elemental segregation in as-cast steel slabs. By analysing mapping and line-scans, Mn and Ni were observed to segregate into the interdendritic region, but Si seemed to have more complicated partition behaviour. Both WRIS and SES methods were applied to slab 1 steel to obtain element distribution profiles, while only SES sorting was used for structural, ship building and pipeline steels. Mn segregation profiles obtained by sorting monotonically increased in concentration with assigned solid fraction have similar shapes: sharp slope initially, shallow sloping middle part and higher sloping last part. The slope changing points between the middle and last parts are assumed to separate the solute-rich and solute-depleted regions. The solute-rich fractions characterised according to the cumulative profiles increased with the increasing carbon content. Comparing the SES with WRIS methods, the scatter-free SES Mn profile produced a small tail with lower Mn content than WRIS profile in the

dendrite centre region in the solid fraction range of 0 to 1.5 wt %. WRIS is better than SES in terms of less scatter in the Ni profile. However, the SES method is still suitable to sort Mn and Si data taking into account their standard deviations.

Chapter 7 Microsegregation modelling by Thermo-Calc software and analytical approaches

Microsegregation from continuous casting of steels affects the microstructure and mechanical properties of final products as mentioned before. It is useful to predict the microsegregation in the steel in order to optimise the casting and subsequent processing, e.g. hot rolling. Therefore, modelling of microsegregation was carried out for the continuously cast steels, whose characterisation was covered in Chapter 6 . Thermodynamic modelling software (Thermo-Calc) under equilibrium conditions and analytical approaches (covered in section 4.2) were applied as a first step to simulate the microsegregation in the steels. Although the centre-line segregation of some continuously cast slabs has been characterised in the previous chapter, 80% of the slab thickness solidified as the bulk composition. For those regions, microsegregation can be predicted using the bulk composition as a starting point.

7.1 Solidification modelling by Thermo-Calc software

7.1.1 Solidification sequences predicted by Thermo-Calc

As shown in section 3.1.1 , the matrix phase transformations during solidification influence the degree of microsegregation and so Thermo-Calc was used to predict the equilibrium solidification sequences for the alloys investigated. The solidification sequences and typical solidification temperatures (liquidus, peritectic and solidus) in the studied steels predicted based on the bulk composition by Thermo-Calc software are listed in Figure 7-1. Due to the different compositions, especially carbon contents, the predicted solidification sequences were divided into two categories: pipeline and structural steels with lower carbon content (0.03 - 0.06 wt % C) solidified fully as δ-ferrite before transforming to austenite, but the temperature

range of the structural steels for the single phase δ-ferrite field is 1 ℃, indicating that if liquid is not solidified under equilibrium conditions, then there may be some mixed δ-ferrite and austenite coexisting before solidification finishes, Slab 1 and ship building steels with higher carbon content (1.0 - 1.4 wt % C) solidified through the peritectic reaction which means before liquid fully transformed to δ-ferrite, austenite nucleates at the δ-ferrite/liquid interface. For slab 1 and the ship building steel, inclusions of MnS form whilst the steel is still partially in the liquid phase, whereas MnS only comes out of solution in the solid phase after solidification in pipeline and structural steels.

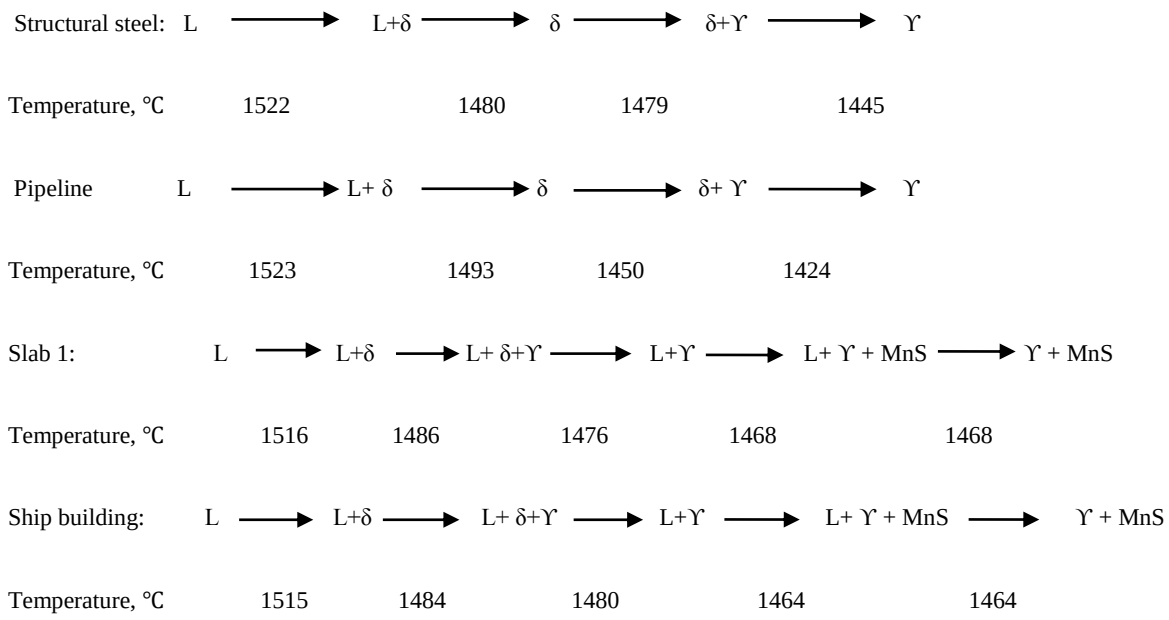

Figure 7-1 Solidification sequences for all continuously cast steels, with critical temperatures predicted by Thermo-Calc software, Liquid (L), δ-ferrite(δ) and austenite(γ).

As temperature goes down, C and N-rich particles begin to precipitate. Generally particles are carbides, nitrides or carbonitrides of Nb, Ti, V and Al, shown in Figure 7-2. In slab 1 steel, the Ti(N) particles are predicted to precipitate first and then the Nb(C,N), AlN and V(C) form in order on cooling further. Ti(N) is predicted to be dissolved with decreasing temperature probably caused by formation of AlN in which N is more stable with lower Gibbs energy

under equilibrium condition. However, in practice, the precipitates do not have enough time to dissolve into the matrix to obtain the equilibrium condition. On further decrease in temperature, proeutectoid ferrite is predicted to form followed by the eutectoid transformation when the remaining austenite transforms to pearlite. Therefore, the final microstructures of the samples studied were mixtures of ferrite and pearlite with a variety of inclusions and precipitates.

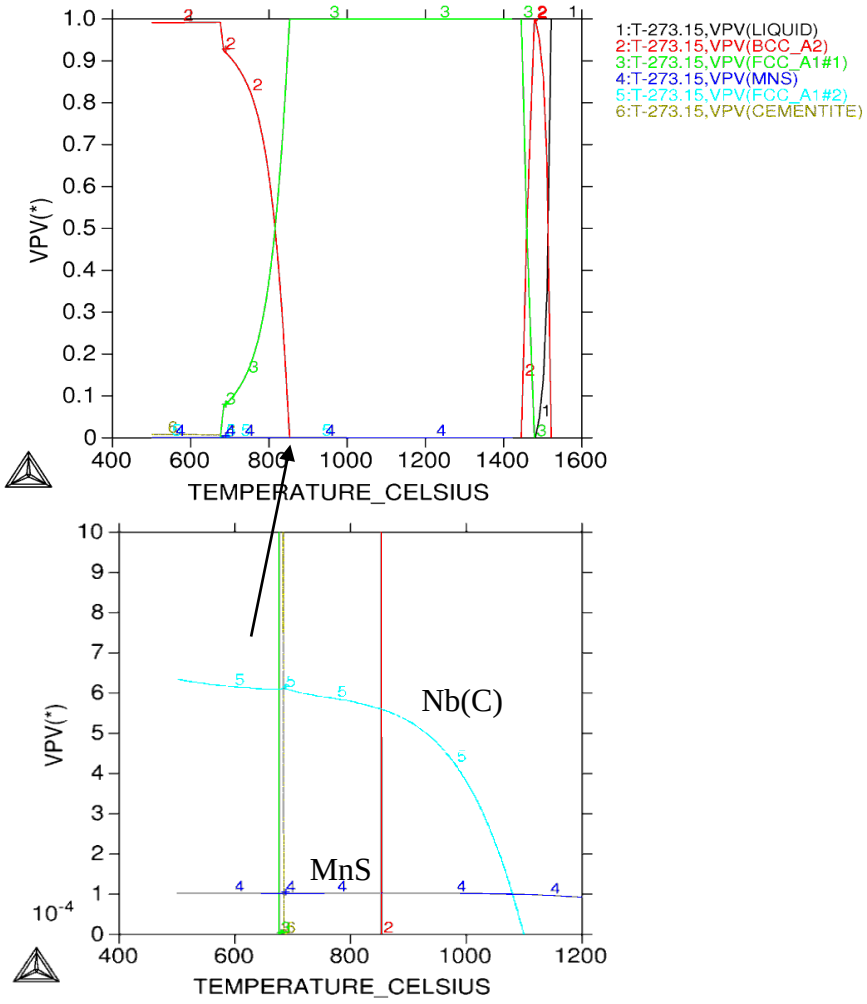

(a)

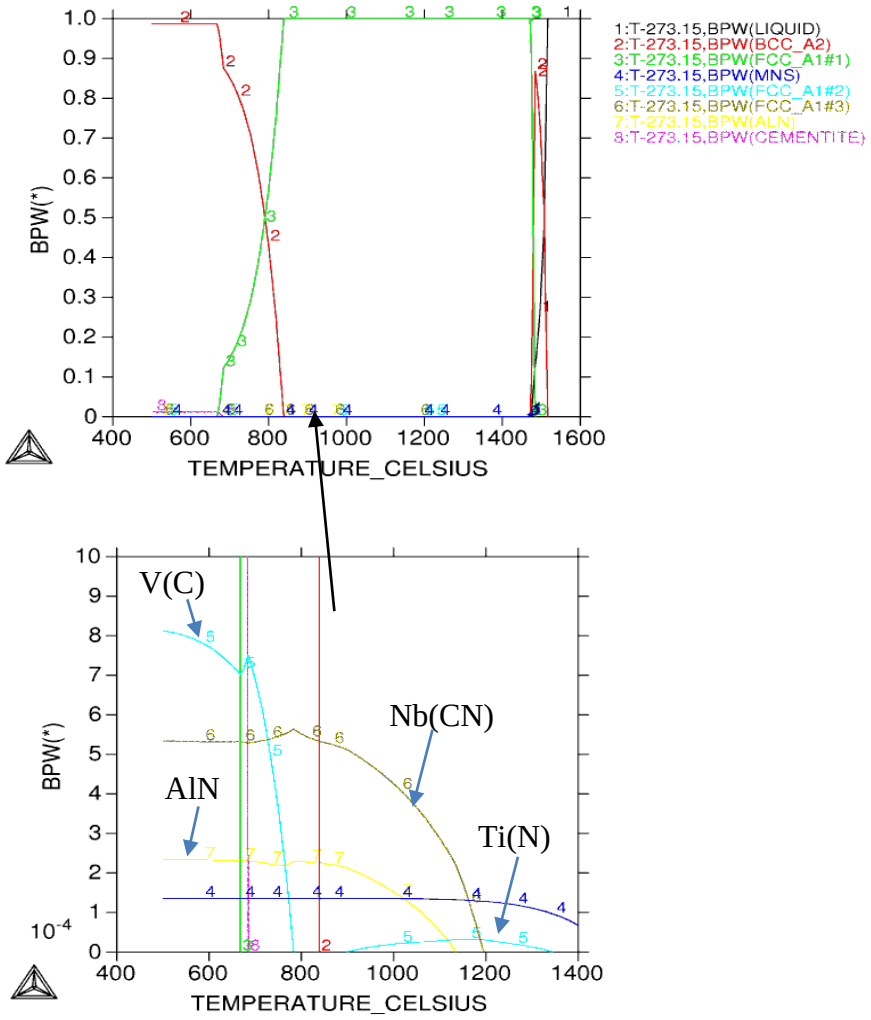

(b)

Figure 7-2 Weight percent of phases as a function of temperature in as- cast a) structural steel slab and b) slab 1 steel predicted by Thermo-Calc.

7.1.2 Partition coefficients predicted by Thermo-Calc in steels with peritectic reaction

The partition coefficient is an important parameter to characterise the segregation tendency of alloying elements during solidification. Thermo-Calc was used to predict the partition coefficient $k^{\delta/L}$ and $k^{\gamma/L}$ under equilibrium conditions taking into account the multicomponent effect in low carbon microalloyed steels. The partition coefficients were calculated by

dividing predicted elemental concentration in solid δ or γ phases by that in liquid. The mean partition coefficient was determined by averaging the partition coefficients at the temperatures from the solidus to the liquidus with an interval of 5 ℃. The elemental concentrations in different phases at different temperatures were obtained by the calculation of property diagram in Thermo-Calc for each steel. Figure 7-3 shows how the element concentrations change with temperature during solidification. It illustrates that $k^{\delta/L}$ and $k^{\gamma/L}$ are not constant but decrease with decreasing temperature, e.g. from 0.70 to 0.66 for $k^{\delta/L}$ of Mn and from 0.20 to 0.18 for $k^{\delta/L}$ of Nb in slab 1 during solidification. Also, compared with the partition coefficients from literatures obtained from binary systems in the section 3.1.1 , most Thermo-Calc predicted partition coefficients are smaller indicating the interactions with other solutes should be considered. The smaller the partition coefficients are, the more severe the microsegregation is.

In addition, the concentrations in austenite for some elements such as C, Ni, Mn are intermediate between those in δ-ferrite and liquid, in the category of austenite-forming elements (Figure 7-3 a), whereas for other elements called ferrite-forming elements like Nb the concentration in δ-ferrite is in- between those in austenite and liquid (Figure 7-3 (b)).

The mean $k^{\delta/L}$ and $k^{\gamma/L}$ values in slab 1 were calculated and listed in Table 7-1; these were used for all the analytical approaches applied to each steel in later sections by neglecting small differences between different steels.

Among substitutional alloying elements, Nb and Ti have a very small $k^{\delta/L}$ value of around 0.2 indicating severe segregation during solidification, while other substitutional elements (Si, Mn, V, Ni and Al) with predicted partition coefficients nearer 1 are assumed to have less

segregation. According to the prediction from Thermo-Calc, all elements segregated into the interdendritic liquid region except Al which partitioned into the centre of the dendrite.

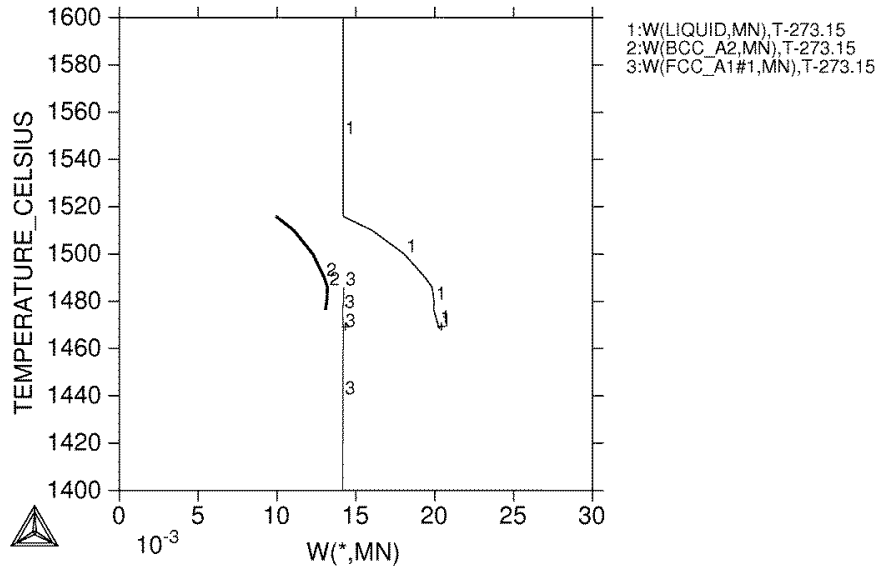

(a)

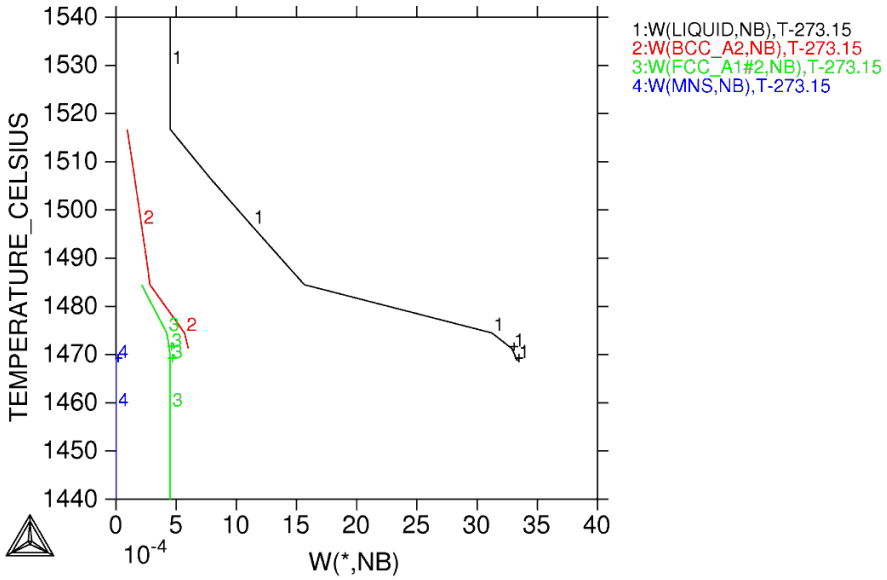

(b)

Figure 7-3 (a) Mn and (b) Nb contents in δ-ferrite, liquid and austenite of slab 1 steel as a function of temperature.

Table 7-1 Predicted mean equilibrium partition coefficients $k^{\delta/L}$ and $k^{\gamma/L}$ by Thermo-Calc in low carbon microalloyed steels

	C	Si	Mn	P	S	Ni	Nb	Ti	V	Cr	Al	N
$k^{\delta/L}$	0.15	0.63	0.68	0.29	0.02	0.78	0.19	0.26	0.74	0.9	1.32	0.30
$k^{\gamma/L}$	0.29	0.62	0.70	0.19	0.01	0.89	0.13	0.19	0.56	0.89	1.22	0.55

7.1.3 Segregation development hypothesis for Nb-bearing, low carbon steel based on Thermo-Calc prediction

A scheme for the development of microsegregation during casting was proposed according to previous Thermo-Calc prediction of steels in section 7.1.1 . Nb was chosen to illustrate the formation of microsegregation. The steels were assumed to solidify through the peritectic reaction as illustrated in Figure 7-4. δ dendrites first form inside the liquid (Figure 7-4a). The solute element atoms are rejected by the solid into the interdendritic liquid, so the δ phase contains low Nb content and the liquid in the interdendritic space is enriched in Nb. As temperature decreases below the peritectic temperature, austenite nucleates at the δ/liquid interface and grows into both the δ phase and liquid (Figure 7-4 c, d). Due to the low diffusion rate in the γ phase, the solute is trapped in the liquid and solute-rich regions form.

High Nb content is assumed to be in the centre of the austenite grains (Figure 7-4 c) and the grain boundaries are low Nb regions. After complete transformation to austenite, the solute element atoms diffuse from high concentration into low concentration regions in the austenite single phase. The temperature at which Nb-rich precipitates are predicted to come out from solution increases with increasing Nb concentration as predicted by Thermo-Calc. Nb(C,N) precipitates first nucleate in the Nb-rich regions in the interdendritic regions. With decreasing

temperature, the Nb-rich particles form in the Nb-depleted regions and the average size of particles is probably smaller with a lower volume fraction in Nb-depleted regions than in the Nb-rich regions. When the temperature falls below A_3, proeutectoid α phase forms at the γ grain boundaries in the dendrite centres and grows into the surrounding austenite (Figure 7-4e). Pearlite is finally formed in the remaining austenite related to the solute-rich region (Figure 7-4 f).

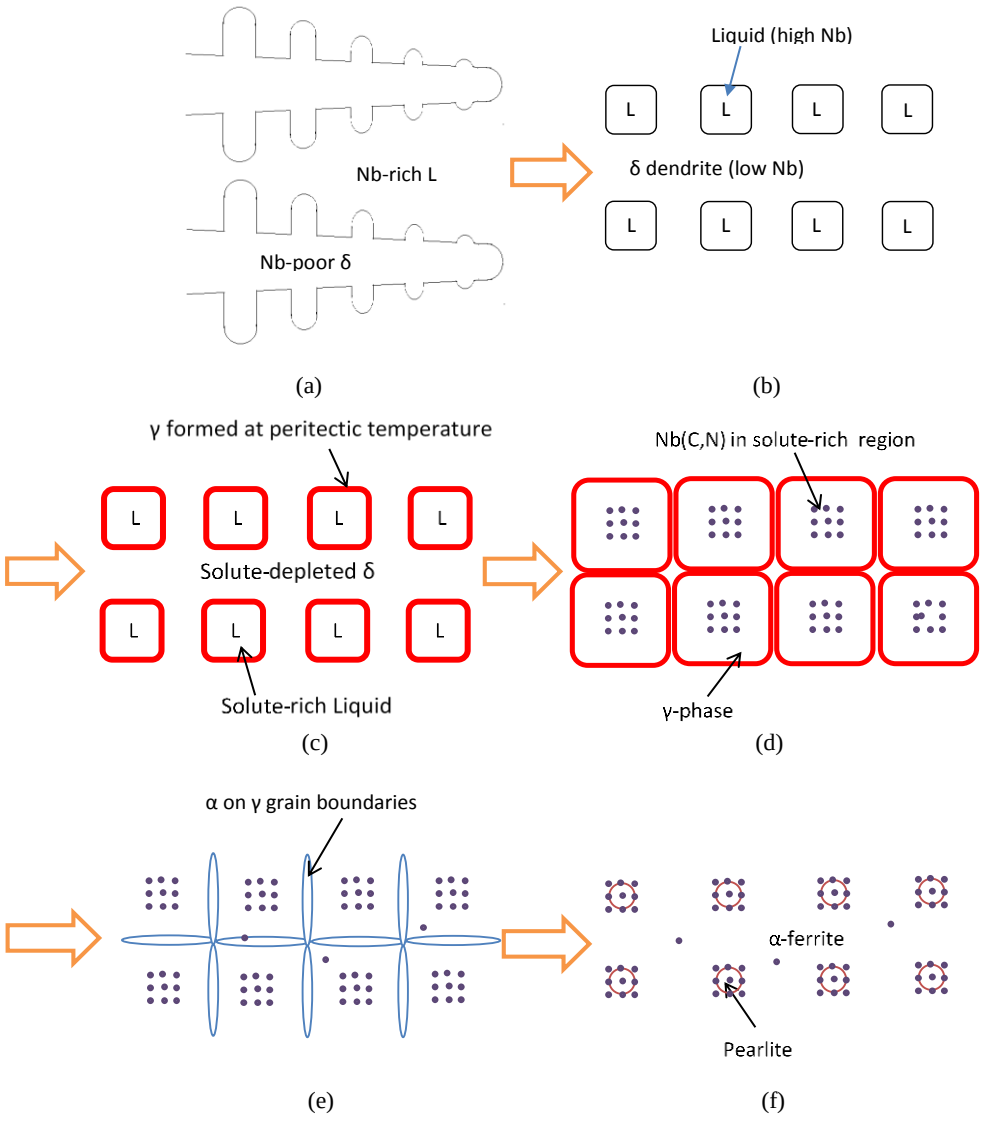

Figure 7-4 Schematic diagram of phase transformations and microsegregation processes during casting at quarter thickness of continuously cast steel slab.

7.2 Mathematical modelling of solidification under non-equilibrium conditions by analytical approaches

The continuous casting process is carried out under certain cooling rates differing from the equilibrium conditions assumed by Thermo-Calc (Thermo-Calc). So analytical approaches under non-equilibrium conditions have been applied to simulate the microsegregation in low carbon microalloyed continuously cast steel slabs.

7.2.1 Assumptions

For non-equilibrium modelling, most models are simplified to consider one-dimensional elemental diffusion normal to the solid-liquid interface; this is not a major limitation as usually diffusion can be expanded to two and three dimensions by geometrical factors. The range of analytical solutions can be represented by Scheil and Clyne-Kurz as shown in section 4.2 [22, 124]; for these there are a number of common assumptions:

i. Equilibrium is assumed to hold at the δ/ L and γ/L interfaces.
ii. The partition coefficients of elements at the δ/L and γ/L interfaces are assumed constant.

In addition to these common ones, Clyne-Kurz model has more assumptions listed below:

i. The cooling rate is constant during solidification;
ii. The alloying element diffusion coefficients are constant in each phase during solidification;

7.2.2 Mathematical formulation with multi-component effects

In this study, multiple-components (C, Si, Mn, P, S) were taken into account in analytical approaches to predict the solute-rich fractions and microsegregation profiles as shown in section 4.2 and other microalloying elements are assumed to have no effect on the liquidus temperature due to the low amounts in which they are present. The Scheil equation has been rewritten to take into account the multiple-component effects by combining Equation 4-8 and 4-15 shown below:

$$T_{int} = T_f - \sum_i m_i \cdot C_{0,i}(1 - f_S)^{(k_i - 1)} \quad 7\text{-}1$$

Similarly, the Clyne-Kurz equation for multiple-components was obtained by imputing Equation 4-10 into Equation 4-15 as follows:

$$T_{int} = T_f - \sum_i m_i \cdot C_{0,i}[1 + f_S(\beta_i k_i - 1)]^{(1-k_i)/(\beta_i k_i - 1)} \quad 7\text{-}2$$

Above the peritectic temperature, δ-ferrite grows into the liquid, so the relationship between element concentration at the δ/L interface in δ-ferrite and solid fraction is as expressed below:

$$C_S^* = k_i^{\delta/L} C_{0,i} \left[1 + f_S(\beta_i^\delta k_i^{\delta/L} - 1)\right]^{(1-k_i^{\delta/L})/(\beta_i^\delta k_i^{\delta/L} - 1)} \quad 7\text{-}3$$

Where $k_i^{\delta/L}$ is the partition coefficient of element *i* at δ/L interface, β_i^δ is β value in δ-ferrite and calculated by Equation 4-12.

7.2.3 Parameters

The cooling rate C_R was calculated using the Equation 3-1 based on SDAS values except for the pipeline steel as was explained in section 6.1 listed in Table 7-2. The liquidus, solidus and peritectic temperatures and equilibrium partition coefficients of the main solute elements were predicted by Thermo-Calc software and are shown in section 7.1 . The diffusion coefficient equation for solute elements in δ-ferrite (D_S^δ) and γ-austenite (D_S^γ) phase (Table 3-1) was used

to calculate the diffusivity for the present study [80]. For the steel solidifying through the peritectic reaction, the average of liquidus and peritectic temperature was used as the temperature value in the diffusivity equation for δ-ferrite. For steels solidifying as single phase δ-ferrite, the diffusivity was calculated at the average temperature of liquidus and solidus. The range of C and Mn diffusivities between the temperature extremes are within ± 4 - 5 % and ± 10 - 14 % of the values respectively calculated in the way above using the average temperature, so this approximation is considered acceptable. The (D_S^{δ}) and (D_S^{γ}) values of various elements were calculated in this way and used for modelling the different steels.

Table 7-2 Cooling rate of Structural, Ship building and Slab1 steels and modelling parameters predicted by Thermo-Calc software.

Steel	Pipeline	Structural	Slab 1	Ship building
Cooling rate (°C/s)	0.80	0.81	0.13	0.57
ΔT_S (°C)	30	41	48	51
t_f (s)	38	51	369	89

Table 7-3 lists the (D_S^{δ}) and (D_S^{γ}) values of different elements used in the slab 1 steel. Carbon diffusion in δ-ferrite is at least one order of magnitude faster than that of any of the other alloying elements. In γ phase, the carbon atom still moves the fastest among all elements. The diffusivities of substitutional elements in γ-phase are at least 2 orders of magnitude lower than those in δ-ferrite, especially Nb and Cr (3 orders of magnitude lower). The liquidus line slope values m [125]used in Equations 7-1 and 7-2 are listed in Table 7-4.

.For the constant cooling rate assumed in the present work, the local solidification time (t_f) simplifies to

$$t_f = \frac{\Delta T_s}{C_R} \qquad 7\text{-}4$$

where ΔT_S is the solidification temperature range, $\Delta T_S = T_L - T_S$ listed in Table 7-2. Solidus and liquidus temperatures were assumed to be unaffected by cooling rate.

Table 7-3 The diffusivity values of different alloying elements in δ-ferrite and γ-austenite phases for slab 1 steel used in Clyne-Kurz model.

Elements	C	Si	Mn	P	S	V	Nb	Cr	Ti	Ni
D_S^{δ}(μm/s)	5.10E+00	3.74E-02	1.87E-02	4.86E-02	2.18E-01	4.12E-02	1.90E-01	2.09E-02	1.61E-02	1.37E-02
D_S^{γ}(μm/s)	7.39E-01	9.36E-04	1.98E-04	3.49E-03	5.14E-02	5.28E-04	9.22E-04	3.49E-05	4.84E-04	1.27E-04

Table 7-4 Liquidus line slopes of solute elements.

Element	C	Si	Mn	P	S
m(℃/pct)	78.0	7.6	4.9	34.4	38

7.3 Comparison of experimental and predicted results

7.3.1 Solute-rich fractions

According to section 7.1.3 , the fraction of solute rich liquid at the peritectic temperature is essential to the formation of microsegregation. Because diffusion in austenite is much slower than diffusion in δ phase, very few substitutional alloying element atoms were assumed to be transported through the austenite layer in these simulations [94, 126]. Due to the high diffusivity of carbon atoms in this temperature range both in δ-ferrite and γ-phase, there is

little undercooling from the equilibrium temperature for the peritectic reaction [85, 127]. So the peritectic temperatures predicted by Thermo-Calc software were used in Clyne-Kurz and Scheil models. The fraction of δ ferrite as a function of temperature is simulated using Equation 7-1 and 7-2 in order to determine liquid fraction at the peritectic temperature.

Table 7-5 Comparison of experimental solute rich fraction (%) with the prediction of Scheil, Clyne-Kurz, Thermo-Calc.

Solute rich fractions	Slab 1	Ship building	Structural	Pipeline
Experimental	10-17	12-20	3	0
Scheil	20	25	0	0
Clyne-Kurz	11	18	0	0
Thermo-Calc	16	20	0	0

The solute-rich fractions predicted by the Scheil model (Equation 7-1), Clyne-Kurz model (Equation 7-2) and Thermo-Calc software are listed in Table 7-5. Compared with experimental solute-rich fractions, Clyne-Kurz and Thermo-Calc predictions fitted better than the Scheil model. The Scheil model which assumes no alloying element back-diffusion in the solid due to a fast cooling rate is not suitable for the case of these continuously cast steels.

7.3.2 Composition profiles

The elemental concentrations in the first solid and the last liquid are usually used to predict the element segregation range. Normalised Mn contents in the first solid and the last liquid were predicted by Thermo-Calc, Clyne-Kurz (Equation 7-3 and 7-4) and Scheil models (Equation 4-8) shown in Table 7-6. The predicted normalised Mn concentrations in the first solid determined by the partition coefficients $k^{\delta/L}$ are similar. The normalised Mn content in

the last liquid predicted by Clyne-Kurz is intermediate between the values predicted by Thermo-Calc and the Scheil model. Although all the predictions overestimate the experimental segregation extent (0.75 - 1.2) in structural steel, Thermo-Calc prediction fits the experimental results better.

Table 7-6 Predicted normalised Mn content in the first solid and the last liquid in structural steel.

	Thermo-Calc	Clyne-Kurz	Scheil	Experimental
First solid	0.71	0.68	0.68	0.75
Last liquid	1.50	1.81	4.24	1.2

The composition profile (composition as a function of solid fraction) at the peritectic temperature for ship building and slab 1 steel and solidus temperature for pipeline and structural steel need to be predicted by different models based on the hypothesis presented in section 7.1.3 to compare with the experimental composition profile obtained at room temperature. The composition in solid and liquid phases at the peritectic or solidus temperature were predicted by Thermo-Calc and the Scheil model (Equation 4-8), while only the interfacial composition in solid and liquid as a function of solid fraction at different temperatures can be predicted by Clyne-Kurz using equations 7-3 and 7-4 and the compositions at the previous interfaces can change as the interface moves due to back-diffusion. In order to compare with experimental results, the interface composition corresponding to a certain solid fraction and temperature is assumed to be unchanged during the rest of solidification. The interface composition in the solid and composition in the remaining liquid at peritectic temperature or interface composition in the solid at solidus temperature predicted by Clyne-Kurz model is assumed to represent the composition profiles against solid fraction at the peritectic temperature or solidus temperature.

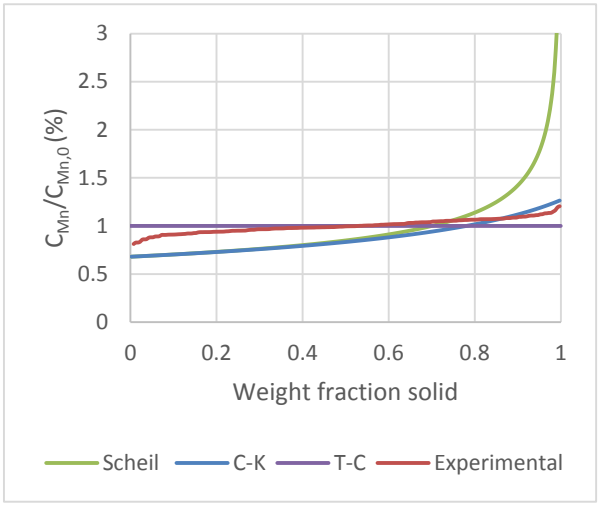

(a)

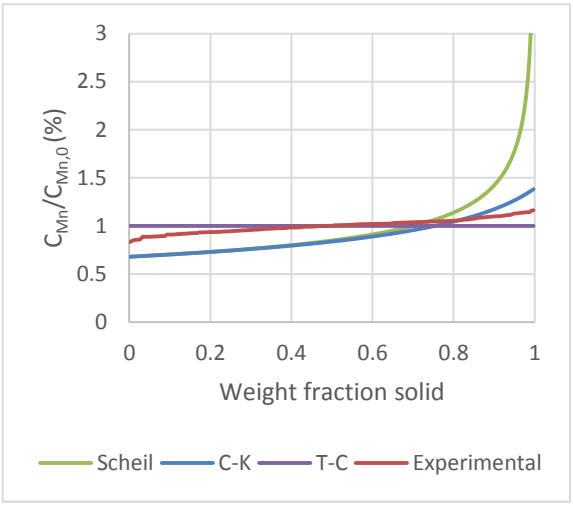

(b)

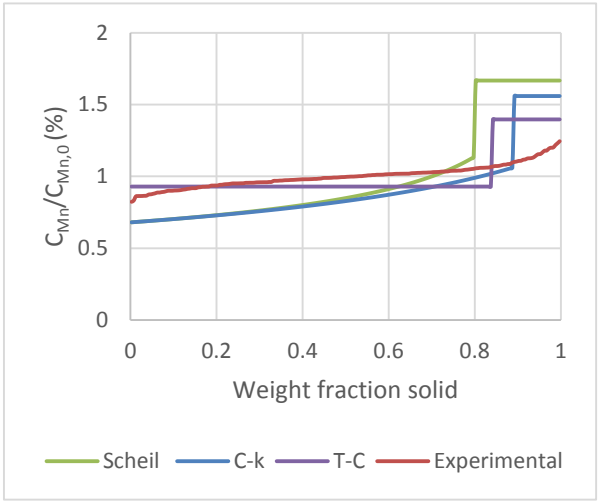

(c)

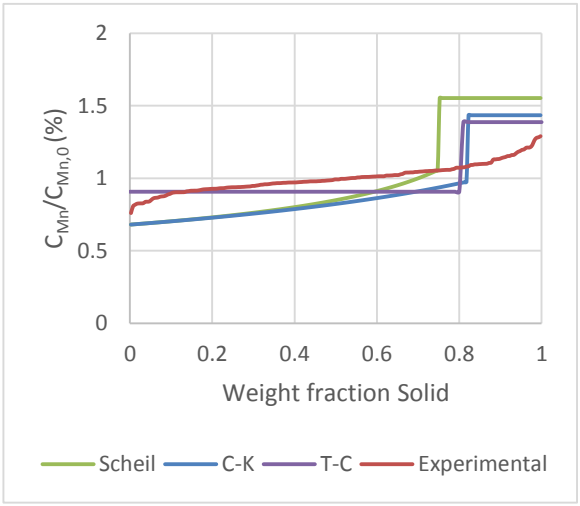

(d)

Figure 7-5 Normalised Mn composition profiles in δ-ferrite at solidus temperature in (a) structural and (b) pipeline steel and through solid and liquid at peritectic temperature in (c) slab 1 and (d) ship building steel as a function of solid fraction predicted by Scheil, Thermo-Calc and Clyne-Kurz models and experimental normalised Mn concentration profiles.

Figure 7-5 shows the comparison of normalised Mn concentration against solid fraction predicted by Thermo-Calc, Clyne-Kurz and Scheil methods at the solidus temperature in structural and pipeline steels and at the peritectic temperature in ship building and slab 1 steels. For the structural and pipeline steels without peritectic reaction, the Thermo-Calc prediction shows no segregation in the solid and the Clyne-Kurz prediction in the right part of

the profile agrees with the experimental profile better than the Scheil model. Also because the interface composition assumption was adopted by the Clyne-Kurz model, the mean composition is not 1. The finite difference solution can be used to obtain composition profiles at the peritectic temperature or solidus with unity mean composition. Also, post-solidification processes may need to be considered to allow more alloying element atoms to diffuse from the interdendritic region (right hand side) to the centre of dendrite arm (left hand side) to improve the prediction. In ship building and slab 1 steels, the liquid composition predicted by Clyne-Kurz is based on the interface composition at peritectic temperature and is not affected by the interface composition assumption. All the predictions for liquid (solute-rich region) composition are above the experimental profiles although Thermo-Calc and Clyne-Kurz prediction are closer to experimental results than the Scheil method. These indicate that more alloying element diffusion from solute-rich to solute-depleted regions after peritectic reaction needs to be invoked. Therefore a finite difference method taking into account processes after the peritectic reaction needs to be applied to improve microsegregation prediction.

7.4 Conclusion

The phase transformations during casting for all four steels have been predicted by Thermo-Calc. The slab 1 and ship building steels were predicted to solidify via a peritectic reaction, while the structural steel and pipeline steel should solidify fully as δ phase before austenite forms. In addition, carbides, nitrides or carbo-nitrides of Ti, Nb, V and Al were predicted to precipitate in low carbon microalloyed steels. The partition coefficients of the solute elements during solidification were predicted by Thermo-Calc and decreased with decreasing temperature and varied with composition. The average partition coefficients were used in analytical approaches. Nb and Ti were expected to exhibit severe microsegregation into the liquid phase during solidification. The formation of austenite at the interface of δ/L was

assumed to trap the enriched elements in the liquid. The remaining liquid fraction was used to predict the solute-rich fraction.

The Scheil, Clyne-Kurz and Thermo-Calc models were used to predict the solute-rich fraction and Mn concentration profiles with solid fraction at peritectic or solidus temperature. The Clyne-Kurz and Thermo-Calc models gave a reasonable agreement of solute-rich fractions with experimental results. The Clyne-Kurz model gave better prediction of segregation profiles than the other two methods when compared with experimental results. A finite difference method considering processes after the peritectic reaction may improve the modelling results.

Chapter 8 DICTRA prediction of segregation in low carbon continuously cast steel

DICTRA is a useful tool for predicting diffusion-controlled phase transformation in multi-component alloy systems incorporating both thermodynamic and kinetic databases. Compared with the analytical approaches used previously, the advantages of DICTRA (numerical model) are summarised below:

1. In the Clyne-Kurz and Scheil models, cross-elemental effects are neglected, although the diffusion of one element in a phase is affected by other elements existing in the matrix at the same time which is taken into account in DICTRA [112];
2. The partition coefficient, k, used at the interface in DICTRA was extracted from the thermodynamic database and so changed with temperature and composition rather than being constant as assumed in the analytical approaches;
3. Due to the richness of thermodynamic and kinetic databases, diffusion-controlled phase transformations during cooling in the solid-state and homogenisation could be dealt with, whereas the Clyne-Kurz and Scheil models are only able to simulate the process of solidification.
4. In the Clyne-Kurz model, only the interface composition in solid and liquid can be obtained with temperature, while DICTRA uses finite-difference methods to give full detailed simulation results as a function of both time and position.
5. In analytical approaches, complete mixing in liquid is assumed, but in DICTRA, the diffusion of elements in liquid are calculated based on the mobility database.

8.1 DICTRA input parameters

8.1.1 Time step ∂t and grid spacing ∂x in DICTRA

Grid distribution or grid spacing ∂x and time step ∂t were important to run the simulation successfully. In numerical modelling the stability and convergence of a solution can be strongly dependent on the ratio of $\frac{D\delta t}{\delta x^2}$ (diffusion number) [128], where D is the diffusivity of each element in a specific phase. If the ratio is over 0.5, the numerical method is unstable and the fluctuation in the concentration profile may appear to lead to a failure of the simulation. Due to the unknown diffusivity in DICTRA, the acceptable stability range for the ratio of $\frac{\delta t}{\delta x^2}$ is unknown as well.

∂t can be controlled by limiting the maximum of the time step (Max (∂t)) used in DICTRA. Generally, the smaller the values of ∂x and ∂t used in DICTRA are, the more accurate is the prediction, however, the longer the simulation time is. The proper choice of ∂x and ∂t should not only give relatively accurate predictive results but also reduce the simulation time to make the model more efficient. Therefore, for low carbon steel, the proper ∂x and ∂t ranges which can give smooth and steady curves in a simulation in a more efficient way were investigated.

According to the different phase transformation types, the whole casting process can be divided into 4 stages: solidification stage, single phase (austenite) stage, proeutectoid and eutectoid stage. The single phase cooling stage is not involved with phase transformation and so, compared to the others, larger ∂x and ∂t can be accepted to still give reasonable results. During the eutectoid stage, a complex pearlite phase consisting of alternate layers of α-ferrite and cementite is formed. Due to the low temperature at which the eutectoid reaction proceeds the overall concentration profiles of substitutional elements were assumed to not change

during the eutectoid reaction. Hence, the solidification and proeutectoid stages were the main investigated objects of this section.

8.1.1.1 Proeutectoid temperature range

The simulation conditions which were used to investigate the effect of varied ∂x and ∂t on the proeutectoid process are described below. The chemical composition used in this simulation is listed in Table 8-1. The cooling rate was 0.025 K/s. There were two phases existing, α-ferrite (bcc) and austenite (fcc). The total simulation time was 2000 s and the overall distance (half of SDAS) was assumed to be 110 μm.

Table 8-1 The chemical composition of Slab 1 used in DICTRA simulation (wt %).

Elements	C	Mn	Si
Slab 1	0.1	0.31	1.42

The effect of ∂x on the diffusion-controlled proeutectoid process of this steel was investigated first. The types of grid point distribution can be specified as linear, geometric and double geometric. Linear grid distribution with same spacing between adjacent grid points was applied as a starting point. Keeping Max (∂t) =10 s constant and changing ∂x from 0.1 μm to 1 μm, the running times were similar, about 12 minutes, indicating that the grid spacing has little effect on the diffusion calculation. At the beginning of the simulation, only the austenite phase existed in a cell. With simulation proceeding, α-ferrite forms at the left hand side of the cell and there is one interface between austenite and α-ferrite. After simulation, the composition profiles and grid point spacing ∂x in different phases against distance from the centre of the dendrite and the position of interface as a function of time can be obtained.

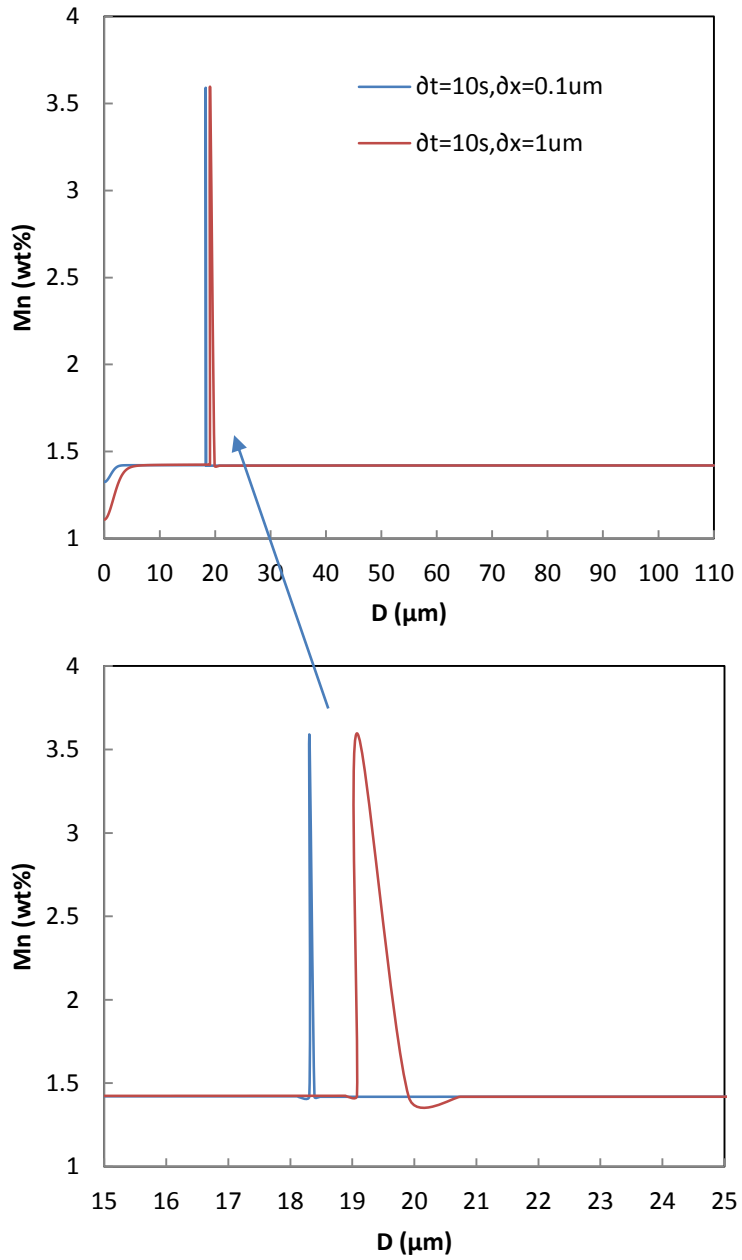

Figure 8-1 The Mn content as a function of distance at 2000s with Max (∂t) =10s and ∂x =0.1μm and 1μm.

Figure 8-1 shows the composition profiles at 2000 s with different ∂x of 0.1 and 1 μm. The initial parts of Mn distribution profiles against distance and the width of the peaks at the interface of bcc and fcc are different with varied ∂x. The α-ferrite forms and grows from the

left hand side towards the right hand side. The solute rejected from bcc at the interface with austenite formed a narrow peak which diffused more back into the bcc to keep the mass conserved (the material in the bcc state has much higher diffusivity than when in fcc), so the Mn content in the very left part of the profile with 0.1µm ∂x is higher than that with 1µm ∂x. Also, the smaller width of interface peak slows down the moving velocity of the interface due to longer time back diffusion so that a difference in the position of the Mn peak as ∂x changes was shown in Figure 8-1. In a real situation, the material should be continuous and the peak width should be controlled by the diffusion and cooling conditions, so ∂x=0.1µm was recommended. The variation in ∂x did not affect the overall composition profile except the initial part which accounts for less than 1 % of the whole length. If a smaller ∂x was applied, the maximum of ∂t will be limited as well. So the combination of ∂x and ∂t need to be considered together.

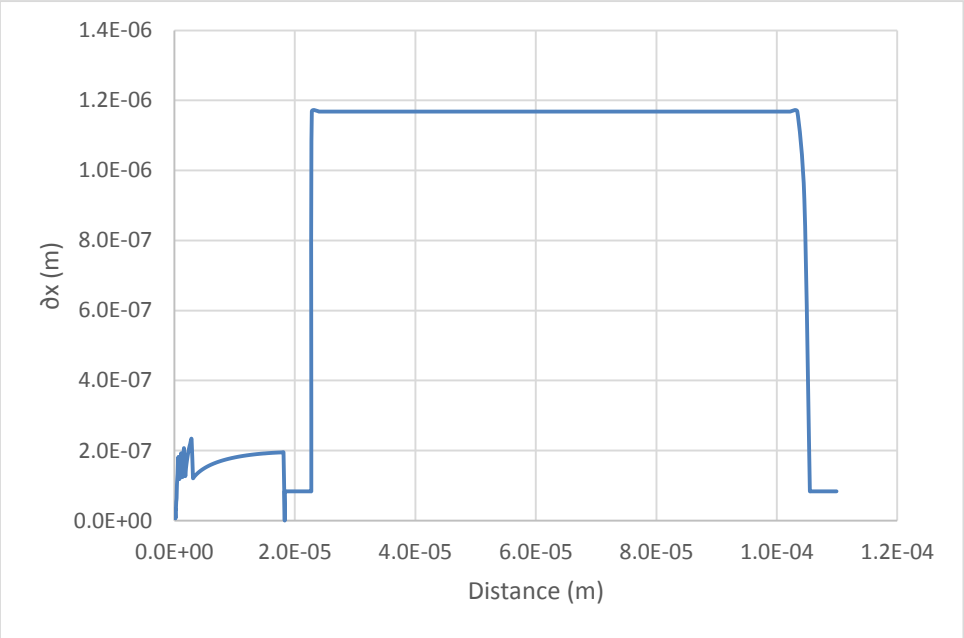

Figure 8-2 Grid point spacing ∂x as a function of distance at 2000 s of simulation with initial set up of ∂x=0.1 µm and Max (∂t) =10 s.

The ∂x distribution along the distance changed with the phase transformation process. Figure 8-2 shows the grid spacing ∂x calculated from the positions of grid points in simulation results as a function of distance with ∂x=0.1 μm when the interface of α-ferrite and austenite was around 20 μm. On the very left hand side, the ∂x is very small about 0.02 μm, so an unstable fluctuation in element profile (in Figure 8-3) occurred when Max (∂t) which controls the time step ∂t in DICTRA is bigger than 10 s. During the proeutectoid reaction, the time step started with a small time step of 1e-7 s by default and increased until the Max (∂t) controlled automatically by the software. When Max (∂t) ≤10 s along with ∂*x*=0.1 μm, a stable smooth concentration profile can be obtained for the proeutectoid stage. Figure 8-4 shows that the concentration profile against distance is independent of ∂t as this varied from 1 s to 10 s. The running time increased from 12 minutes to more than 1 hour when the Max (∂*t*) decreased from 10 s to 1 s. Therefore in order to reduce running time, the Max (∂t) = 10 s was chosen for the simulation of the proeutectoid process.

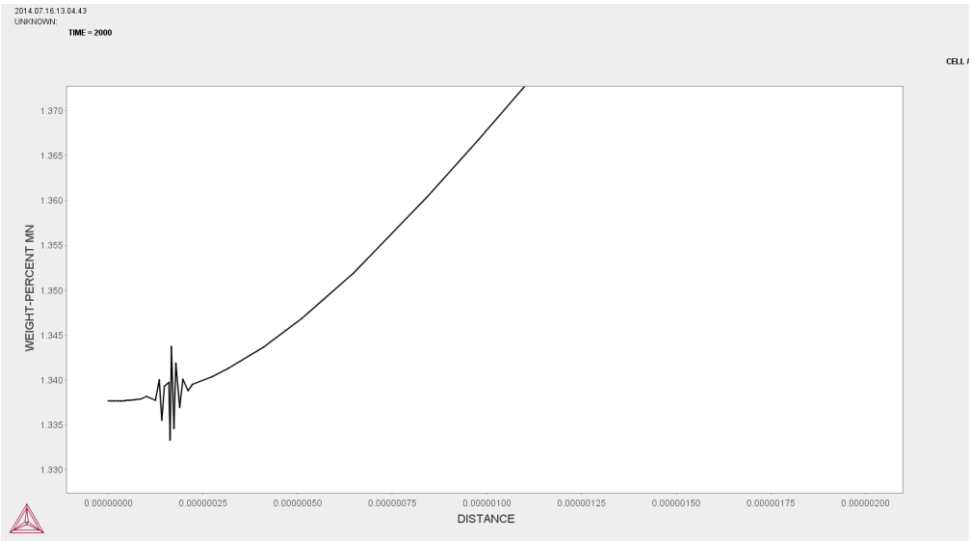

Figure 8-3 Fluctuation in the Mn profile against distance.

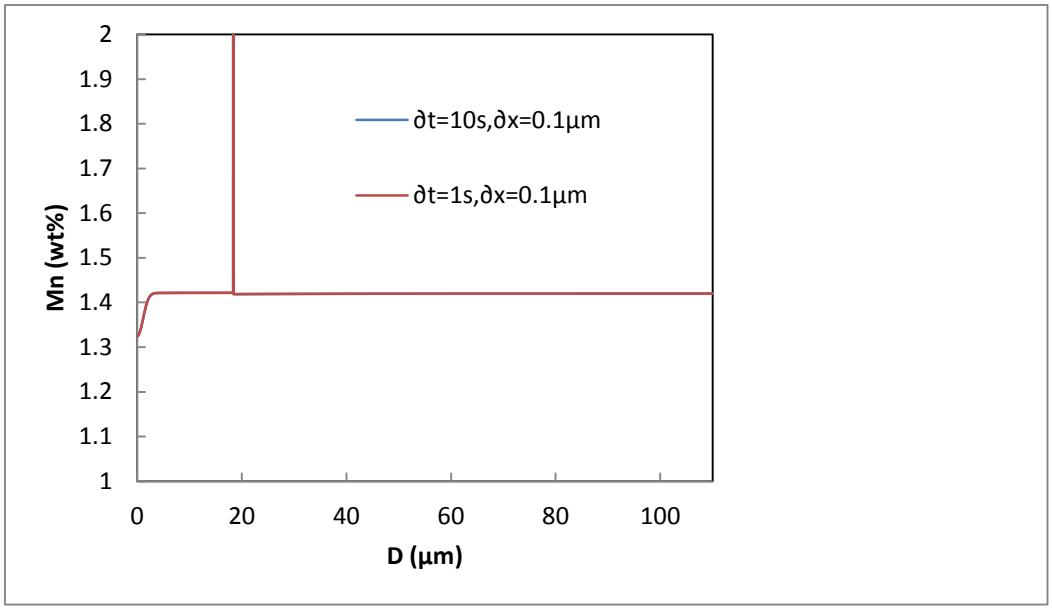

Figure 8-4 Mn concentration as a function of distance for different ∂t.

8.1.1.2 Solidification process

There is no sharp composition peak near the interfaces during the solidification process due to the fast diffusion of elements in both solid and liquid, so the larger values for ∂t and ∂x can be used. Simulation conditions were determined for the solidification stage as described below. Chemical composition was the same as that used for the proeutectoid process shown in Table 8-1. Cooling rate used during solidification was 0.18 ℃/s near the solidification rate of slab 1 steel. The linear geometric grid point distribution was applied. Max (∂t) and ∂x were investigated in the range from 10 s -100 s and 0.1-1 µm.

From Figure 8-5, varying ∂x from 0.1 µm to 1 µm has no effect on Mn diffusion during the solidification process as predicted by DICTRA. Therefore, 1 µm ∂x was chosen for use as ∂x through the solidification stage.

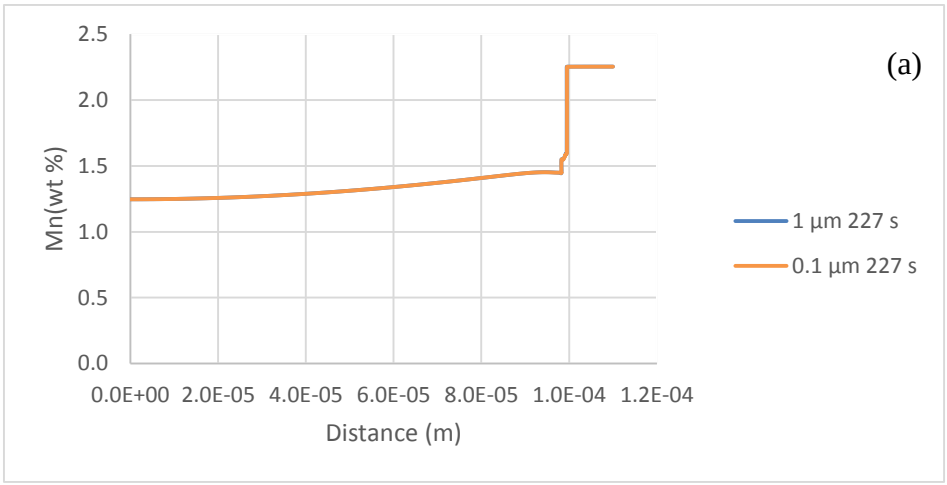

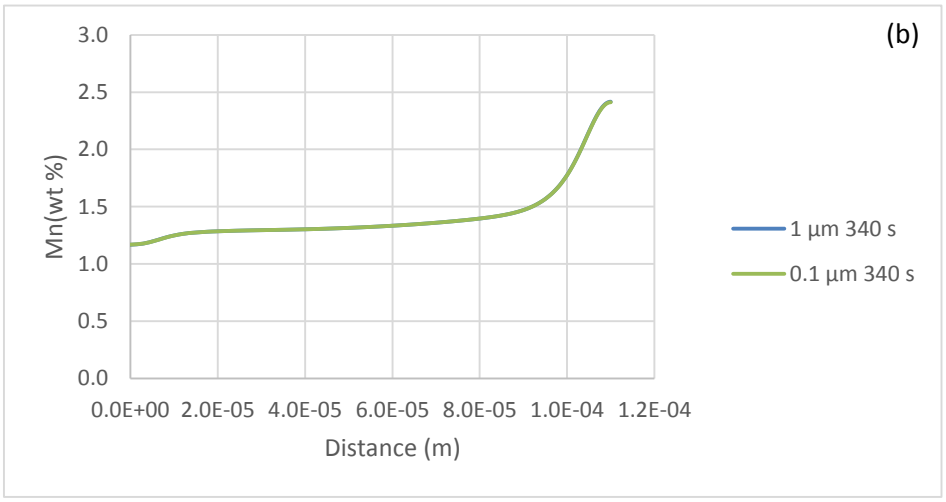

Figure 8-5 Mn weight percentage as a function of distance at different ∂x and different time (a) 227 s and (b) 340 s for slab 1 steel with C, Si and Mn.

During simulation of solidification, the time steps automatically set by DICTRA were mostly less than 10 s, so there was almost no difference in output for Max (∂t) values between 10 s and 100 s. Solidification simulation using values of Max (∂t) = 100 s and ∂x = 1 µm proceeded without fluctuation, Figure 8-6, and so this was incorporated with the single austenite phase stage for simulation using DICTRA, with a consistent set of parameters of Max (∂t) = 100 s and ∂x = 1 µm. When simulating the three stages (solidification,

single austenite phase and proeutectoid stages) together, a set of Max (∂t) = 10 s and ∂x = 0.1 μm was used in order to run through all the stages successfully.

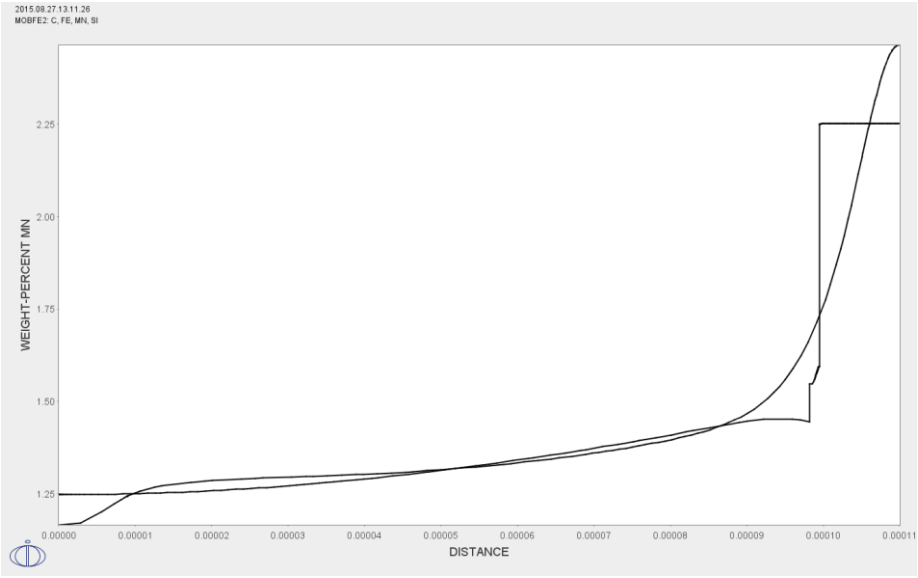

Figure 8-6 Mn profile against distance (m) from centre of the dendrite for slab 1 steel with Max (∂t) = 100 s and ∂x = 1 μm at 227 s and 330 s.

8.1.2 Cooling rate prediction

The cooling rate is an important parameter for DICTRA prediction. The whole cooling process at quarter thickness of steel was divided into two stages: water cooling (secondary cooling) and air cooling stages. The cooling rate during water cooling process was assumed to be constant and the same as the solidification rate predicted by Equation 3-1, i.e. varying from 0.13 to 0.81 K/s which were also used in the analytical approaches. The temperature at which the secondary cooling process finished at quarter thickness of slab was assumed to be 1250 ℃ which is in the middle of the average temperature range reported in section 2.2.2 [15, 129]. Cooling rate during air cooling was predicted by a 1 D heat transfer model using a Matlab calculation described below.

8.1.2.1 Numerical modelling of air cooling rate by Matlab

A numerical model of heat transfer, using Matlab designed by Jason Swan (PhD student from School of Metallurgy and Materials, University of Birmingham) for an air cooling process has been adopted and adapted to predict the cooling rate in radiative cooling during the continuous casting of steel. The mathematical model is as follows. The width of the slab is much greater than the thickness, in section 5.1 , so the heat transfer of the steel slab is simplified into one dimension along the thickness direction. The heat transfer is assumed symmetric along the thickness direction. Therefore the half thickness of the steel slab was investigated with a thickness of n mm divided into n cells and the volume of each cell V is 1 mm^3: 1 mm long, 1 mm wide and 1 mm high. The simulation time is 180 minutes with time step dt of 0.5 s and ambient temperature of 20 ℃. It is hard to know the temperature distribution along the thickness direction when the radiative cooling process starts so that the average temperature through the thickness, 1250 ℃ is assumed to be the starting temperature neglecting the initial temperature gradient along the thickness direction. This assumption may affect the cooling rate at different thickness positions at the beginning of the process, while the surface temperature will drop quickly and be controlled by the heat taken off from the surface. In each cell, at each time step, the temperature T is the same, so the temperature dependent properties are uniform such as thermal conductivity C_n. The left hand side of the cell is assumed to be the centre of the slab and the surface on the right hand side is exposed to the air. Each cell is denoted as i and from left to right hand side, i increased from 1 to n.

The thermal conductivity for 0.5C-0.5Mn-0.25Si wt% steel was fitted into Equation 8-1 and applied to the steels in this study approximately:

$$\begin{matrix} k = -0.032T + 63.736,\ \ 800K\ \leq\ T < 1054\ K \\ k = 30,\ \ 1054K \leq T < 1273K \end{matrix} \qquad 8\text{-}1$$

Where *k* is thermal conductivity, W m^{-1} K^{-1}

Heat transfer coefficient for mild steel from surface to air is about 7.9 W/ (m^2·K) and emissivity coefficient for steel with an oxidised surface is approximately 0.79, which were chosen to be used in this modelling. The densities of steel were calculated by Thermo-Calc software.

$$dH = \delta Q = C_p dT \tag{8-2}$$

provided that the system is under constant pressure (dP = 0) and that the only work done by the system is expansion work (δW ' = 0). δQ is a small amount of heat added to the system, C_p is the heat capacity at constant pressure. It means H is only dependent on temperature. Enthalpy H in the system, as a function of temperature, was obtained from Thermo-Calc calculations for each composition.

The thermal resistance of right half of cell i-1 which contacted the left interface of cell i is

$$R_{i-1}^{r} = \frac{0.5dx}{k_{i-1}} \tag{8-3}$$

The thermal resistance of left half cell i which contacted the left interface of cell i is

$$R_{i}^{l} = \frac{0.5dx}{k_{i}} \tag{8-4}$$

Where *k* is heat transfer coefficient.

So the heat transferred into cell i through the left interface is

$$p_{i,j}^{l} = (T_{i-1,j} - T_{i,j}) \cdot A/(R_{i-1}^{r} + R_{i}^{l}) \tag{8-5}$$

So in the same way, the heat transfer out of cell i through the right interface is

$$p_{i,j}^{r} = (T_{i} - T_{i+1}) \cdot A/(R_{i}^{r} + R_{i+1}^{l}) \tag{8-6}$$

Where j is denoted as time, *d*t, starting with 0, *A* is cross-sectional surface area.

When $2 \ll i \ll n-1$,

$$p_{i,j} = p_{i,j}^{l} - p_{i,j}^{r} \quad 8\text{-}7$$

Where $p_{i,j}$ is the energy change of cell i per time, J/s.

When $i = 1$,

$$p_{1,j} = -p_{1,j}^{r} \quad 8\text{-}8$$

There is no heat transfer at the left hand side of slab.

When $i = n$,

$$p_{n,j} = p_{n,j}^{l} - p_{n,j}^{out} \quad 8\text{-}9$$

$$p_{n,j}^{out} = p_{n,j}^{rout} + p_{n,j}^{cout} \quad 8\text{-}10$$

Where $p_{n,j}^{out}$ $p_{n,j}^{rout}$ and $p_{n,j}^{cout}$ are respectively the total energy loss, radiative energy loss and convective energy loss per unit time, J/s.

The energy $E_{i,j}$ stored in each cell can be calculated by the equation below through enthalpy H_n:

$$E_{i,j} = V_c \times \rho \times H_{i,j} \quad 8\text{-}11$$

$$H_{i,j} = H(T_{i,j}) \quad 8\text{-}12$$

Where ρ is the density of steel assumed constant, $H_{i,j}$ is the enthalpy of cell i at the temperature of $T_{i,j}$, J/g. After dt, the energy in cell i is

$$E_{i,j+1} = E_{i,j} + p_{i,j} \times dt \quad 8\text{-}13$$

$$H_{i,j+1} = \frac{E_{i,j+1}}{V_c \times \rho} \quad 8\text{-}14$$

The temperature in each cell at time of $(j+1)*d$t can be calculated by

$$T_{i,j+1} = T(H_{i,j+1}) \quad 8\text{-}15$$

So, by increasing j from 0 to 21600, when $T_{i,0} = 1250$ ℃, the temperature in all cells ($1 \ll i \ll n$)) at every time step can be obtained. The mathematical calculations were carried out in Matlab.

Taking the ship building steel as an example, half thickness of ship building steel is 110 mm divided into 110 cells. The enthalpy against temperature was predicted by Thermo-Calc and is shown in Figure 8-7. The average density of steel over the temperature range of 500 - 1250 ℃ predicted by Thermo-Calc is 7.554 g/cm^3.

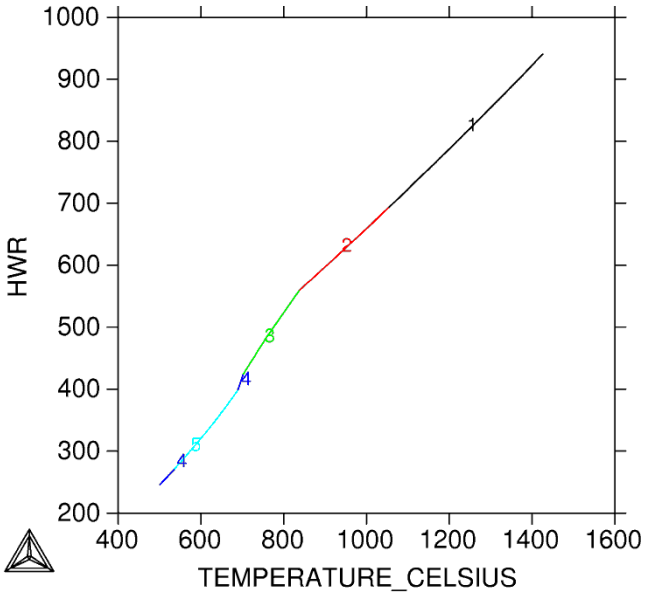

Figure 8-7 Enthalpy as a function of temperature predicted by Thermo-Calc for ship building steel

Using the Matlab code, the temperature at different thickness positions in the steel slab as a function of time was predicted. The temperature at quarter thickness was used and combined with the solidification rate to get the whole cooling process in Figure 8-8. The air cooling rates for 220 mm thick and 290 mm thick steel slab increased rapidly to maxima of 0.21 ℃/s and 0.17 ℃/s respectively at around 1200 ℃ and linearly reduces to 0.02 - 0.03 ℃/s at 600℃ with decreasing temperature. The simulation time was set as 6000 s for processes

from solidification to eutectoid and 2000 s for that from solidification to formation of precipitates.

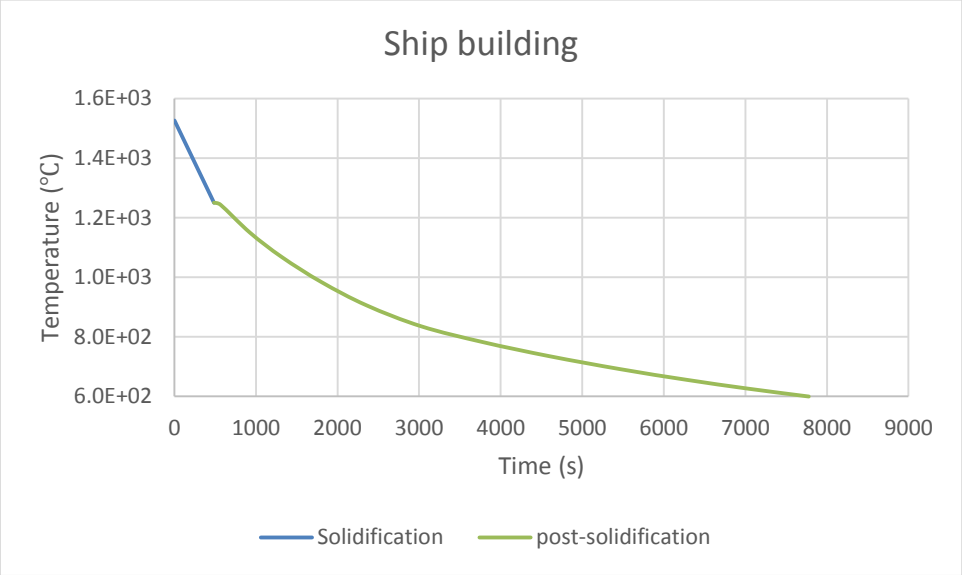

Figure 8-8 Predicted temperature as a function of time for the whole cooling process of ship building steel.

8.2 DICTRA predicted phase transformation and microsegregation development

In the steels studied, eutectoid and higher temperature phase transformations are controlled by diffusion and temperature. The microsegregation (the variation of element concentration along the direction from one dendrite centre to the adjacent one) arises from the solidification process, but is modified by the subsequent solid-state phase transformation. After inputting the parameters and simulation conditions, such as predicted temperature dependent on time and composition, into DICTRA, the diffusion-controlled phase transformation simulations were carried out through the whole temperature range. All the relevant information was stored in a dic file in which any results e.g. concentration as a function of distance in a cell and

velocity of interface movement can be extracted for analysis at any time. Solidification, cooling as a single austenite phase and γ-α transformation were analysed separately below.

8.2.1 Solidification process and single austenite stage

After running DICTRA for all investigated continuously cast steels, only the structural steel was predicted to have a different phase transformation process during solidification from the equilibrium Thermo-Calc prediction. According to the Thermo-Calc prediction in the previous chapter, structural steel should solidify as single δ phase before austenite forms with a 1 degree difference between the solidus and austenite forming temperatures, while in DICTRA, it solidified through the peritectic reaction at the very end of solidification. The difference can be explained by the segregation of elements in DICTRA which changed the local solidus temperature and austenite forming temperature. The ship building and pipeline grade steels were chosen as two typical examples representative of peritectic and non-peritectic steels to illustrate the phase transformation and segregation predicted by DICTRA.

Interstitial and substitutional alloying element distributions was investigated as a function of the distance along the dendrite centre - dendrite centre direction respectively because they have different diffusion mechanisms in steels and occupy different sub-lattices in the sub-regular Thermo-Calc (and DICTRA) used.

Figure 8-9 and Figure 8-10 show how the carbon concentration distributions in ship building steel (0.14C-0.38Si-1.35Mn) and pipeline steel (0.03C-0.25Si-1.7Mn) vary with distance from the centre of dendrite (on the left side) to the interdendritic region (on the right side) predicted by DICTRA and changed at different simulated times. The steps shown in each curve indicate the position of the interfaces between two adjacent phases due to partition of elements during the phase transformation. As was mentioned before, the thermodynamic data

from the thermodynamic databases were applied to the interfaces for each time step. The diffusion of the alloying element atoms in phases with time and temperature was calculated based on the kinetic databases.

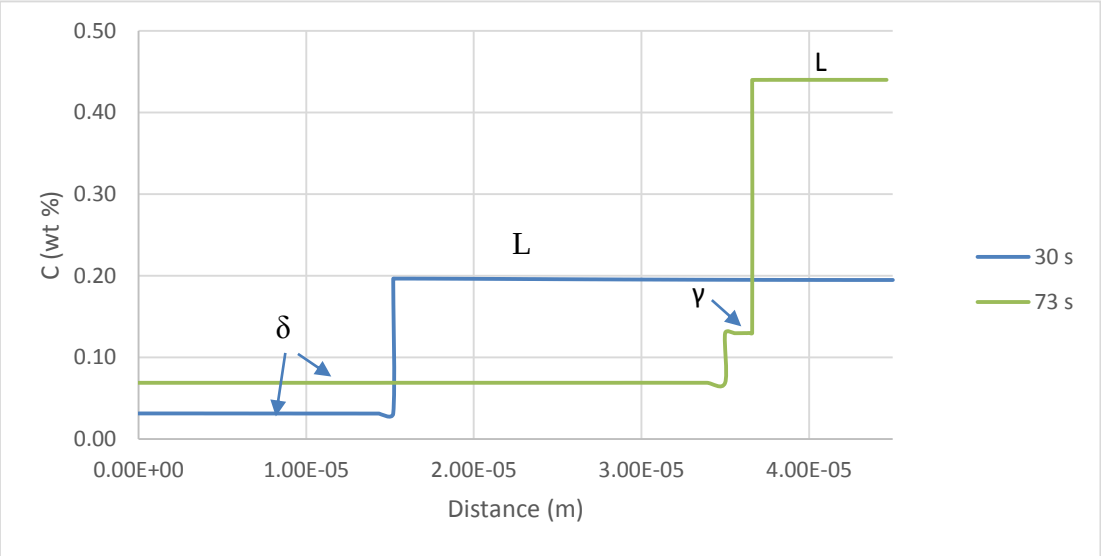

(a)

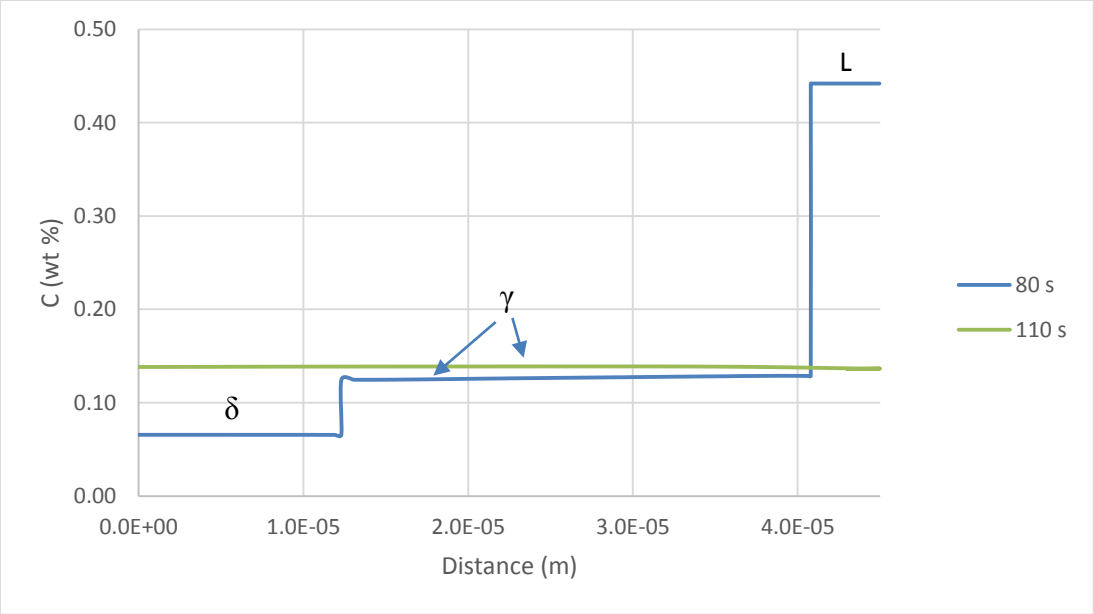

(b)

Figure 8-9 The C distribution along the distance from the centre of a dendrite to the middle point of two dendritic arms in ship building steel predicted by DICTRA at (a) 30 s, 73 s and (b) 80 s, 110 s corresponding to temperatures of 1510, 1485, 1481 and 1464 ℃.

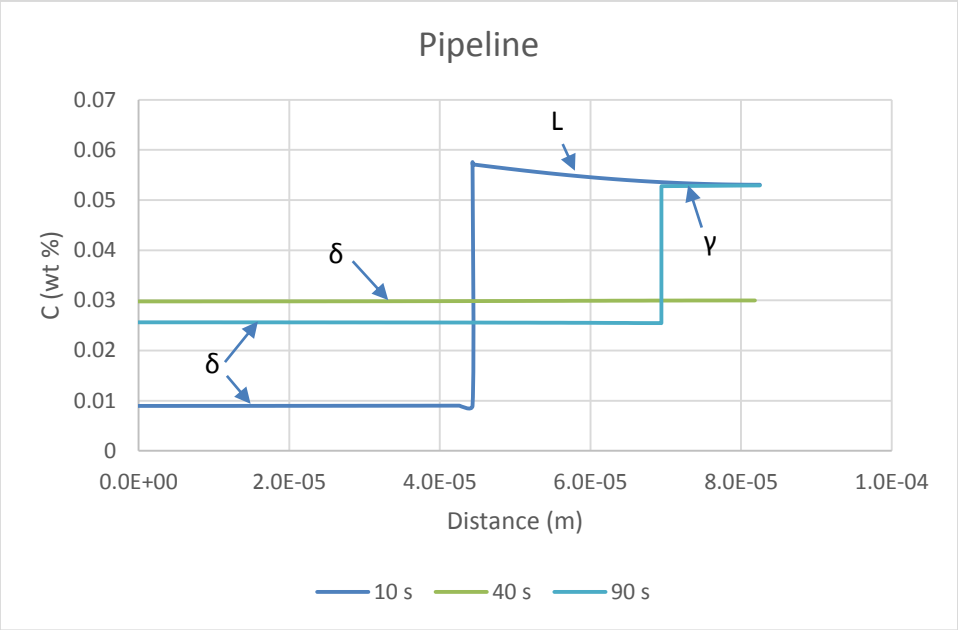

Figure 8-10 The C distribution along the distance from the centre of a dendrite to the middle point of two dendrite arms in pipeline steel predicted by DICTRA at 10 s, 40 s and 90 s corresponding to temperatures of 1519, 1495 and 1455 ℃.

At the beginning of the simulation, only liquid existed with a uniform concentration throughout the entire cell. On cooling, δ-ferrite formed on the left hand side of the simulation cell and grew into liquid towards the right hand side. Carbon partitions into the liquid, so the carbon content in δ-ferrite is lower than that in liquid shown in Figure 8-9(a). For the ship building steel, the peritectic temperature is reached after 73 s, when austenite (γ) with carbon content between those in liquid and δ-ferrite formed at the δ/L interface shown in Figure 8-9(a). As time passed, the γ-phase grew into both δ-ferrite on the left and liquid on the right shown in Figure 8-9(b). At 110 s, the γ-phase replaced δ-ferrite and liquid fully. For pipeline steel with lower carbon content, δ-ferrite grew into the liquid until the liquid disappeared and single phase δ-ferrite with a nearly uniform C content existed until the γ-phase formed on the right hand side of the cell and grew to replace the δ-ferrite. The carbon content stayed almost uniform in the austenite single phase in both steels indicating almost no carbon

microsegregation in single phase austenite after solidification. For the Clyne-Kurz model, due to the high diffusivity of carbon during solidification, β for carbon → 1, which changes the Clyne-Kurz model to the lever rule model and means the back-diffusion is fast enough to even out the segregation for carbon atoms. Therefore, there is no carbon microsegregation in δ-ferrite predicted by Clyne-Kurz or by DICTRA.

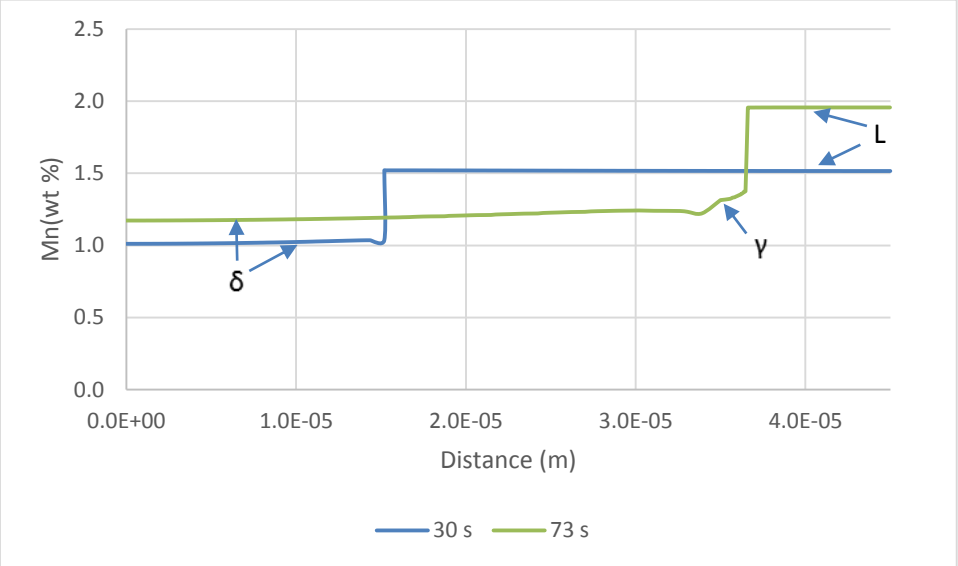

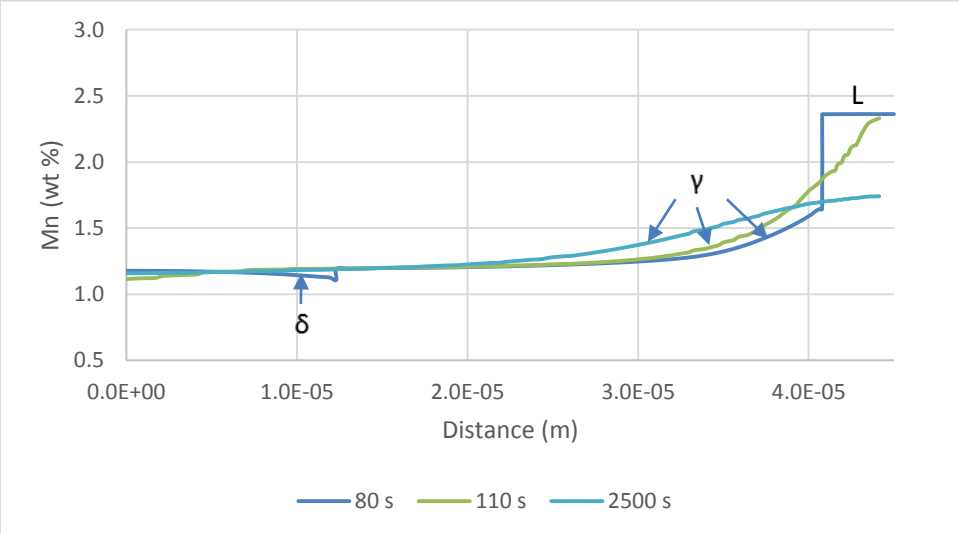

Figure 8-11 The Mn distribution against distance in ship building steel predicted by DICTRA at different times.

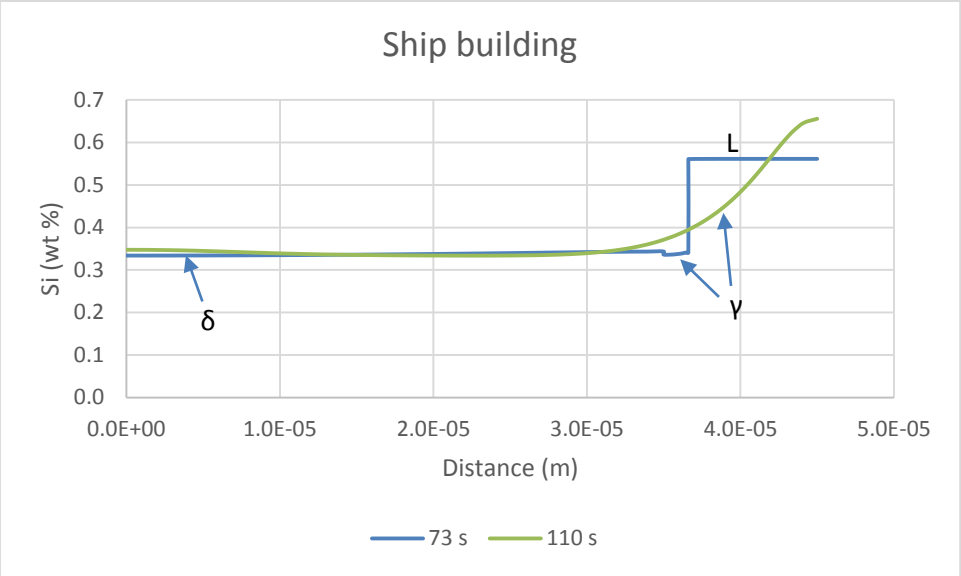

Figure 8-12 The Si distribution against distance in slab 1 steel predicted by DICTRA at 73 s and 110 s.

The substitutional alloying elements have different predicted segregation and diffusion behaviour from interstitial elements. The distributions of Mn (austenite stabiliser) in ship building steel and Si (ferrite stabiliser) in slab 1 steel against distance predicted by DICTRA are shown in Figure 8-11. There is little Mn segregation in δ-ferrite due to the high diffusivity of Mn in δ-ferrite. When austenite formed, due to the slower Mn diffusion in austenite, the Mn atoms in the last solidified liquid were trapped and contents stay higher than the left hand side of the profiles. As temperature decreased, homogenisation of Mn in single austenite phase occurs and the level of microsegregation decreased. As to the ferrite stabilising elements like Si, the Si was rejected from austenite to ferrite during the peritectic transformation. Therefore from left to right hand side, the Si content decreased slightly first and then increased, as shown in Figure 8-12.

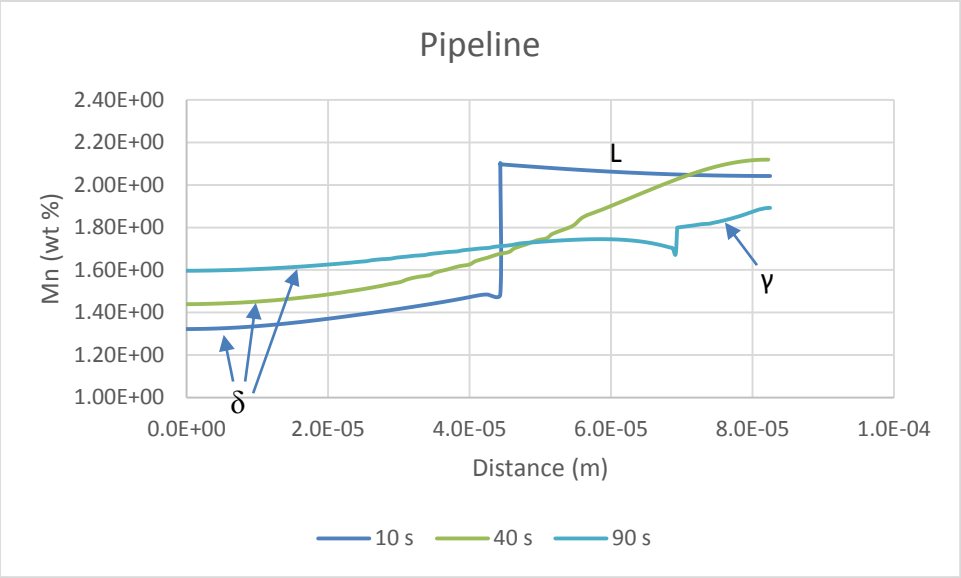

Figure 8-13 Mn distribution against distance in pipeline steel predicted by DICTRA at different times.

For the pipeline steel, there is no peritectic reaction during solidification, so the level of segregation for substitutional elements such as Mn is less severe. In Figure 8-13, the pipeline steel was predicted to be solidified as single phase δ-ferrite which was retained from 36 s to 82 s before austenite formed from the right hand side. The fast diffusion of alloying element atoms in the single δ-ferrite stage largely decreased the segregation as a function of distance in the cell (Figure 8-13).

8.2.2 Proeutectoid ferrite formation

At the end of the single γ-austenite phase stage, α-ferrite started to form and grew into γ-austenite phase (proeutectoid transformation) until the eutectoid reaction happened and the remaining γ-austenite phase was transformed to pearlite. The growth of ferrite has three major growth regimes: Partitioning, Local Equilibrium (or P-LE), Negligible Partitioning, Local Equilibrium (or NP-LE), and Para-equilibrium (ParaE) [43]. The P-LE and NP-LE regimes assume local equilibrium holds at the interface of α-ferrite and austenite, while ParaE assumes that only carbon partition between ferrite and austenite occurs whilst other substitutional

elements like Mn do not redistribute. The two assumptions for interfacial re-distribution were respectively applied to DICTRA for prediction of phase transformation of austenite to α-ferrite.

Figure 8-14 shows the C, Mn and Si concentration profiles at different times based on the local equilibrium assumption at the interface. Carbon (interstitial alloying element) gives an even concentration in α-ferrite phase and uneven concentration in austenite decreasing with distance from the interface. Mn, a substitutional alloying element, is rejected from α-ferrite to austenite as an austenite stabiliser. In contrast, Si as a ferrite stabiliser has the opposite partition direction to Mn.

In order to distinguish the ferrite growth mechanism, c_M^{AB} is defined as element M concentration in phase A at A/B interface. At the beginning of the α-ferrite-austenite transformation, $c_C^{\gamma\alpha} \rightarrow$ bulk composition $\overline{c}_c$ and $c_{Mn}^{\alpha\gamma}$ differs from $\overline{c}_{Mn}$, so ferrite grew by the P-LE mechanism according to section 2.4 . As time went by, the situation changed gradually: $c_{Mn}^{\alpha\gamma} \rightarrow \overline{c}_{Mn}$, so the mechanism for growth of ferrite switched to NP-LE according to its definition. In conclusion, the P-LE mechanism happened first until NP-LE takes over. Under P-LE mechanism, the initial part in the Mn profiles on the left hand side formed due to the partition of Mn between α-ferrite and austenite is consistent with experimental observation, whereas under subsequent NP-LE mechanism, the Mn profile almost keeps the same during the transformation.

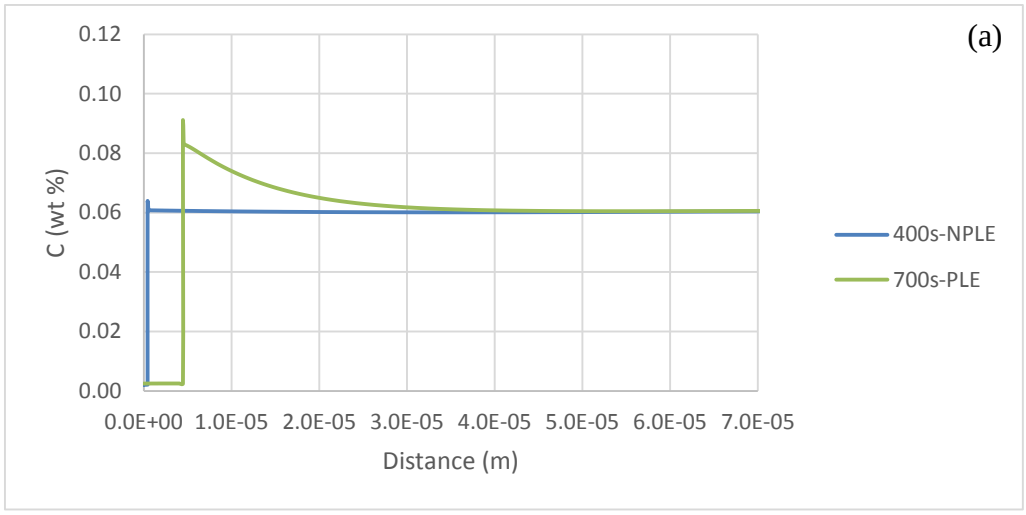

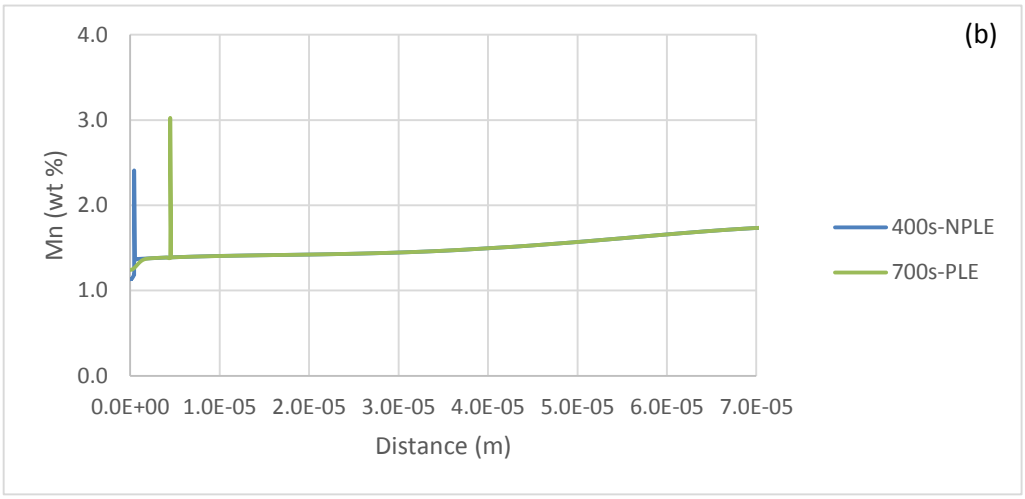

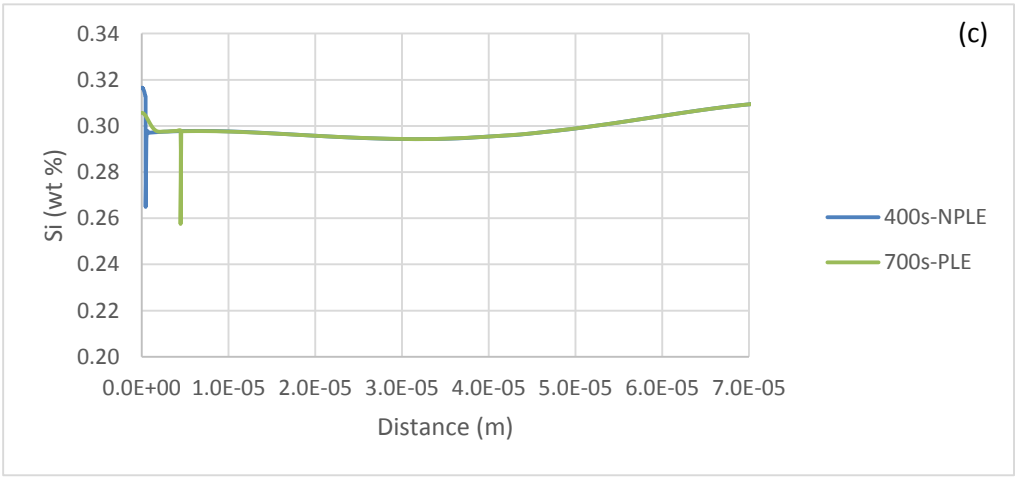

Figure 8-14 C (a), Mn (b) and Si (c) content (wt %) as a function of distance at different times corresponding to NP-LE and P-LE mechanism under local equilibrium assumption in the structural steel.

Table 8-2 The starting temperature (℃) of NP-LE, P-LE and ParaE growth mechanism for different steel.

	Structural	Ship building	Slab 1
T_{PLE}	847	832	828
$T_{NP\text{-}LE}$	822	778	808
T_{PE}	791	750	760

ParaE mechanism was investigated by DICTRA in steels separately from P-LE and NP-LE. The starting temperature for the P-LE, NP-LE and ParaE mechanisms according to their different elemental partition behaviour are listed in Table 8-2. ParaE mechanism occurred below the P-LE and NP-LE mechanism temperatures. The velocities of the ferrite / austenite interface v_i versus temperature for slab 1 and ship building steels predicted by DICTRA are shown in Figure 8-15 under LE and ParaE mechanisms. In a certain temperature range under ParaE starting temperature, the interface grew faster by the ParaE mechanism than by LE ones, while the driving force ΔG_v for the LE mechanism is greater than that for the ParaE mechanism. The total free energy change depends on both v_i and ΔG_v. Therefore, according to the global minimisation of Gibbs energy technique, ParaE growth is possible to substitute for NP-LE during the austenite-ferrite transformation. The profiles of substitutional alloying elements, such as Mn against distance remained almost unchanged under both NP-LE and ParaE mechanisms and only the initial part of the profile changed according to partition direction under the P-LE mechanism. So the substitutional element profiles obtained below the NP-LE starting temperature can be used to represent the final profiles at room temperature.

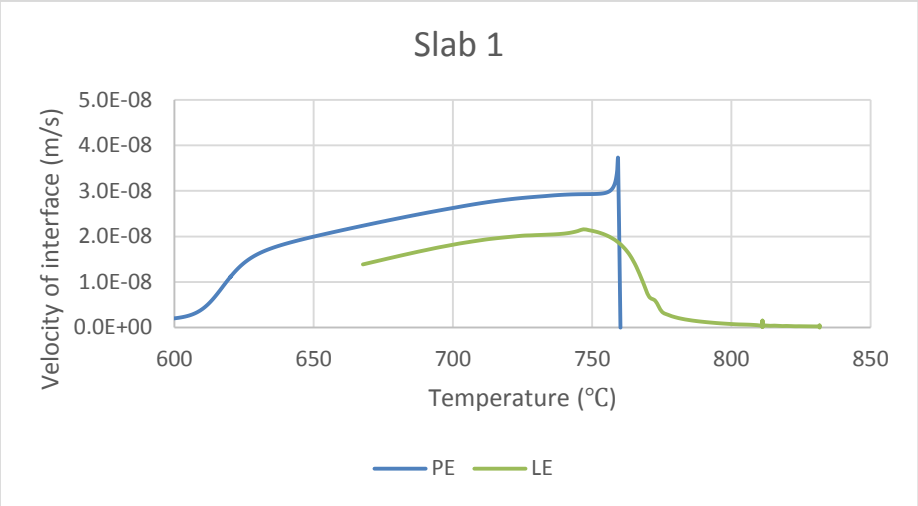

(a)

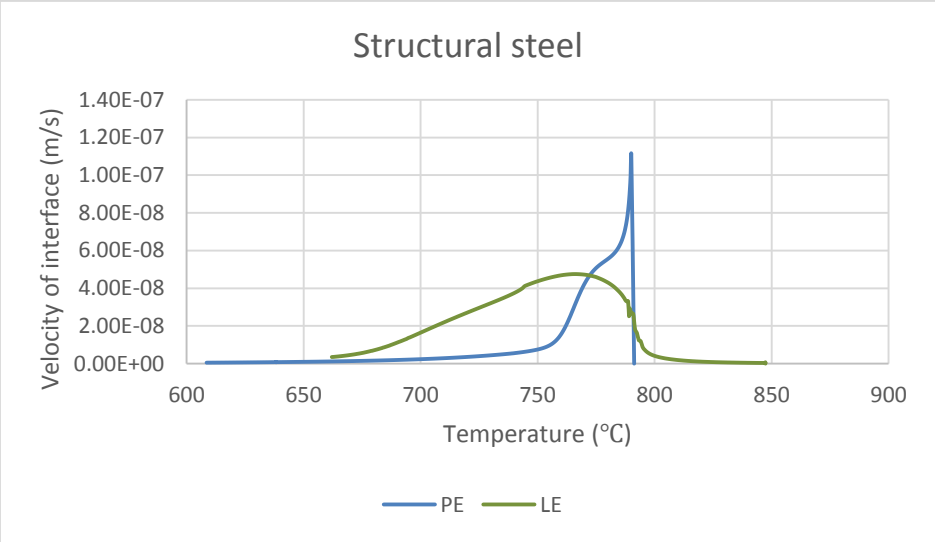

(b)

Figure 8-15 The velocity of interface as a function of temperature for slab 1 (a) and ship building (b) steels predicted by DICTRA.

8.2.3 The effect of microalloying elements (Al, V and Nb) on phase transformation and Mn diffusion

Due to limitation of DICTRA simulation, it is impossible to take all the elements into account and also, in order to save computing time, it is necessary to decrease the elements and phases being simulated. The substitutional alloying elements with a composition content over 0.1 wt % and the interstitial element carbon were chosen to be the basic elements as Fe-C-Si-Mn (-Ni) (the interstitial elements P and S were not taken into account for simulation in DICTRA). Microalloying elements, such as Nb and V with low content precipitate with C or N before proeutectoid ferrite starts to form and so the effect of these elements on proeutectoid ferrite formation can be ignored. The effects of these microalloying elements on the solidification process are investigated below. Liquidus, peritectic and solidus temperatures of the simplified system Fe-C-Si-Mn-Ni and with addition of different microalloying elements predicted by DICTRA are listed in Table 8-3. The microalloying elements with around 0.05 wt% content had little effect on the liquidus and peritectic temperatures. But the addition of Nb decreased the solidus temperature by 13 K.

In addition, the influence of the addition of microalloying elements on Mn segregation was investigated. The Mn profiles along half the SDAS in the simplified system Fe-C-Si-Mn and those with added different microalloying elements are shown in Figure 8-16. At 580 s referring to 1458 ℃, the steel composition with Nb has a higher Mn content in the interdendritic region due to a lower solidus temperature compared with other compositions. However, at 2000s, after elemental diffusion in austenite has taken place, the Mn profiles are almost the same with and without the different microalloying element additions. Therefore, the influence of added microalloying elements on the final Mn profiles can be ignored.

Table 8-3 The liquidus, peritectic and solidus temperatures (℃) predicted by DICTRA in slab 1 steel for the composition system Fe-C-Si-Mn-Ni-M, M is microalloying element: Nb, V and Al.

	Fe-C-Si-Mn-Ni	Fe-C-Si-Mn-Ni-(0.045%)Nb	Fe-C-Si-Mn-Ni-(0.052)V	Fe-C-Si-Mn-Ni-(0.046)Al
T_L	1518	1518	1518	1518
T_γ	1488	1487	1487	1488
T_S	1471	1458	1469	1472

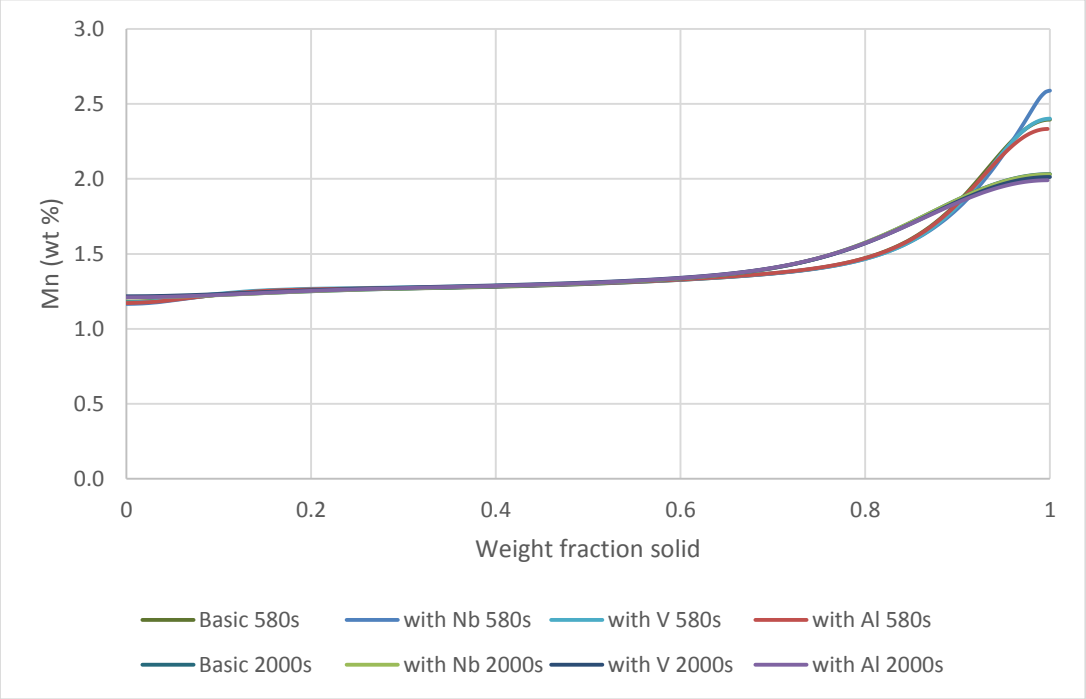

Figure 8-16 The Mn profiles as a function of solid fraction in slab 1 at different times with addition of different microalloying elements.

8.2.4 Effect of model variable-cooling rate and SDAS in the DICTRA model

The sensitivity of the parameters of cooling rate and SDAS on the results in the DICTRA model was investigated. The comparison of Mn segregation profiles by changing only one parameter (cooling rate or SDAS) is shown in Figure 8-17. When cooling rate increased from

0.13 to 1 K/s which covers the cooling rates used in all steels (0.13 - 0.81 K/s), the maximum Mn concentration increased from 2.0 to 3.0 wt %, whilst when SDAS changed from a minimum value of 90 µm to a maximum value of 270 µm for all the steels, the maximum Mn concentration increased from 1.6 to 2.0 wt %. The reason may be that, with increasing cooling rate, there is less back-diffusion in the solid during solidification and homogenisation after solidification, leading to more solute atoms being trapped in the interdendritic region. With increasing SDAS, the solute-rich region becomes bigger in volume and thus more solute atoms remain in the solute-rich region after casting with the same cooling rate. Therefore, decreasing both cooling rate and SDAS was predicted to reduce the microsegregation in steel. However, usually SDAS decreased with increasing cooling rate.

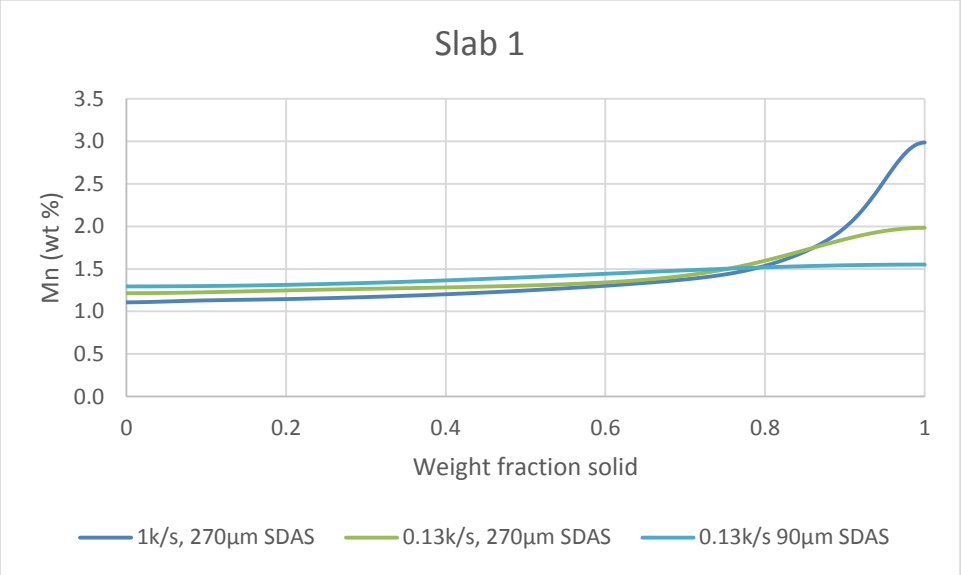

Figure 8-17 The comparison of Mn distributions in dendrites at 1200 ℃ in slab 1 steel by changing cooling rate from 0.13 to 1 K/s and SDAS from 90 to 270 µm.

8.2.5 Verification of DICTRA segregation prediction by comparison with experimental results

In order to assess the accuracy of DICTRA predictions for microsegregation, experimental segregation data described in section 6.2.3 were used to verify the simulated profiles. Some experimental details for the slabs and the parameters used in DICTRA simulation are listed in Table 8-4. The comparison of DICTRA predicted and SES experimental normalised Mn and Si concentration profiles for steels are shown in Figure 8-18 and Figure 8-19.

Table 8-4 C, Mn, Si and Ni content, solidification rate and SDAS values of investigated steels.

	C wt%	Mn wt%	Si Wt%	Ni wt%	Solidification rate ℃ /s	SDAS μm
Pipeline	0.03	1.7	0.25	-	0.8	165
Structural	0.06	1.52	0.3	-	0.81	140 ± 20
Slab 1	0.1	1.42	0.31	0.32	0.13	270 ± 50
Ship building	0.14	1.35	0.38	-	0.57	90 ± 15

SES experimental Mn profiles were scatter-free because Mn was chosen as a reference element in the SES sorting method. Root-mean-square deviation (RMSD) values were used to measure the average differences between DICTRA predicted and SES experimental Mn concentration profiles. 200 equally-spaced points were selected to compare DICTRA predicted profiles and experimental data and calculate the RMSD. The formula in Equation 8-16 was applied:

$$RMSD = \sqrt{\frac{\sum_{i=1}^{200}(\frac{C_{Mn,i}^{D}}{C_{0,Mn}^{D}} - \frac{C_{Mn,i}^{E}}{C_{0,Mn}^{E}})^2}{200}} \qquad 8\text{-}16$$

Where, i denotes the number of individual point; $c_{Mn,i}^{D}$ and $c_{Mn,i}^{E}$ are respectively the Mn concentration from DICTRA predictions and from experimental data at point i and their values increase with ascending order of i; $c_{0,Mn}^{D}$ and $c_{0,Mn}^{E}$ are the average Mn concentrations used in DICTRA and of experimental data.

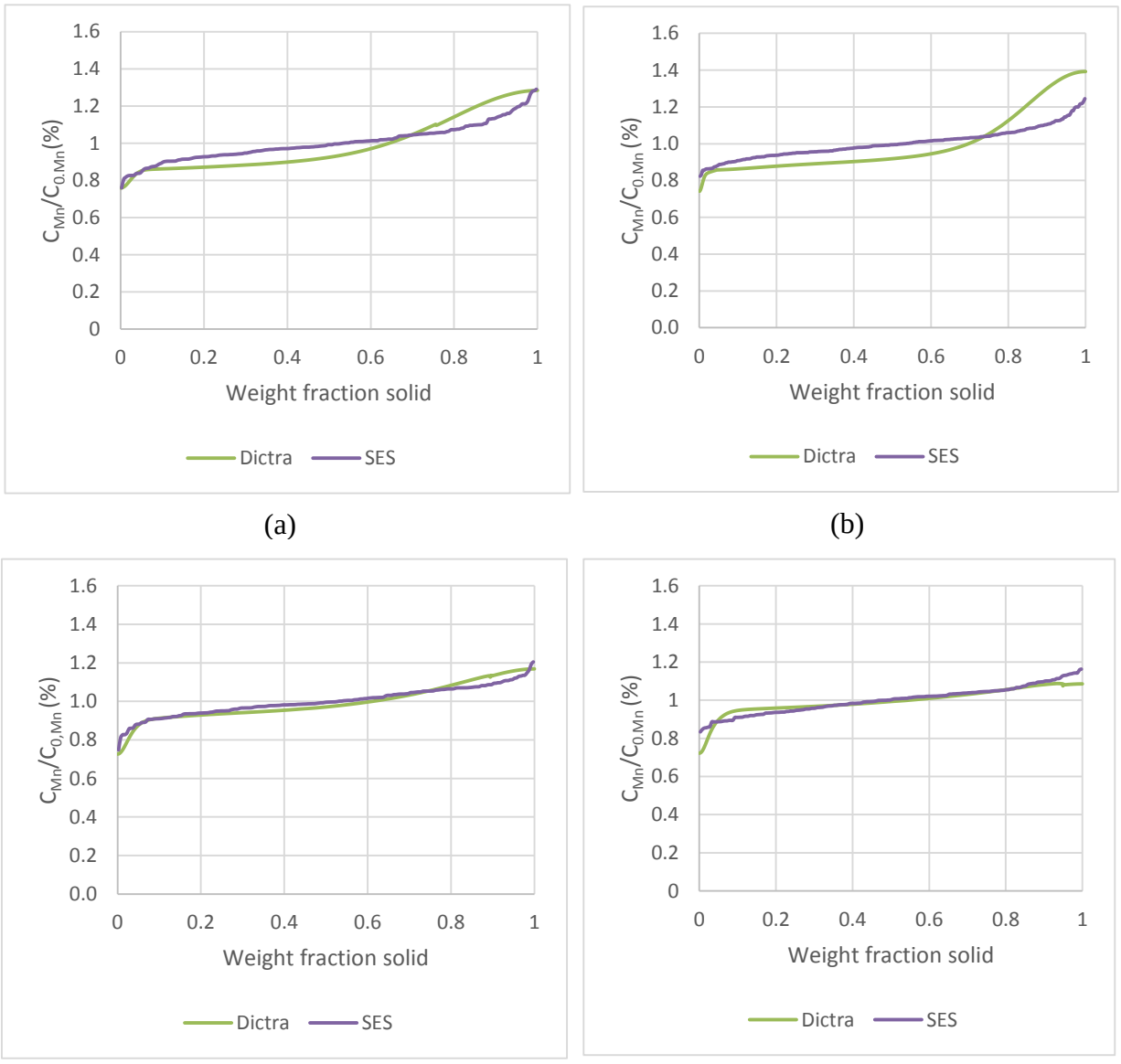

Figure 8-18 Comparison of SES experimental and DICTRA predicted Mn distribution from centre of dendrite to interdendritic region in (a) ship building, (b) slab 1, (c) structural and (d) pipeline steels.

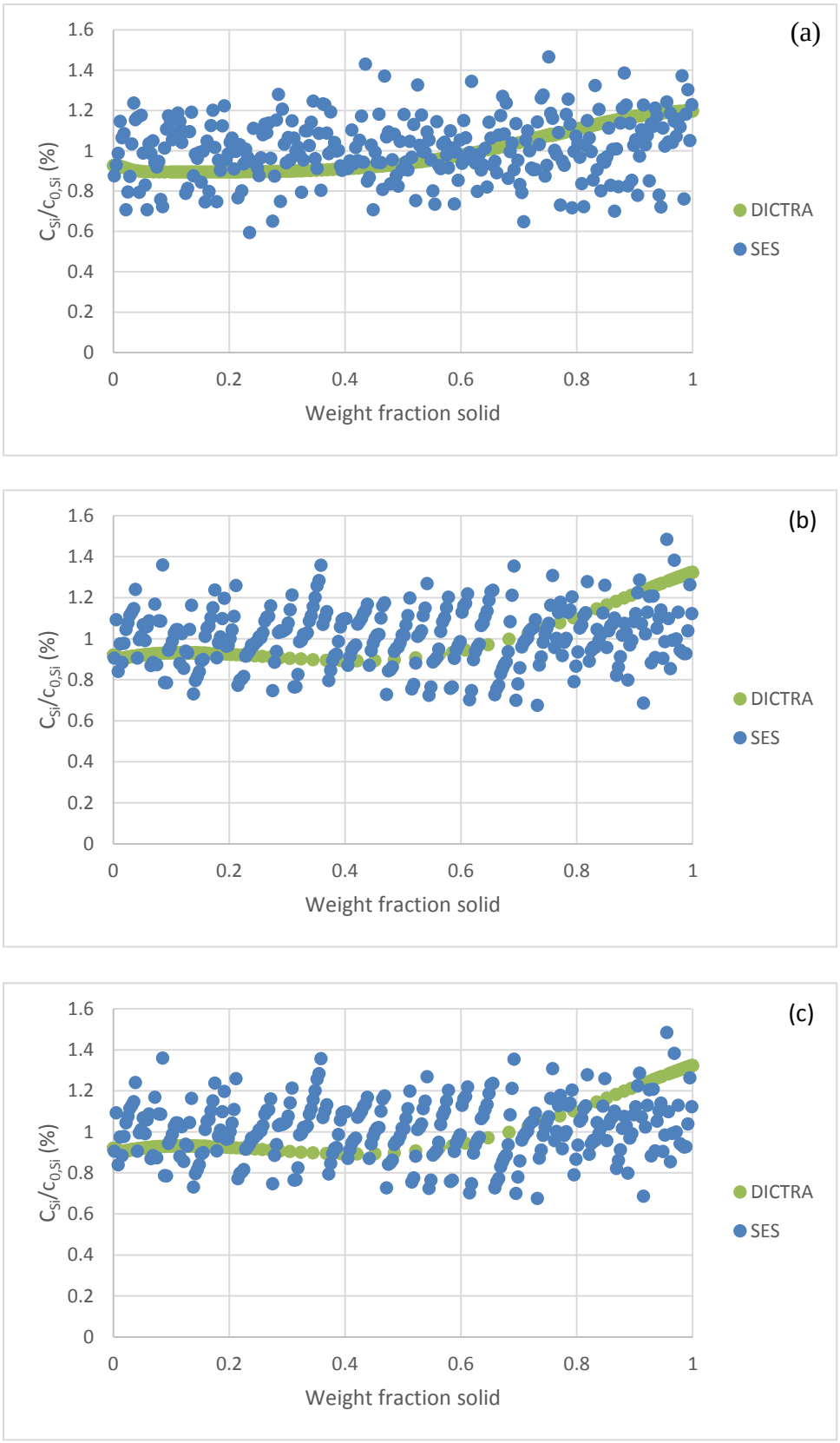

Figure 8-19 Comparison of SES experimental and DICTRA predicted Si distribution from centre of dendrite to interdendritic region in (a) ship building, (b) slab 1 and (c) structural steels.

The calculated RMSD values by using different model data (Clyne-Kurz, Scheil and DICTRA) and experimental data and experimental statistical deviation of the normalised Mn concentration in different steels from EDS measurements are listed in Table 8-5. The smaller the RMSD value is, the better the modelling fits the experimental data. From Table 8-5, RMDS values for Clyne-Kurz in different steels are smaller than those for Scheil and thus the Clyne-Kurz predicted Mn profiles fit the experimental results better. However, all the RMDS values for the analytical methods are over the standard deviation from EDS data which means that the discrepancy between modelling and experiment is beyond the experimental error allowance. As they show the smallest RMDS values among all models, DICTRA predictions agree with experimental data better than both analytical methods.

As to the DICTRA model, the predictions for Mn segregation profiles for structural and pipeline steels agree with the SES profiles better than for the ship building steel and also the values of RMSD for these three steels are smaller than the standard deviation of EDS data which means the deviation between predicted and experimental results is within the experimental error and hence has been taken to be acceptable. Slab 1 steel has the largest RMSD value, greater than the statistical deviation of the experimental data, so that effort should be made to improve it. For SES experimental Si profiles, the scatter existed due to the uncertainty from EDS measurements. The scatter of SES Si profiles in the steels except slab 1 steel covered the DICTRA predicted profiles. In slab 1 steel, the predicted Si concentrations in the solute rich region seems higher than the experimental ones. Therefore the observation from Si profiles further confirms that the DICTRA prediction of slab 1 steel does not match experimental results well.

One of the reasons for this discrepancy may be the uncertainty of the cooling rate. According to previous analysis, decreasing cooling rate can reduce the segregation level. However, the

cooling rate for slab 1 (0.1 k/s) is quite low, so further decreasing it may not change the segregation distribution much and be beyond the practical limitation. Dendrite arm coarsening may be another reason. There are two main mechanisms for coarsening: ripening and coalescence presented in section 2.3.2 . The ripening mechanism is reported to occur at the lower fraction solid where the segregation is less sensitive to length scale; the coalescence mechanism prevails at higher solid fractions [30]. Turkeli reported that at a cooling rate of 0.25 K/s, the coalescence mechanism dominated the dendrite arm coarsening process rather than the ripening mechanism observed at the higher cooling rates in Fe-C-Mn steels [55]. The slab 1 steel has the lowest cooling rate among all the steels, so that the coarsening by thcoalescence mechanism may occur. Before coalescence happens, smaller second dendrite arms exist, which decrease the segregation in the solid. Therefore, for slab 1 steel, the DICTRA model, which does not consider the coalescence coarsening effect, may overestimate the microsegregation.

Table 8-5 The RMSD values of normalised Mn segregation profiles and the statistical deviation of EDS experimental data in SES profiles in different steels.

	Ship building	Slab 1	Structural steel	Pipeline
RMSD	0.05	0.1	0.02	0.02
Clyne-Kurz	0.19	0.2	0.15	0.16
Scheil	0.25	0.28	0.40	0.40
Statistical deviation (wt %)	0.09	0.08	0.08	0.07

The microalloying element distributions in the dendritic structure were also predicted by DICTRA. The profiles taken at the precipitate-forming temperature predicted by Thermo-Calc

based on the bulk composition were used to represent the elemental distribution, frozen in place by precipitation. The segregation level of microalloying elements in slab 1 measured by SEM-EDS and WDS by Chakrabarti et al. [6] were used to compare with the DICTRA prediction. The precipitate-forming temperatures from Thermo-Calc are listed in Table 8-6.

The Nb and V concentration profiles in Figure 8-20 (a) and (b) show that Nb and V are enriched in the interdendritic region, while the Nb segregation is more severe than the V segregation in steel. The predicted maximum Nb, and V contents in the interdendritic region are greater than the measured values, the ratio of maxima of DICTRA predicted and experimental element concentrations (C_{max}^{D}/C_{max}^{E}) is similar for Nb and V with the ratio for Mn (1.16). In the dendrite core area, the predictions are similar with measurements (Table 8-7). Therefore, to some extent, the fitting behaviour between DICTRA prediction and experimental results has consistency for different alloying elements in slab 1 steel.

Table 8-6 Bulk equilibrium precipitate forming temperature of Slab 1 steel predicted by Thermo-Calc.

Precipitate forming temperature	Ti(N)	Nb(CN)	AlN	V(C)
Slab 1(K)	1619	1468	1409	1058

Table 8-7 Comparison of DICTRA predicted and experimental segregation levels of microalloying elements in solute-deleted and solute-rich regions of slab 1 steel.

Slab 1		Nb	V
Dendrite center	DICTRA	0.03	0.051
	Experimental	0.027	0.047
Interdendritic	DICTRA	0.088	0.064
	Experimental	0.075	0.056
	C_{max}^{D}/C_{max}^{E}	1.17	1.14

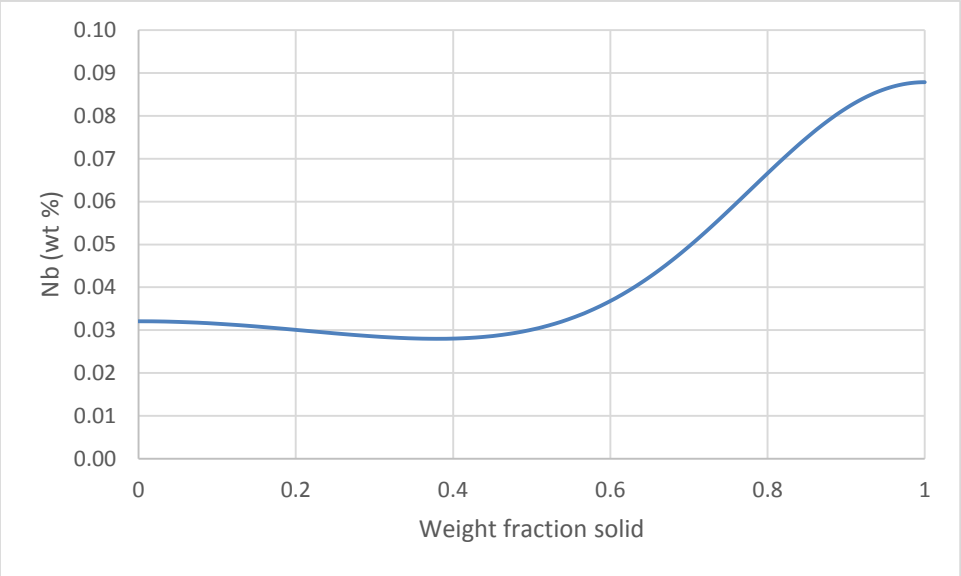

(a)

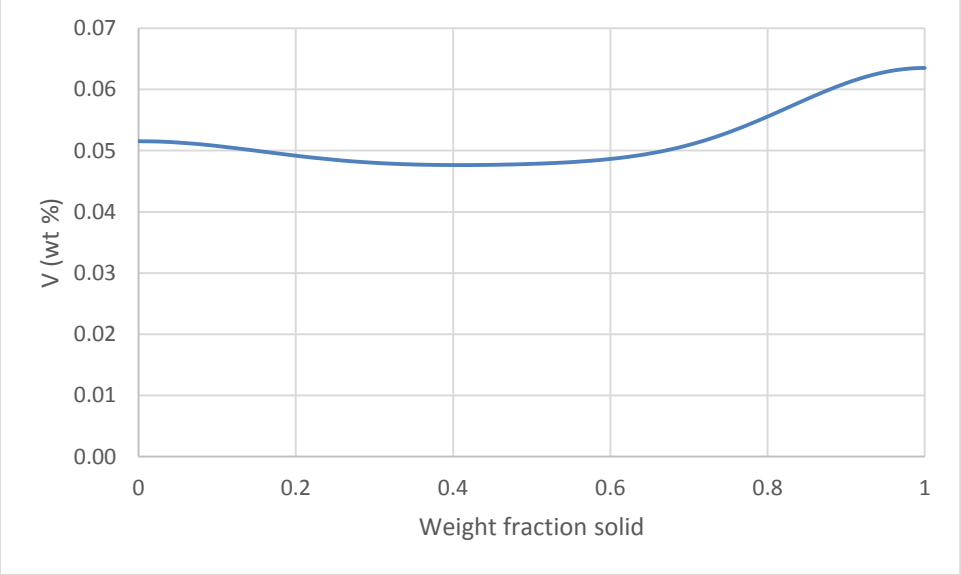

(b)

Figure 8-20 Predicted (a) Nb and (b) V weight percent as a function of solid fraction from the centre of the dendrite in slab 1 steel.

8.3 Conclusions

1. A numerical 1-D heat transfer model was used to predict the cooling rate for the air cooling process.
2. According to the DICTRA prediction, the peritectic reaction had a significant effect on the formation of segregation. Steels undergoing the peritectic reaction had greater segregation levels than the steel solidifying without the peritectic reaction. The transformation of austenite to α-ferrite has little effect on the alloying element distribution except an initial sharp slope part in the dendritic core region.
3. According to DICTRA predictions, the addition of microalloying elements such as Nb and V has little effect on liquidus and peritecitc temperatures. However, the addition of Nb decreased the solidus temperature by more than 10 degrees. Also, the addition of microalloying elements has no influence on the final profiles of Mn against distance. So the composition system for simulation was simplified into Fe-C-Si-Mn(-Ni)-M, where M is one of the microalloying elements.
4. Cooling rate and SDAS can significantly affect the formation of segregation predicted by DICTRA. By only increasing the cooling rate from 0.13 to 1 K/s and SDAS from 100 to 270 μm in slab 1 steel, the maximum Mn concentration at 1200 ℃ increased from 2.0 to 3.0 wt % and from 1.55 to 2.0 wt % respectively.
5. Root-mean-square deviation (RMSD) was used to characterise the deviation between the DICTRA predicted and SES experimental Mn profiles. In most of the steels, the values of RMSD were less than experimental standard deviation except for the slab 1 steels. The cooling rate or dendrite arm coarsening by coalescence mechanism at low cooling rates may be the reason for the discrepancy between prediction and experiment in slab 1 steel.

6. Compared with the EDS or WDS measurement in the dendritic core and interdendritic regions in Slab 1, Nb and V concentration predicted by DICTRA has similar fitting features with experimental results as Mn.

Chapter 9 Comparison of DICTRA predictions with directional solidification results and published data

From the last chapter, the use of an inaccurate cooling rate in DICTRA simulations may be a reason for the discrepancy between modelling and experimental results. Hence, a casting performed under known cooling conditions was carried out and the resulting ingot characterised for comparison with DICTRA simulation. Therefore the directional solidification (DS) trials described in section 5.1 were carried out to give dendritic structures that could be analysed in terms of microsegregation and, for which, accurate thermal histories were available. The thermocouples inserted into the mould, Figure 5-4, during casting monitored the temperature change which was recorded with time by the control system of the DS furnace. In addition, experimental data from literature reports which give clear cooling rates were also used to verify DICTRA simulations.

9.1 The cooling history of DS steels

Temperature was measured by the thermocouple during the casting trials in the DS furnace. Two DS trials with different withdrawal rates which can lead to two different cooling rates and one thermal cycle which was used to compare with the real casting temperature profile against time Table 9-1 were carried out with large baffles. The withdrawal rates for the different trials were listed in Table 9-1. In the DS trial 1, 200 mm/h withdrawal rate was used at the beginning of the trial and decreased to 100 mm/h when the ram position was more than 140 mm below the baffle. Decreasing the withdrawal rate in the later part of this trial was to reduce the cooling rate at the lower temperatures and reduce the amount of bainite phase formed in the steel in order that the dendritic structure can be more clearly resolved.

Table 9-1 Withdrawal rate applied in DS trials and thermal cycle test.

	DS trial 1	DS trial 2	Thermal cycle test
Withdrawal rate (mm/h)	200-100	50	229

The variations in temperature as a function of time for DS trials and thermal cycle test are shown in Figure 9-1. The cooling rates were calculated from the recorded temperature versus time data by $\Delta T/\Delta t$ which represents the cooling rate at time of $t + \Delta t$, where T is temperature, ℃ and t is time, s. The recorded temperatures are integers and the cooling rates are less than 1 ℃/s so that the temperature recorded remained the same over a certain time period. In order to avoid zero calculated cooling rate, Δt should be larger than the maximum of those time periods: Δt = 50 s was used in DS trial 1 and a thermal cycle with the higher cooling rate and Δt =100s was used in DS trial 2 with the lower cooling rate.

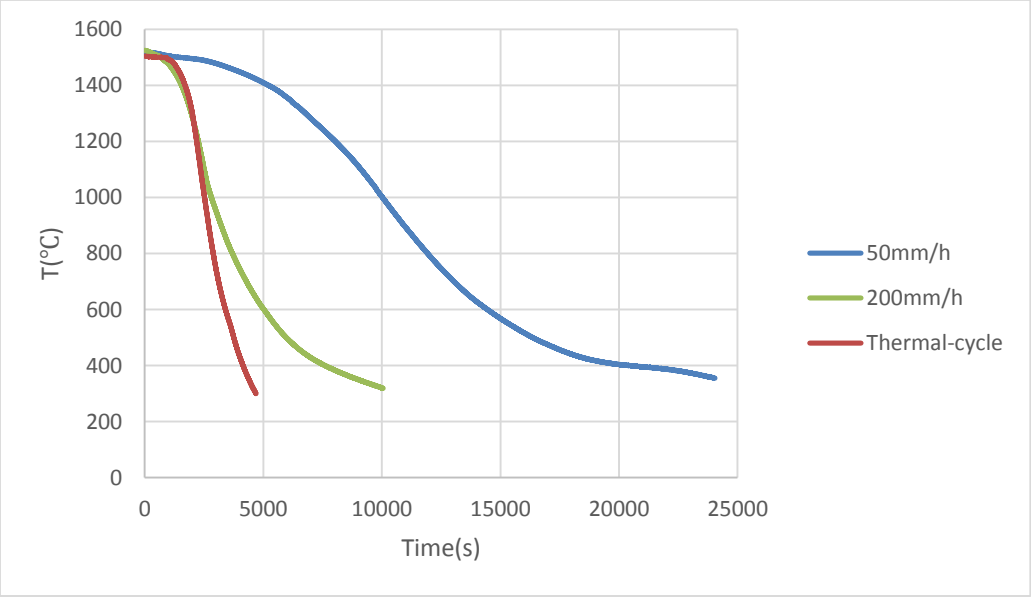

Figure 9-1 Temperature as a function of time of DS trials at withdrawal rates of 50, 200 - 100 mm/h and thermal cycle test.

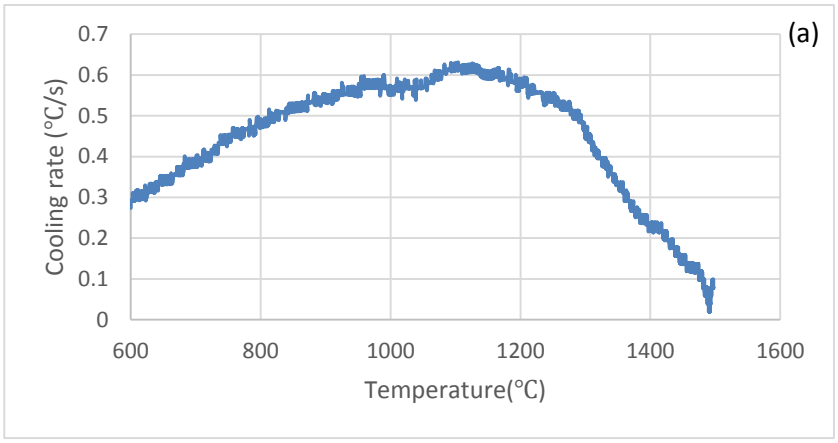

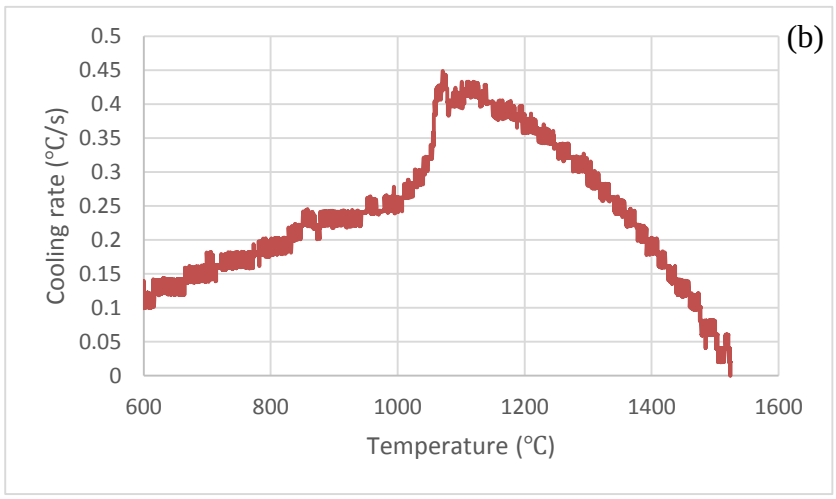

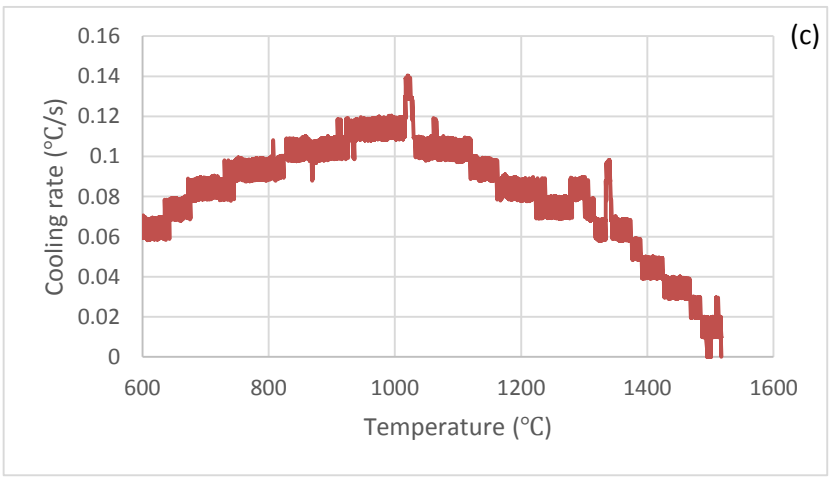

Figure 9-2 Cooling rate as a function of temperature during (a) thermal cycle test and DS castings at withdrawal rates of (b) 200 - 100 mm/h and (c) 50 mm/h.

The cooling rate against temperature plots during the thermal cycle test and DS castings are shown in Figure 9-2. The cooling rate increased first to a maximum and then decreased as temperature decreased. Cooling rate profile of DS trial 1 at withdrawal rate of 200 - 100 mm/h was reduced at about 1100 ℃ more than that of thermal cycle test probably due to the withdrawal rate change around that temperature. The cooling rates of DS trial 2 at 50 mm/h withdrawal rate are lower than those of DS trial 1 at the withdrawal rate of 200-100 mm/h. The maximum cooling rates and solidification rates of these two DS trials are listed in Table 9-2. The cooling rates of DS trial 1 at the withdrawal rate of 200 - 100 mm/h were 2 - 3 times of those of DS trial 2 at the withdrawal rate of 50 mm/h. The solidification rates of DS trials (0.02 - 0.06 ℃/s) are small compared with those of continuously cast steel slab (0.13 - 0.81 ℃/s).

Table 9-2 Maximum cooling rate and solidification rate of DS samples at withdrawal rates of 50 and 200 - 100 mm/h.

C_R (℃/s)	Max (C_R)	Solidification rate (℃/s)
200-100 mm/h	0.45	0.04-0.08
50 mm/h	0.14	0-0.02

9.2 Microstructure of DS steels

The microstructures of DS samples were investigated in order to obtain SDASs related to the thermal profiles recorded. The DS samples 1 and 2 from DS trial 1 and 2 at 200 – 100 and 50 mm/h withdrawal rate respectively were cut just above the position where the thermocouple was located. The longitudinal sections were prepared according to the description in section 5.2.1 . Representative microstructures from DS samples 1 and 2 are shown in Figure 9-3 and

Figure 9-4. The microstructure of DS sample 1 consisted of ferrite and pearlite with patches of bainite (Figure 9-3 (b)). During DS casting, carbon was lost (to the atmosphere) and the bulk carbon content for DS sample 1 is 0.046 wt % and for DS sample 2 it should be lower. In DS sample 1, the microstructure patterns are not identical across the whole sample area. Figure 9-3 (c) shows the regions without clear dendrite structures which were located randomly across the section, while the dendrite structures are only clear in some regions Figure 9-3 (a), in which the SDAS was 90 ± 20 μm, may indicate the secondary dendrite arms only developed in some areas from primary arms due to low carbon content and low solidification rate. The bainite was formed below the eutectoid temperature and so it will not affect the segregation characterisation of DS samples.

There is a lower pearlite fraction in the microstructure of DS sample 2 from DS trial 2 at 50 mm/h withdrawal rate (Figure 9-4) and the dendrite structures were not observed in DS sample 2. Therefore only DS sample 1 at the withdrawal rate of 200 - 100 mm/h was used in the DICTRA model. For this sample, the recorded solidification rate and calculated solidification rate based on the SDAS value by Equation 3-1 used in DICTRA model in Chapter 8 was listed in Table 9-3. The calculated solidification rate is 2 orders of magnitude more than the recorded one indicating the use of this equation to calculate the solidification rate might account for some of the errors seen in Chapter 8 .

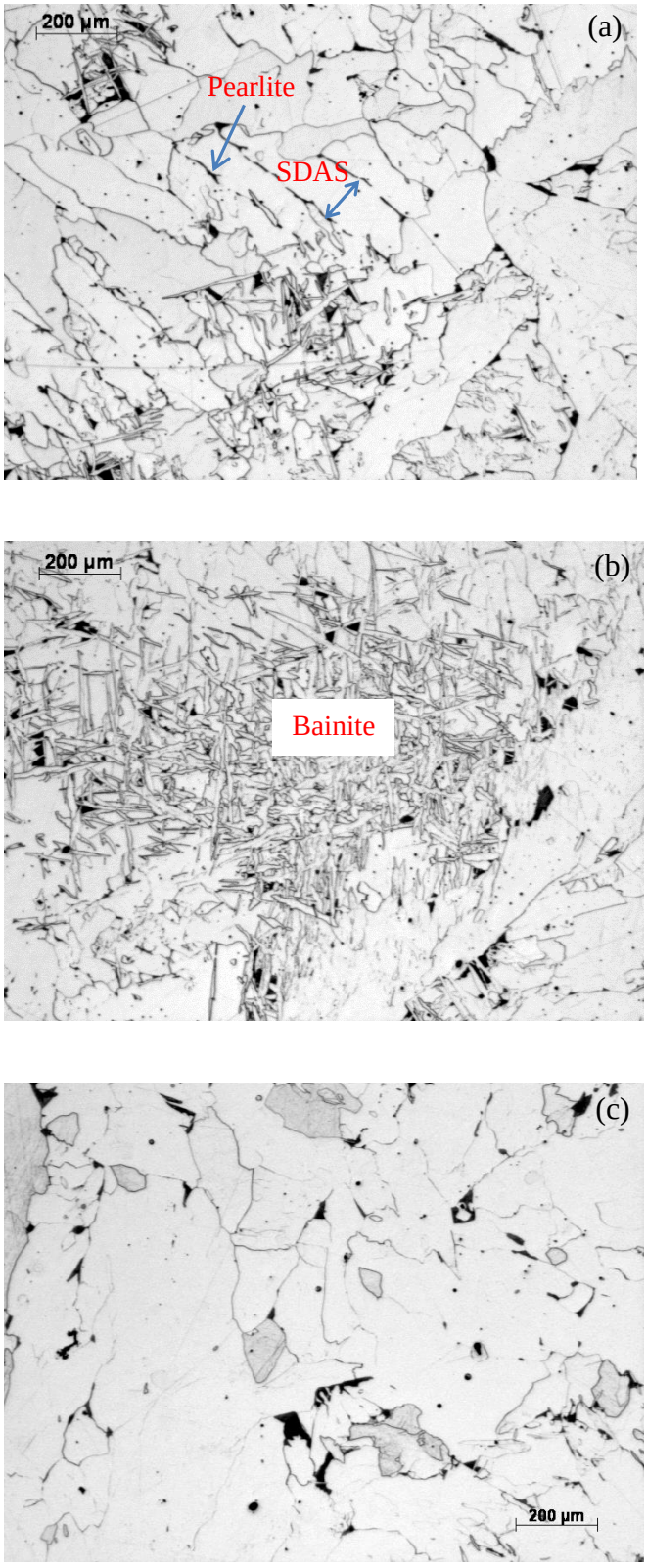

Figure 9-3 Typical microstructures of DS sample 1 on the longitudinal section with (a) dendrite structure, (b) bainite and (c) lower pearlite fraction.

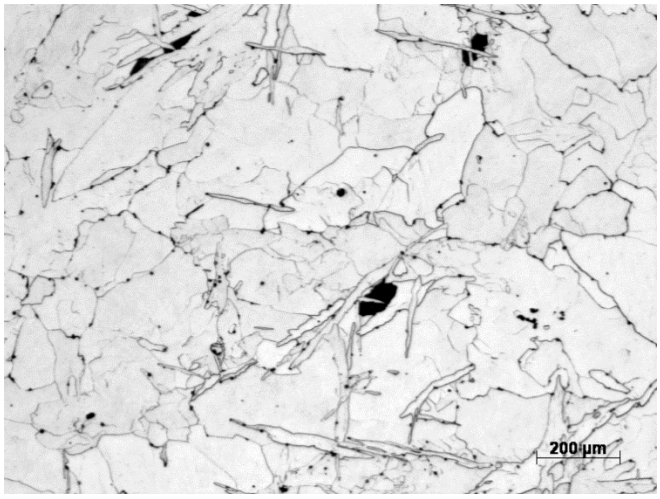

Figure 9-4 Typical microstructure of DS sample 1 on the longitudinal section.

Table 9-3 Comparison of recorded cooling rate and calculated from the SDAS by Equation 3-1 of DS trials.

	Experimental	Calculated
Solidification rate (℃/s)	0.04-0.08	2.31

9.3 DICTRA simulation

The DICTRA prediction was carried out by inputting an equation of temperature/time relation fitted from the recorded temperature/time data and average SDAS value. $\delta(x) = 0.1$ μm and Max ($\delta(t)$) =10 s were used in this simulation. The total simulation time was 10000 s. The other settings in DICTRA were the same as the ones applied in DICTRA for continuously cast steel slabs in Chapter 8 . No peritectic reaction was predicted to occur during solidification due to the very low carbon content.

9.4 Cumulative EDS mapping

In order to verify the DICTRA prediction for segregation in the DS samples under a known cooling rate, experimental cumulative EDS profiles were obtained as descried in section 5.2.3 . EDS spectra from 200 points located in square mesh grids with equidistant spacing of 200 μm were measured. In DS sample 1, Mn, Si and Ni all have similar low contents of about 0.4 to 0.5 wt %. The WIRS (weighted interval rank sort) method described in section 3.2.3.4 was chosen to sort the elements in DS sample 1. Both Mn and Ni were taken into account in the sorting scheme because their content increases monotonically from the dendrite centre to the interdendritic region; Si was sorted based on them.

9.5 Verification of DICTRA prediction for segregation by cumulative segregation profiles

Comparison between DICTRA prediction and measured WIRS segregation profiles was carried out for DS trial 1. Figure 9-5 shows the Mn, Ni and Si DICTRA predicted and WIRS sorted profiles as a function of distance from the centre of the dendrite. The WIRS profiles were scattered due to the uncertainty of the EDS measurements. Standard deviations for normalised elemental contents are listed in Table 9-4. The simulated profile falls within the scatter band. The best fit to the WIRS sorted data for Mn and Ni shows an increase towards the interdendritic centre, which is not shown by DICTRA. There is also a deficit at the dendrite centre. The diffusion of Mn, Ni and Si in δ-ferrite used in DICTRA may be faster than the real situations and cause the discrepancy between the simulation and the best fit to WIRS profiles in the centre of the dendrite.

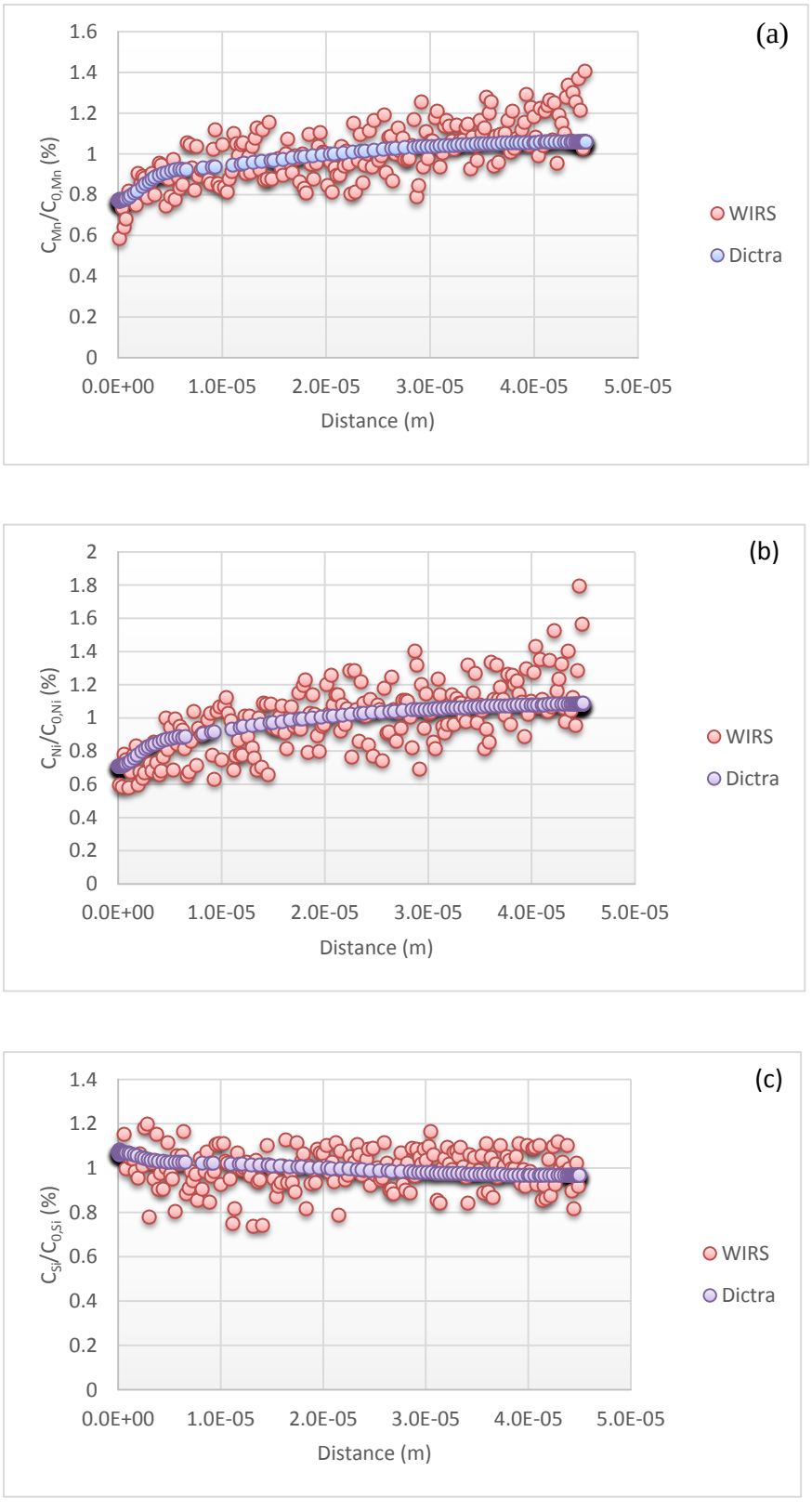

Figure 9-5 Comparison of DICTRA predicted and WIRS sorted normalised composition profiles for (a) Mn, (b) Ni and (c) Si in DS trial sample 1.

Table 9-4 Standard deviation of normalised Si, Mn and Ni contents from EDS measurements.

Spectrum	Si	Mn	Ni
Std. deviation	0.078	0.15	0.17

9.6 Comparison with Howe's numerical modelling and experimental results from literature reports

Howe's numerical model was summarised by Howe et al. to be more efficient for the prediction of solidification and microsegregation in peritectic alloys than a number of different schemes [111]. In this model, parameters such as partition coefficient *k* and diffusion coefficient in each phase in this model are based on binary systems and only the effect of temperature on each parameter can be considered, as mentioned in section 4.4.2 However, partition coefficients (section 7.1.2) and diffusion coefficients depend on both element concentration and temperature (section 4.4.3.1).

In contrast, DICTRA assessed the experimental data and used a CALPHAD method to obtain thenatomic mobility of each element in a multicomponent system as a function of temperature and composition. The diffusivity matrix as a function of temperature and composition was calculated according to the atomic mobility.

In order to examine the difference between DICTRA and Howe's model, the experimental results along with predicted results by Howe's model from the literature report were used to compare with the DICTRA model prediction.

A series of experiments investigated by Turkeli on the unidirectional solidification of Fe-C-Mn steels (0.1-0.21 wt % C and ~1.5 wt % Mn) [55] were also used for comparison between

Howe's model and DICTRA. The alloys were solidified under a constant cooling rate and specimens were quenched during solidification and homogenisation after solidification to characterise the segregation and microstructure. The cooling rates, quenching temperatures for segregation characterisation and primary arm spacing in two steels are listed in Table 9-5 and used as input in the DICTRA modelling.

For the composition and the cooling conditions mentioned above, a cylindrical cellular model based on the primary dendrite arm space was used in a DICTRA simulation, as was the case for Howe's model, because the secondary dendrite arms were poorly developed. $\delta(x) = 1$ μm and $\mathrm{Max}(\delta(t)) = 100$ s were used in this DICTRA simulation. The calculation went through the homogenisation after solidification and finished at the quenching temperature listed in Table 9-5.

Table 9-5 Cooling rate, quenching temperature and primary arm spacing in Fe-Mn-C steels.

Cooling rate K/s	Quenching temperature, ℃	Primary arm spacing, μm
0.1C-1.5Mn		
0.25	1370	312
0.3	1220	258
0.39	1200	228
0.21C-1.6Mn		
0.25	1225	350
0.39	1120	225

The comparisons between the experiment, Howe's model and DICTRA are listed in Figure 9-6. Predicted maximum Mn concentrations by Howe's model and DICTRA have similar

trends with different cooling rates and quenching temperatures. However, the DICTRA predictions are always greater than Howe's predictions. The Mn partition coefficients used in Howe's model based on a binary system are slightly higher than Mn partition coefficients in the Fe-C-Mn system predicted by Thermo-Calc, as shown in Table 9-6. The smaller partition coefficients used in DICTRA is one reason for the higher maximum Mn concentration. Howe's model only considered binary systems of Fe-C and Fe-Mn. The effect of cross-diffusion between C and Mn and concentration gradient of each element on Mn diffusion is expected to be another reason to cause the discrepancy.

Also, the experimental results are in between the predictions of Howe's model and DICTRA. In 0.1 C-1.5 Mn steel, solidified at lower cooling rate (0.25 ℃/s), the experimental results are closer to the prediction of Howe's model, while at higher cooling rates (0.3 and 0.39 ℃/s), the DICTRA prediction agree with experimental results better, as shown in Figure 9-6 (a). In 0.21 C-1.6 Mn steel, the experimental results were right in the middle of the two series of predictions for all the cooling rates. The maximum Mn contents were obtained by averaging several ones from line scans across primary arms. Mapped spectra results were available for the 0.1C-1.5Mn steel at 0.25 ℃/s cooling rate, shown in Figure 9-7. The most segregated pink regions in Figure 9-7 were in the four corners of each primary arm so that the line scans on the transverse section may miss out the most segregated area leading to smaller maximum experimental values.

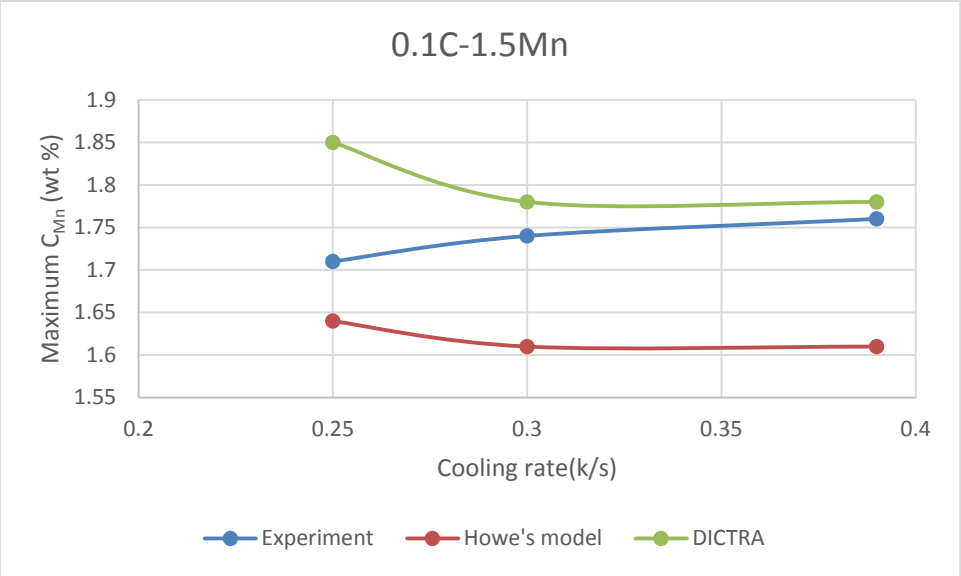

(a)

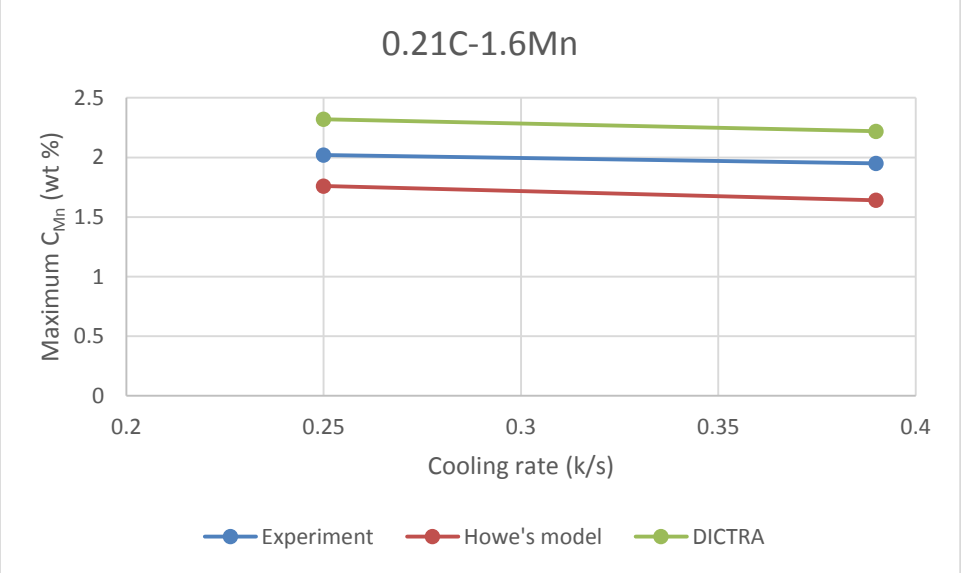

(b)

Figure 9-6 Experimental from the reference and predicted maximum Mn concentrations as a function of cooling rate by Howe's and DICTRA models in (a) 0.1 C-1.5 Mn and (b) 0.21 C-1.6 Mn steels.

Table 9-6 Average Mn partition coefficients predicted by Thermo-Calc and Mn partition coefficients used in Howe's model.

Partition coefficient k	$k_{Mn}^{\delta/L}$	$k_{Mn}^{\gamma/L}$
Howe's model	0.74	0.78
Thermo-Calc	0.72	0.74

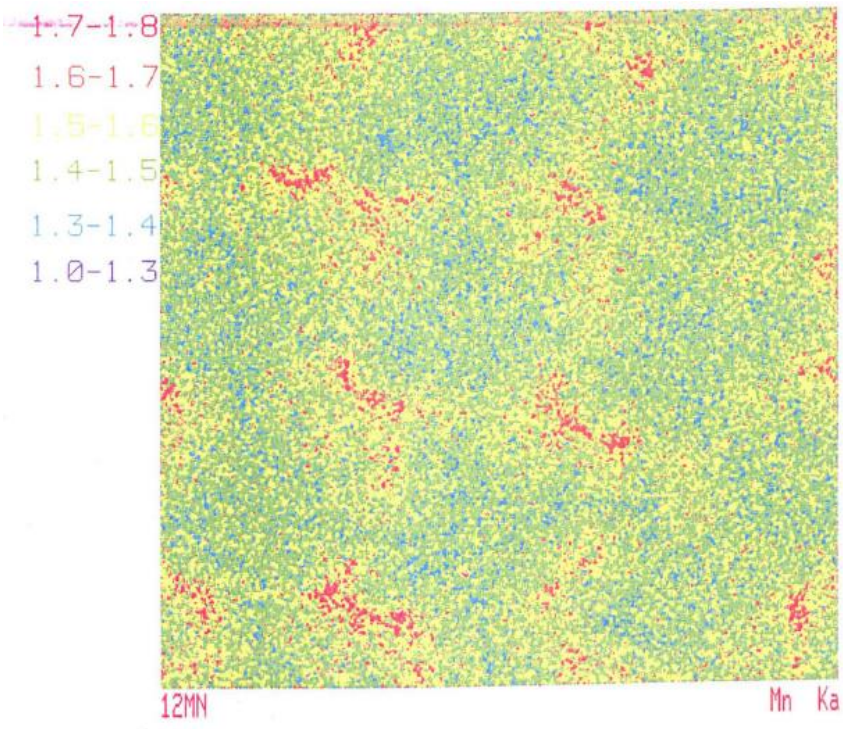

Figure 9-7 Colour concentration map of primary arms on the transverse section of 0.1C-1.5Mn steel at 0.25 ℃/s cooling rate.

9.7 Conclusions

1 Directional solidification trials were carried out to provide microsegregation data by the WIRS method along with precise thermal history.

2 The DICTRA prediction using the measured cooling rate and SDAS fell into the scatter band of WIRS profiles. However, there is discrepancy between the simulation and best fit to the WIRS profiles in the centre of both the dendritic and interdendritic regions. The reason may be that the diffusion of Mn, Ni and Si in δ-ferrite used in DICTRA is faster than the real situations.

3 DICTRA predictions for Mn segregation in Fe-C-Mn steel from literature reports are greater than the predictions from Howe's model. The smaller Mn partition coefficients applied in DICTRA is one reason for the greater Mn segregation predicted by DICTRA. Also, the effect of cross-diffusion of C-Mn and the concentration gradients of different elements on the Mn diffusion may be another reason to cause the discrepancy.

4 DICTRA predictions are also higher than the experimental results from literature reports. That may be because the line-scans method used to characterise segregation in the steels can miss out the most segregated region on the cross-section and cause lower experimental maximum Mn concentrations than the DICTRA predictions.

Chapter 10 Conclusions and suggested further work

10.1 Conclusions

Through characterisation and modelling of Mn, Si and Ni segregation by analytical approaches (Clyne-Kurz and Scheil models) and DICTRA of continuously cast steel slabs and directionally cast steels, the following conclusions can be drawn.

Characterisation of macrosegregation and microsegregation

1. Four continuously cast steel slabs were chosen and investigated in terms of microsegregation. Slab 1 and ship building steels with higher carbon contents (0.1 - 0.14 wt %) were predicted to be peritectic steels; structural and pipeline steels with lower carbon contents (0.03 - 0.06 wt %) were predicted to be non-peritectic steels by Thermo-Calc. Peritectic reaction was assumed to have significant effect on microsegregation development during solidification.
2. In continuously cast steel slabs, macrosegregation existed across the thickness direction with centreline enrichment. At the quarter thickness position, the microstructures are a mixture of pearlite and ferrite.
3. Grid-mapping and line-scans show that Mn and Ni atoms segregated into interdendritic regions during solidification.
4. Mn cumulative profiles sorted by SES in different steels have a similar shape: sharp slope initially, shallow sloping middle part and higher sloping last part. The change of slope between the middle part and the last part was assumed to separate the solute-rich and solute-depleted regions. Solute-rich fractions from Mn cumulative profiles increased with increasing carbon content in the steel.

Microsegregation modelling by Thermo-Calc software and analytical approaches (Clyne-Kurz and Scheil models)

1. Slab 1 and ship building steels, with higher carbon contents, were predicted by Thermo-Calc to solidify via a peritectic reaction, while the predictions for structural steel and pipeline steel with lower carbon contents give full solidification as δ phase before austenite forms.
2. The partition coefficients of solute elements during solidification predicted by Thermo-Calc decreased with decreasing temperature and were larger than the ones obtained from binary (Fe-X) systems except for phosphorus.
3. The austenite layers formed at the interface of δ/L during the peritectic reaction were assumed to trap the enriched elements in the liquid. The remaining liquid fractions were used to predict the solute-rich fractions.
4. Solute-rich fractions predicted by the Clyne-Kurz and Thermo-Calc models agree well with experimental results. The Clyne-Kurz model was better in predicting segregation profiles than the other two methods when compared with experimental results.

Microsegregation predicted by DICTRA

1. According to DICTRA predictions, the structural steel solidified through a peritectic reaction which is different from the Thermo-Calc prediction. The reason may be the segregation formed during the solidification which causes changes of solidus and austenite forming temperatures.
2. According to DICTRA predictions, the peritectic reaction had a significant effect on the formation of segregation. Steels undergoing the peritectic reaction had greater segregation levels than the steel solidifying without the peritectic reaction. The

transformation of austenite to α-ferrite has little effect on the alloying element distribution except for an initial sharp slope part in the dendritic core region.

3. According to DICTRA predictions, the addition of microalloying elements such as Nb and V has little effect on liquidus and peritecitc temperatures. However, the addition of Nb decreased the solidus temperature by more than 10 degrees consistent with severe Nb segregation during solidification.
4. Cooling rate and SDAS can significantly affect the formation of segregation predicted by DICTRA. By increasing the cooling rate from 0.13 to 1 K/s and SDAS from 100 to 270 μm in slab 1 steel, the maximum Mn concentration at 1200 ℃ increased from 2.0 to 3.0 wt % and from 1.55 to 2.0 wt % respectively.
5. RMSD values were used to characterise the deviation between the predicted and the experimental Mn segregation profiles. In terms of RMSD values obtained for the various models in the continuously cast steels, the DICTRA predictions have a better agreement with experimental results than Clyne-Kurz predictions. The RMSD values for Clyne-Kurz model were greater than the experimental standard deviations. In most of the steels studied, RMSD values for DICTRA prediction were less than experimental standard deviations. The exception was slab 1 steel. Cooling rate and dendrite arm coarsening effects may be the reason for the discrepancy between prediction and experimental results in slab 1 steel.

Comparison of DICTRA predictions with directional solidification results and published data

1. DICTRA predictions of DS samples using the measured cooling rate and SDAS values fell within the scatter bands of WIRS profiles. However, a discrepancies between the

simulation and best fit to the WIRS profiles in the centre of dendrite and interdendritic regions were found. The reason may be that the diffusion rates assumed for Mn, Ni and Si in δ-ferrite in DICTRA are slightly faster than in the real situation.

2. Maximum Mn concentrations in Fe-C-Mn steels predicted by DICTRA are greater than those predicted by Howe's model from literature report. The reason probably is that DICTRA takes the cross-elemental effects into account leading to different partition coefficients and diffusion coefficients.
3. Maximum Mn concentrations predicted by DICTRA are higher than the experimental results. This may be because of the line-scan method which was used to characterise segregation in the steels, which can miss out the most segregated region on the cross-section and cause lower experimental results.
4. Compared with the analytical approaches (Scheil and Clyne-Kurz models), DICTRA can produce more precise predictions in terms of Mn segregation in continuously cast steels. Six elements in the steels can be modelled at the same time by DICTRA. The segregation results of the continuously cast microalloyed steels can be used to calculate the precipitate dissolution temperatures in solute-rich and solute-depleted regions respectively for subsequent rolling processing in continuous casting. Also DICTRA can be used to design new steels to decrease the segregation level for subsequent processing.

10.2 Suggestions for future work

It has been shown that the discrepancies between DICTRA predictions and experimental results were observed in slab 1 steel and the DS sample. The accuracy of diffusivity of alloying elements such as Mn, Si and Ni in δ-ferrite used in DICTRA and the effect of the dendrite arm coarsening process on the microsegregation may be the potential reasons to lead

to the discrepancies. The following procedures are suggested to be carried out to verify those reasons and further improve the present DICTRA model.

1. Steels with two different carbon contents (~0.4 wt % and 0.1 - 0.15 wt %) and higher alloying element contents (more than 1 wt %) can be prepared by ingot casting. The steel with lower carbon content will represent steel solidified as δ-ferrite until the solidification is complete, while the steel with higher carbon content should solidify through a peritectic reaction.
2. Each ingot steel can be cut into cylindrical shape samples for directional solidification trials. A range of withdrawal rates (10 - 1000 mm/hour) can be used to obtain different cooling rates (0.1 - 1 K/s) if the machine was running over night.
3. In order to investigate the formation of dendrite arm coarsening, the DS caster needs to be modified to allow the samples to be quenched from different temperatures through the solidification and homogenisation process from 1520 -1400 ℃
4. The microstructures of samples from different quenching temperatures and cooling rates can be analysed to obtain SDAS values. The relationship of SDAS, carbon content and cooling rate can be obtained to verify Equation 3-1. In addition, the cumulative profiles method using a more accurate elemental analysis method, e.g. wavelength-dispersive spectroscopy (WDS) can be adopted to characterise the microsegregation to decrease the uncertainty in the segregation profile.
5. The dendrite arm coarsening process can be identified by analysing the microstructures of samples quenched at different temperatures. The conditions (composition and cooling rate) at which the dendrite arm coarsening (ripening or coalescence) occurs can be summarised.
6. For the samples without coarsening process, the DICTRA model described in the present study can be applied to compare with the experimental results. The accuracy of diffusivity

of different elements (Mn, Si and Ni) in δ-ferrite and austenite phases can be investigated by analysing fitting feature of steels quenched at different temperature with and without peritectic reaction during solidification. If DICTRA predictions did not agree well with experimental results, the DIC_PARROT module in DICTRA can be used to assess experimental data and optimise calculations.

7. For the samples which exhibit dendrite arm coarsening, the effect on the microsegregation can be investigated by using line-scans or mapping. Multiple cells or a cell with changing size may be applied in the DICTRA model to take into account the coarsening process according to the coarsening mechanisms.

List of References

1. H.L. Andrade, M.G. Akben, J.J. Jonas, Effect of molybdenum, niobium, and vanadium on static recovery and recrystallization and on solute strengthening in microalloyed steels. Metallurgical Transactions A, 1983. **14**(10): p. 1967-1977.

2. C.L. Davis, M. Strangwood, Preliminary study of the inhomogeneous precipitate distributions in Nb-microalloyed plate steels. Journal of Materials Science, 2002. **37**(6): p. 1083-1090.

3. Z. Chen, M.H. Loretto, R.C. Cochrane, Nature of large precipitates in titanium-containing HSLA steels. Materials Science and Technology, 1987. **3**(10): p. 836-844.

4. D. Chakrabarti, C. Davis, M. Strangwood, Characterisation of bimodal grain structures in HSLA steels. Materials Characterization, 2007. **58**(5): p. 423-438.

5. D. Chakrabarti, C.L. Davis, M. Strangwood, The effect of precipitate distribution on high strength low alloy (HSLA) steel grain structures. Transactions of the Indian Institute of Metals, 2006. **59**(2): p. 205-213.

6. D. Chakrabarti, C. Davis, M. Strangwood, Development of bimodal grain structures in Nb-containing high-strength low-alloy steels during slab reheating. Metallurgical and Materials Transactions A-Physical Metallurgy and Materials Science, 2008. **39A**(8): p. 1963-1977.

7. D. Chakrabarti, C.L. Davis, M. Strangwood, Effect of deformation and Nb segregation on grain size bimodality in HSLA steel. Materials Science and Technology, 2009. **25**(8): p. 939-946.

8. S.J. Wu, C.L. Davis, Effect of duplex ferrite grain size distribution on local fracture stresses of Nb-microalloyed steels. Materials Science and Engineering A-Structural Materials Properties Microstructure and Processing, 2004. **387**: p. 456-460.

9. D. Mirkovic, R. Schmid-Fetzer, Directional solidification of Mg-Al alloys and microsegregation study of Mg alloys AZ31 and AM50: Part i. Methodology. Metallurgical and Materials Transactions A-Physical Metallurgy and Materials Science, 2009. **40A**(4): p. 958-973.

10. B.K. Dhindaw, T. Antonsson, J. Tinoco, H. Fredriksson, Characterization of the peritectic reaction in medium-alloy steel through microsegregation and heat-of-transformation studies. Metallurgical and Materials Transactions A-Physical Metallurgy and Materials Science, 2004. **35A**(9): p. 2869-2879.

11. P.L. Ferrandini, C.T. Rios, A.T. Dutra, M.A. Jaime, P.R. Mei, R. Caram, Solute segregation and microstructure of directionally solidified austenitic stainless steel. Materials Science and Engineering A-Structural Materials Properties Microstructure and Processing, 2006. **435**: p. 139-144.

12. N. Chakraborti, R. Kumar, D. Jain, A study of the continuous casting mold using a pareto-converging genetic algorithm. Applied Mathematical Modelling, 2001. **25**(4): p. 287-297.

13. Y.A. Meng, B.G. Thomas, Modeling transient slag-layer phenomena in the shell/mold gap in continuous casting of steel. Metallurgical and Materials Transactions B-Process Metallurgy and Materials Processing Science, 2003. **34**(5): p. 707-725.

14. J. Sengupta, B.G. Thomas, M.A. Wells, The use of water cooling during the continuous casting of steel and aluminum alloys. Metallurgical and Materials Transactions A-Physical Metallurgy and Materials Science, 2005. **36A**(1): p. 187-204.

15. H.M. Wang, G.R. Li, Y.C. Lei, Y.T. Zhao, Q.X. Dai, J.J. Wang, Mathematical heat transfer model research for the improvement of continuous casting slab temperature. ISIJ International, 2005. **45**(9): p. 1291-1296.

16. S. Luo, M.Y. Zhu, S. Louhenkilpi, Numerical simulation of solidification structure of high carbon steel in continuous casting using cellular automaton method. ISIJ International, 2012. **52**(5): p. 823-830.

17. M.J. Peet, H.S. Hasan, H.K.D.H. Bhadeshia, Prediction of thermal conductivity of steel. International Journal of Heat and Mass Transfer, 2011. **54**(11-12): p. 2602-2608.

18. Overall heat transfer coefficients for some common fluids and heat exchanger surfaces. [The Engineering ToolBox]; Available from: http://www.engineeringtoolbox.com/overall-heat-transfer-coefficients-d_284.html.

19. Emissivity coefficients of some common materials. [The Engineering ToolBox]; Available from: http://www.engineeringtoolbox.com/emissivity-coefficients-d_447.html.

20. M.C. Flemings, Solidification processing Mcgraw-Hill College New York, 1974.

21. R.E. Reed-Hill, Physical metallurgy principles, Van Nostrand, 1973.

22. G. Krauss, Solidification, segregation, and banding in carbon and alloy steels. Metallurgical and Materials Transactions B, 2003. **34**(6): p. 781-792.

23. S.K. Choudhary, S. Ganguly, Morphology and segregation in continuously cast high carbon steel billets. ISIJ International, 2007. **47**(12): p. 1759-1766.

24. M.J. Long, L.F. Zhang, F. Lu, A simple model to calculate dendrite growth rate during steel continuous casting process. ISIJ International, 2010. **50**(12): p. 1792-1796.

25. W. Kurz, About initial solidification in continuous casting of steel. Metallurgia Italiana, 2008(7-8): p. 56-64.

26. M. Imagumbai, T. Takeda, Influence of calcium-treatment on sulfide-inclusions and oxide-inclusions in continuous-cast slab of clean steel - dendrite structure and inclusions. ISIJ International, 1994. **34**(7): p. 574-583.

27. Y.L. Lu, M.Q. Li, Y. Niu, X.C. Li, Microstructure and element distribution during partial remelting of an Al-4Cu-Mg alloy. Journal of Materials Engineering and Performance, 2008. **17**(1): p. 25-29.

28. A. Mortensen, On the influence of coarsening on microsegregation. Metallurgical Transactions A-Physical Metallurgy and Materials Science, 1989. **20**(2): p. 247-253.

29. T. Kraft, Y.A. Chang, Discussion of "effect of dendrite arm coarsening on microsegregation". Metallurgical and Materials Transactions A-Physical Metallurgy and Materials Science, 1998. **29**(9): p. 2447-2449.

30. M.C. Flemings, Coarsening in solidification processing. Materials Transactions, 2005. **46**(5): p. 895-900.

31. H.W. Kerr, J. Cisse, G.F. Bolling, Equilibrium and nonequilibrium peritectic transformations. Acta Metallurgica, 1974. **22**(6): p. 677-686.

32. K. Matsuura, Y. Itoh, T. Narita, A solid-liquid diffusion couple study of a peritectic reaction in iron carbon system. ISIJ International, 1993. **33**(5): p. 583-587.

33. M. Ohno, K. Matsuura, Diffusion-controlled peritectic reaction process in carbon steel analyzed by quantitative phase-field simulation. Acta Materialia, 2010. **58**(18): p. 6134-6141.

34. H. Fredriksson, T. Nylen, Mechanism of peritectic reactions and transformations. Metal Science, 1982. **16**(6): p. 283-294.

35. J. Singh, G.R. Purdy, G.C. Weatherly, Microstructural and microchemical aspects of the solid-state decomposition of delta-ferrite in austenitic stainless-steels. Metallurgical Transactions a-Physical Metallurgy and Materials Science, 1985. **16**(8): p. 1363-1369.

36. T. Takahashi, K. Ohsasa, J. Tanaka, Peritectic reaction and delta-gamma transformation mechanism in carbon-steels. Tetsu to Hagane-Journal of the Iron and Steel Institute of Japan, 1987. **73**(1): p. 99-106.

37. D. Phelan, M. Reid, R. Dippenaar, Kinetics of the peritectic reaction in an Fe-C alloy. Materials Science and Engineering A-Structural Materials Properties Microstructure and Processing, 2008. **477**(1-2): p. 226-232.

38. H. Shibata, Y. Arai, M. Suzuki, T. Emi, Kinetics of peritectic reaction and transformation in Fe-C alloys. Metallurgical and Materials Transactions B-Process Metallurgy and Materials Processing Science, 2000. **31**(5): p. 981-991.

39. T. Emi, H. Fredriksson, High-speed continuous casting of peritectic carbon steels. Materials Science and Engineering A-Structural Materials Properties Microstructure and Processing, 2005. **413**: p. 2-9.

40. H. Fredriksson, J. Stjerndahl, Solidification of iron-base alloys. Metal Science, 1982. **16**(12): p. 575-585.

41. H. Fredriksson, The mechanism of the peritectic reaction in iron-base alloys. Metal Science, 1976. **10**(3): p. 77-86.

42. A. Kagawa, T. Okamoto, Influence of alloying elements on temperature and composition for peritectic reaction in plain carbon-steels. Materials Science and Technology, 1986. **2**(10): p. 997-1008.

43. Phase transformations in steels, in: E. Pereloma, D.V. Edmonds (Eds.) Phase transformations in steels, Woodhead Publishing, 2012, pp. i-iii.

44. G.E. Totten, M.A.H. Howes, Steel heat treatment handbook, Taylor & Francis, 1997.

45. Y. Du, J.C. Schuster, Z.K. Liu, R.X. Hu, P. Nash, W.H. Sun, W.W. Zhang, J. Wang, L.J. Zhang, C.Y. Tang, Z.J. Zhu, S.H. Liu, Y.F. Ouyang, W.Q. Zhang, N. Krendelsberger, A thermodynamic

description of the Al-Fe-Si system over the whole composition and temperature ranges via a hybrid approach of CALPHAD and key experiments. Intermetallics, 2008. **16**(4): p. 554-570.

46. V.T. Witusiewicz, A.A. Bondar, U. Hecht, S. Rex, T.Y. Velikanova, The Al-B-Nb-Ti system iii. Thermodynamic re-evaluation of the constituent binary system Al-Ti. Journal of Alloys and Compounds, 2008. **465**(1-2): p. 64-77.

47. A. Jacot, M. Rappaz, A pseudo-front tracking technique for the modelling of solidification microstructures in multi-component alloys. Acta Materialia, 2002. **50**(8): p. 1909-1926.

48. S. Malinov, W. Sha, Software products for modelling and simulation in materials science. Computational Materials Science, 2003. **28**(2): p. 179-198.

49. F. Takahashi, Y. Momoi, K. Kajikawa, H. Yamada, Effect of microsegregation on porosity formation in high Cr steel under pressurized atmosphere. Tetsu to Hagane-Journal of the Iron and Steel Institute of Japan, 2010. **96**(3): p. 107-116.

50. M. Wu, J. Li, A. Ludwig, A. Kharicha, Modeling diffusion-governed solidification of ternary alloys - part 1: Coupling solidification kinetics with thermodynamics. Computational Materials Science, 2013. **79**: p. 830-840.

51. T. Matsumiya, H. Kajioka, S. Mizoguchi, Y. Ueshima, H. Esaka, Mathematical-analysis of segregations in continuously-cast slabs. Transactions of the Iron and Steel Institute of Japan, 1984. **24**(11): p. 873-882.

52. G. Straffelini, L. Lutterotti, M. Tonolli, M. Lestani, Modeling solidification microstructures of steel round billets obtained by continuous casting. ISIJ International, 2011. **51**(9): p. 1448-1453.

53. R. Trivedi, W. Kurz, Dendritic growth. International Materials Reviews, 1994. **39**(2): p. 49-74.

54. Y.M. Won, B.G. Thomas, Simple model of microsegregation during solidification of steels. Metallurgical and Materials Transactions A-Physical Metallurgy and Materials Science, 2001. **32**(7): p. 1755-1767.

55. A. Turkeli, Microsegregation in manganese steels. University of Sheffield, 1989.

56. J. Lacaze, P. Benigni, A. Howe, Some issues concerning experiments and models for alloy microsegregation. Advanced Engineering Materials, 2003. **5**(1-2): p. 37-46.

57. F.Y. Xie, X.Y. Yan, L. Ding, F. Zhang, S.G. Chen, M.G. Chu, Y.A. Chang, A study of microstructure and micro segregation of aluminum 7050 alloy. Materials Science and Engineering A-Structural Materials Properties Microstructure and Processing, 2003. **355**(1-2): p. 144-153.

58. X. Yan, S. Chen, F. Xie, Y.A. Chang, Computational and experimental investigation of micro segregation in an Al-rich Al-Cu-Mg-Si quaternary alloy. Acta Materialia, 2002. **50**(9): p. 2199-2207.

59. P.K. Sung, D.R. Poirier, Liquid-solid partition ratios in nickel-base alloys. Metallurgical and Materials Transactions A-Physical Metallurgy and Materials Science, 1999. **30**(8): p. 2173-2181.

60. M.N. Gungor, A statistically significant experimental-technique for investigating microsegregation in cast alloys. Metallurgical Transactions A-Physical Metallurgy and Materials Science, 1989. **20**(11): p. 2529-2533.

61. W.H. Yang, W. Chen, K.M. Chang, S. Mannan, J. DeBarbadillo, Monte Carlo sampling for microsegregation measurements in cast structures. Metallurgical and Materials Transactions A-Physical Metallurgy and Materials Science, 2000. **31**(10): p. 2569-2574.

62. M.C. Flemings, D.R. Poirier, R.V. Barone, H.D. Brody, Microsegregation in iron-base alloys. Journal of the Iron and Steel Institute, 1970. **208**: p. 371-&.

63. F.Y. Xie, T. Kraft, Y. Zuo, C.H. Moon, Y.A. Chang, Microstructure and microsegregation in Al-rich Al-Cu-Mg alloys. Acta Materialia, 1999. **47**(2): p. 489-500.

64. S. Tin, T.M. Pollock, Phase instabilities and carbon additions in single-crystal nickel-base superalloys. Materials Science and Engineering A-Structural Materials Properties Microstructure and Processing, 2003. **348**(1-2): p. 111-121.

65. G.E. Fuchs, Solution heat treatment response of a third generation single crystal Ni-base superalloy. Materials Science and Engineering A-Structural Materials Properties Microstructure and Processing, 2001. **300**(1-2): p. 52-60.

66. M. Ganesan, D. Dye, P.D. Lee, A technique for characterizing microsegregation in multicomponent alloys and its application to single-crystal superalloy castings. Metallurgical and Materials Transactions A-Physical Metallurgy and Materials Science, 2005. **36A**(8): p. 2191-2204.

67. M. Charpentier, D. Daloz, A. Hazotte, E. Gautier, G. Lesoult, M. Grange, Study of microstructure and solute partitioning in a cast Ti-48Al-2Cr-2Nb alloy by quenching during directional solidification technique. Metallurgical and Materials Transactions A-Physical Metallurgy and Materials Science, 2003. **34A**(10): p. 2139-2148.

68. M.S.A. Karunaratne, D.C. Cox, P. Carter, R.C. Reed, Modelling of the microsegregation in CMSX-4 superalloy and its homogenisation during heat treatment, Minerals, Metals & Materials Soc, Warrendale, 2000.

69. M. Ganesan, L. Thuinet, D. Dye, P.D. Lee, Quantification of microsegregation in cast Al-Si-Cu alloys. Metallurgical and Materials Transactions B-Process Metallurgy and Materials Processing Science, 2007. **38**(4): p. 557-566.

70. M.C. Flemings, Our understanding of macrosegregation: Past and present. ISIJ International, 2000. **40**(9): p. 833-841.

71. G. Lesoult, Macro segregation in steel strands and ingots: Characterisation, formation and consequences. Materials Science and Engineering A-Structural Materials Properties Microstructure and Processing, 2005. **413**: p. 19-29.

72. Y. Nakai, H. Kurahashi, T. Emi, O. Haida, Development of steels resistant to hydrogen induced cracking in wet hydrogen sulfide environment Transactions of the Iron and Steel Institute of Japan, 1979. **19**(7): p. 401-410.

73. A. Ghosh, Segregation in cast products. Sadhana-Academy Proceedings in Engineering Sciences, 2001. **26**: p. 5-24.

74. J.J. Moore, Review of axial segregation in continuous cast steel. Continuous casting, Iron and Steel Society, 1984. **3**: p. 11-20.

75. R.A. Hardin, K. Liu, A. Kapoor, C. Beckermann, A transient simulation and dynamic spray cooling control model for continuous steel casting. Metallurgical and Materials Transactions B-Process Metallurgy and Materials Processing Science, 2003. **34**(3): p. 297-306.

76. K. Miyazawa, K. Schwerdtfeger, Macrosegregation in continuously cast steel slabs - preliminary theoretical investigation on the effect of steady-state bulging. Archiv Fur Das Eisenhuttenwesen, 1981. **52**(11): p. 415-422.

77. J.H. Lee, H.C. Kim, C.Y. Jo, S.K. Kim, J.H. Shin, S. Liu, R. Trivedi, Microstructure evolution in directionally solidified Fe-18Cr stainless steels. Materials Science and Engineering A-Structural Materials Properties Microstructure and Processing, 2005. **413**: p. 306-311.

78. P.N. Quested, M. McLean, Solidification morphologies in directionally solidified superalloys. Materials Science and Engineering, 1984. **65**(1): p. 171-180.

79. D.A. Porter, K.E. Easterling, Phase transformations in metals and alloys, third edition (revised reprint), Taylor & Francis, 1992.

80. J.A. Sarreal, G.J. Abbaschian, The effect of solidification rate on microsegregation. Metallurgical Transactions A-Physical Metallurgy and Materials Science, 1986. **17**(11): p. 2063-2073.

81. Y. Du, Y.A. Chang, S.H. Liu, B.Y. Huang, F.Y. Xie, Y. Yang, S.L. Chen, Thermodynamic description of the Al-Fe-Mg-Mn-Si system and investigation of microstructure and microsegregation during directional solidification of an Al-Fe-Mg-Mn-Si alloy. Zeitschrift Fur Metallkunde, 2005. **96**(12): p. 1351-1362.

82. H.D. Brody, M.C. Flemings, Solute redistribution in dendritic solidification. Transactions of the Metallurgical Society of Aime, 1966. **236**(5): p. 615-&.

83. I. Ohnaka, Mathematical analysis of solute redistribution during solidification with diffusion in the solid phase. Transactions of the Iron and Steel Institute of Japan, 1986. **26**(12): p. 1045-1051.

84. J. Billingham, J.V. Sharp, J. Spurrier, P.J. Kilgallon, Review of the performance of high strength steels used offshore. 2003.

85. Y.M. Won, K.H. Kim, T.J. Yeo, K.H. Oh, Effect of cooling rate on ZST, LIT and ZDT of carbon steels near melting point. ISIJ International, 1998. **38**(10): p. 1093-1099.

86. S.K. Choudhary, Thermodynamic evaluation of inclusion formation during cooling and solidification of low carbon Si-Mn killed steel. Materials and Manufacturing Processes, 2012. **27**(9): p. 925-929.

87. S.K. Choudhary, A. Ghosh, Mathematical model for prediction of composition of inclusions formed during solidification of liquid steel. ISIJ International, 2009. **49**(12): p. 1819-1827.

88. M. Ode, J.S. Lee, S.G. Kim, W.T. Kim, T. Suzuki, Phase-field model for solidification of ternary alloys. ISIJ International, 2000. **40**(9): p. 870-876.

89. T. Koseki, T. Matsumiya, W. Yamada, T. Ogawa, Numerical modeling of solidification and subsequent transformation of Fe-Cr-Ni alloys. Metallurgical and Materials Transactions A-Physical Metallurgy and Materials Science, 1994. **25**(6): p. 1309-1321.

90. W. Khalifa, F.H. Samuel, J.E. Gruzleski, Iron intermetallic phases in the al corner of the Al-Si-Fe system. Metallurgical and Materials Transactions A-Physical Metallurgy and Materials Science, 2003. **34A**(3): p. 807-825.

91. B. Sundman, B. Jansson, J.O. Andersson, The Thermo-Calc databank system. CALPHAD-Computer Coupling of Phase Diagrams and Thermochemistry, 1985. **9**(2): p. 153-190.

92. B. Jansson, B. Jonsson, B. Sundman, J. Agren, The Thermo Calc project. Thermochimica Acta, 1993. **214**(1): p. 93-96.

93. J. Agren, Calculation of phase diagrams: CALPHAD. Current Opinion in Solid State & Materials Science, 1996. **1**(3): p. 355-360.

94. P. Shi, B. Sundman Thermo-Calc software user's guide. 2008.

95. A.F. Guillermet, Critical-evaluation of the thermodynamic properties of cobalt. International Journal of Thermophysics, 1987. **8**(4): p. 481-510.

96. B. Jonsson, J. Agren, Thermodynamic assessment of Sb-Sn system. Materials Science and Technology, 1986. **2**(9): p. 913-916.

97. T. Yamashita, K. Okuda, T. Obara, Application of Thermo-Calc to the developments of high-performance steels. Journal of Phase Equilibria, 1999. **20**(3): p. 231-237.

98. J.C. Hu, H.M. Song, Y. Ming, L.Z. Jiang, Thermo-Calc calculation and experimental study of microstructure of SUS 410s and SUS 430 ferrite stainless steels at high temperature. Journal of Iron and Steel Research International, 2007. **14**: p. 183-188.

99. S.H. Atapek, E. Erisir, S. Gumus, Modeling and thermal analysis of solidification in a low alloy steel. Journal of Thermal Analysis and Calorimetry, 2013. **114**(1): p. 179-183.

100. A. Karma, W.J. Rappel, Quantitative phase-field modeling of dendritic growth in two and three dimensions. Physical Review E, 1998. **57**(4): p. 4323-4349.

101. R. Kobayashi, Modeling and numerical simulations of dendritic crystal-growth. Physica D, 1993. **63**(3-4): p. 410-423.

102. A.A. Wheeler, W.J. Boettinger, G.B. McFadden, Phase-field model for isothermal phase-transitions in binary-alloys. Physical Review A, 1992. **45**(10): p. 7424-7439.

103. S.G. Kim, W.T. Kim, T. Suzuki, Phase-field model for binary alloys. Physical Review E, 1999. **60**(6): p. 7186-7197.

104. I. Steinbach, F. Pezzolla, B. Nestler, M. Seesselberg, R. Prieler, G.J. Schmitz, J.L.L. Rezende, A phase field concept for multiphase systems. Physica D, 1996. **94**(3): p. 135-147.

105. J. Tiaden, B. Nestler, H.J. Diepers, I. Steinbach, The multiphase-field model with an integrated concept for modelling solute diffusion. Physica D, 1998. **115**(1-2): p. 73-86.

106. B. Bottger, M. Apel, B. Santillana, D.G. Eskin, Phase-field modelling of microstructure formation during the solidification of continuously cast low carbon and HSLA steels. Mcwasp Xiii: International Conference on Modeling of Casting, Welding and Advanced Solidification Processes, 2012. **33**: p. 8.

107. A.F. Ferreira, L.D. Ferreira, Microsegregation in Fe-C-P ternary alloys using a phase-field model. Journal of the Brazilian Society of Mechanical Sciences and Engineering, 2009. **31**(3): p. 173-180.

108. Y. Ueshima, N. Komatsu, S. Mizoguchi, H. Kajioka, Effects of alloying elements on interdendritic microsegregation of carbon-steel. Tetsu to Hagane-Journal of the Iron and Steel Institute of Japan, 1987. **73**(11): p. 1551-1558.

109. Y. Ueshima, S. Mizoguchi, T. Matsumiya, H. Kajioka, Analysis of solute distribution in dendrites of carbon-steel with delta-gamma-transformation during solidification. Metallurgical Transactions B-Process Metallurgy, 1986. **17**(4): p. 845-859.

110. J. CRANK, Two methods for the numerical solution of moving-boundary problems in diffusion and heat flow. The Quarterly Journal of Mechanics and Applied Mathematics, 1957. **10**(2): p. 220-231.

111. A.A. Howe, D.H. Kirkwood, Computer prediction of microsegregation in peritectic alloy systems. Materials Science and Technology, 2000. **16**(9): p. 961-967.

112. J.O. Andersson, J. Agren, Models for numerical treatment of multicomponent diffusion in simple phases. Journal of Applied Physics, 1992. **72**(4): p. 1350-1355.

113. S. Griesser, M. Reid, R. Pierer, C. Bernhard, R. Dippenaar, In situ quantification of micro-segregation that occurs during the solidification of steel. Steel Research International, 2014. **85**(8): p. 1257-1265.

114. S. Yoshida, K. Ushioda, J. Agren, Kinetic model of the gamma to alpha phase transformation at grain boundaries in boron-bearing low-alloy steel. ISIJ International, 2014. **54**(3): p. 685-692.

115. S. Aminorroaya, M. Reid, R. Dippenaar, Simulation of microsegregation and the solid/liquid interface progression in the concentric solidification technique. Modelling and Simulation in Materials Science and Engineering, 2011. **19**(2): p. 16.

116. H.E. Lippard, C.E. Campbell, T. Bjorklind, U. Borggren, P. Kellgren, V.P. Dravid, G.B. Olson, Microsegregation behavior during solidification and homogenization of Aermet100 steel. Metallurgical and Materials Transactions B-Process Metallurgy and Materials Processing Science, 1998. **29**(1): p. 205-210.

117. H.S. Kim, Y. Kobayashi, K. Nagai, Prediction of prior austenite grain size of high-phosphorous steels through phase transformation simulation. ISIJ International, 2006. **46**(6): p. 854-858.

118. J. Lis, A. Lis, C. Kolan, Investigation of boron segregation in low carbon steel. Metalurgija, 2011. **50**(2): p. 123-126.

119. T. Yamamoto, T. Takashima, K. Nishida, Inter-diffusion in the zeta-solid solution of a Ni-Al system. Transactions of the Japan Institute of Metals, 1980. **21**(9): p. 601-608.

120. L.S. Darken, Diffusion of carbon in austenite with a discontinuity in composition. Transactions of the American Institute of Mining and Metallurgical Engineers, 1949. **180**: p. 430-438.

121. L. Onsager, Reciprocal relations in irreversible processes. I. Physical Review, 1931. **37**(4): p. 405-426.

122. Thermo-Calc console mode user guide version 4.1. 2014.

123. C.L. Davis, M. Strangwood, Segregation behaviour in Nb microalloyed steels. Materials Science and Technology, 2009. **25**(9): p. 1126-1133.

124. T.W. Clyne, W. Kurz, Solute redistribution during solidification with rapid solid-state diffusion. Metallurgical Transactions A-Physical Metallurgy and Materials Science, 1981. **12**(6): p. 965-971.

125. A.S.f.M.M.H. Committee, Metals handbook. - vol. 8: Metallography, structures and phase diagrams, ASM International, 1973.

126. R. Willms, High strength steel for steel constructions. 2009: p. 597-604.

127. F.B. Pickering, Physical metallurgy and the design of steels, Applied Science Publishers, 1978.

128. H. Mehrer, Diffusion in solids: Fundamentals, methods, materials, diffusion-controlled processes, Springer, 2007.

129. J. Reiter, C. Bernhard, H. Presslinger, Austenite grain size in the continuous casting process: Metallographic methods and evaluation. Materials Characterization, 2008. **59**(6): p. 737-746.